Simulation of shock-induced bubble collapse with application to vascular injury in shockwave lithotripsy

Thesis by

Vedran Coralic

In Partial Fulfillment of the Requirements

for the Degree of

Doctor of Philosophy

California Institute of Technology

Pasadena, California

2015

(Defended September 18, 2014)

In loving memory of my grandparents, Fadila Coralic (1925–2007) and Alija Coralic (1924–2014).

Acknowledgments

The present thesis constitutes the culmination of nearly seven years of research during which numerous mentors, coworkers, family and friends have left their mark. And while I am the sole author of this work, there is not a doubt in my mind that it would not exist without their contributions, whether they had come through scientific discussion or emotional support. Of course, out of everyone, I would most like to acknowledge the helping hand of my thesis advisor, Tim Colonius, whose seemingly boundless knowledge of computational fluid dynamics, insight into flow physics, and patience have helped me both bring my research to fruition, as well as grow personally and professionally. Tim's unwavering support and strong belief in my ability to succeed were key factors in the completion of my doctorate and I thank him for both the role he has played, and will play, in my present and future accomplishments.

Naturally, I would also like to thank my committee members: Guillaume Blanquart, John Brady and Joseph Shepherd, as well as past and present members of the Computational Flow Physics Group, especially Keita Ando, Daniel Appelö, Andres Goza, Kristján Guðmundsson, Matthew Inkman, Eric Johnsen, Jeff Krimmel, Sebastian Liska, Jomela Meng and Sam Taira. My committee was invaluable in helping me develop new and original ways to achieve my research goals, while my fellow lab mates, in addition to frequently partaking in insightful scientific discussions, were highly supportive during difficult times in both matters of life and work. A great debt of gratitude is also owed to the members of the Program Project Grant Group, notably Michael Bailey, Jonathan Freund, Wayne Kreider, Thomas Matula, Jim McAteer and Oleg Sapozhnikov, whose theoretical and practical understanding of bubble dynamics in tissue helped me form the basis of some of the ideas explored in the present work.

Last but not least, I would like thank my mother, Mira Damjanovic, my father, Jasmin Coralic, and my girlfriend, Stanislava Petkova, who were always incredibly supportive despite being oversees and thousands of miles away. It is with certainty that I know that without their love, support and sacrifices, I would not be where I am today.

This work was supported by NIH Grant PO1-DK043881, NSF Grant OCI-1053575 and the NSF Graduate Research Fellowship Program.

Abstract

Shockwave lithotripsy is a noninvasive medical procedure wherein shockwaves are repeatedly focused at the location of kidney stones in order to pulverize them. Stone comminution is thought to be the product of two mechanisms: the propagation of stress waves within the stone and cavitation erosion. However, the latter mechanism has also been implicated in vascular injury. In the present work, shock-induced bubble collapse is studied in order to understand the role that it might play in inducing vascular injury. A high-order accurate, shock- and interface-capturing numerical scheme is developed to simulate the three-dimensional collapse of the bubble in both the free-field and inside a vessel phantom. The primary contributions of the numerical study are the characterization of the shock-bubble and shock-bubble-vessel interactions across a large parameter space that includes clinical shockwave lithotripsy pressure amplitudes, problem geometry and tissue viscoelasticity, and the subsequent correlation of these interactions to vascular injury. Specifically, measurements of the vessel wall pressures and displacements, as well as the finite strains in the fluid surrounding the bubble, are utilized with available experiments in tissue to evaluate damage potential. Estimates are made of the smallest injurious bubbles in the microvasculature during both the collapse and jetting phases of the bubble's life cycle. The present results suggest that bubbles larger than 1 μm in diameter could rupture blood vessels under clinical SWL conditions.

Contents

List of Figures

List of Tables

Nomenclature

Greek letters

α	Rescaled WENO ideal weight, volume fraction or vortex decay rate
β	WENO smoothness indicator
Γ	Stiffened gas EOS fitting parameter function
γ	Small deviatoric strain, specific heat ratio or stiffened gas EOS fitting parameter
δ_{ij}	Kronecker delta tensor
Δt	Time-step size
Δx	Cell width in x-direction
Δy	Cell width in y-direction
Δz	Cell width in z-direction
ϵ	Kinetic energy dissipation rate, machine epsilon or vortex strength
ε	Specific internal energy
θ	Polar coordinate/direction or shockwave angle
$\boldsymbol{\Lambda}$	Eigenvalue matrix
λ	Principal stretch
μ	Shear viscosity
ν	Kinematic viscosity
$\boldsymbol{\xi}$	Natural or virtual position vector
ξ	Natural or virtual coordinate/direction
Π_∞	Stiffened gas EOS fitting parameter function

π_∞	Stiffened gas EOS fitting parameter
ρ	Density
σ	Surface tension coefficient
τ	Deviatoric or viscous stress
ϕ	Azimuthal coordinate/direction or velocity potential
$\boldsymbol{\omega}$	Vorticity vector
ω	Vorticity component

Roman letters

$\mathbf{A}$	Jacobian of $\mathbf{f}$
A	Area or sink flow fitting parameter
$\mathbf{B}$	Jacobian of $\mathbf{g}$
$\mathcal{B}$	Body configuration
B	Sink flow fitting parameter
$\mathbf{C}$	Jacobian of $\mathbf{h}$
C	CFL number or sink flow fitting parameter
c	Sound speed
Ca	Cauchy number
$\mathbf{D}$	Deformation rate tensor
D	Diameter or diffusion number
$\mathbf{d}$	Displacement vector
d	Displacement or WENO ideal weight
$\mathbf{E}$	Green-Lagrange strain tensor
E	Green-Lagrange strain or total energy
$\mathbf{F}$	Deformation gradient tensor
$\mathbf{f}$	Flux vector in x-direction
G	Shear modulus
$\mathbf{g}$	Flux vector in y-direction

H	Bubble distance from vessel center or Heaviside function
$\mathbf{h}$	Flux vector in z-direction
h	Vascular injury layer thickness
$\mathbf{I}$	Identity matrix
I	Control volume interval
$\mathbf{L}$	RHS operator
L	Norm or characteristic length
M	Mach number
m	Sink flow strength
N	Number of dimensions/cells/particles or shape function
$\mathbf{n}$	Unit normal vector
P	Pressure
p	Pressure
$\mathbf{Q}$	Right eigenvector matrix
$\mathbf{q}$	Conservative variables vector
R	Radius
r	Radial coordinate/direction
Re	Reynolds number
S	WENO stencil
$\mathbf{s}$	Source term vector
s	HLLC wave speed
$\mathbf{T}$	Viscous stress tensor
T	Temperature
t	Time
U	Characteristic velocity or velocity in x-direction
$\mathbf{u}$	Velocity vector
u	Characteristic velocity or velocity in x-direction

V	Volume
$\mathbf{v}$	Primitive variables vector
v	Velocity in y-direction
$\mathbf{w}$	Characteristic variables vector
w	Velocity in z-direction
We	Weber number
$\mathbf{x}$	Position vector
x	x-coordinate/direction
Y	Young's modulus
y	y-coordinate/direction
z	z-coordinate/direction

Subscripts

Q_*	HLLC star region value
Q_∞	Far-field property
Q_0	Value at ambient conditions or initial value
Q_b	Bubble property
Q_c	Value at bubble collapse
Q_d	Deviatoric component of strain or value at distal bubble/vessel wall interface
Q_di	Value at downstream bubble interface
Q_f	Final value
Q_g	Gas property
Q_j	Jet property
Q_L	Value at left of cell boundary
Q_l	Liquid property
Q_max	Maximum value
Q_min	Minimum value
Q_o	Value at ambient conditions or initial value

Q_p	Value at proximal bubble/vessel wall interface
Q_R	Value at right of cell boundary
Q_r	Refracted shockwave property
Q_s	Incident shockwave property
Q_t	Tissue or transmitted shockwave property
Q_u	Ultimate material property
Q_ui	Value at upstream bubble interface
Q_v	Vessel property or volumetric component of strain
Q_vm	von Mises invariant of strain

Superscripts

$\bar{Q}$	Arithmetic/Roe average value or property at bubble centroid
$\dot{Q}$	Temporal derivative of variable
$\hat{Q}$	Monotone function approximation
Q'	Ambient/initial value perturbation or deformed body configuration property
Q^*	Dimensionless variable
Q^a	Advective flux
Q^d	Diffusive flux
Q^L	Value at left of cell boundary
Q^R	Value at right of cell boundary

Abbreviations and acronyms

1D	One-dimensional
2D	Two-dimensional
3D	Three-dimensional
CFL	Courant-Friedrichs-Lewy
EOS	Equation of state
HLLC	Harten-Lax-van Leer-contact

NRBC	Non-reflective boundary condition
RBC	Reflective boundary condition
RHS	Right-hand side
RK	Runge-Kutta
SWL	Shockwave lithotripsy
TVD	Total variation diminishing
WENO	Weighted essentially non-oscillatory

Chapter 1

Introduction

1.1 Motivation

Shockwave lithotripsy (SWL) is a medical procedure utilized to noninvasively treat kidney stones. In typical clinical applications, approximately 2000 pressure pulses, with peak positive pressures between 30 and 110 MPa and peak negative pressures between -5 and -15 MPa, are generated by the lithotripter [26]. These pulses, or shockwaves, are delivered at a rate between 0.5 and 3 Hz and focused at the location of the stones in order to pulverize them and enable their expulsion through the urinary tract. Both the effectiveness and safety of the treatment strongly depends on the bubble dynamics excited by the passage of the shockwaves. Cavitating bubbles are documented to occur during treatment in both urine and surrounding tissue [6]. In the vicinity of kidney stones, cavitation erosion is thought to be an important mechanism of stone comminution [31, 34] and is characterized by the formation of liquid jets and the emission of shockwaves, both with the potential to inflict significant damage to nearby stones [65, 66, 91]. Unfortunately, cavitation in SWL is also implicated in the onset of renal trauma [5, 6], specifically hemorrhage, which is instigated by the rupture of small blood vessels, such as capillaries, arterioles and venules [114, 118], which have an average lumen diameter of only about 8 to 30 μm [26]. Recent experiments in the vasculature of *ex vivo* rat mesentery suggest that the growth and collapse of bubbles, along with liquid jet impact, may deform small blood vessels sufficiently as to cause them to rupture [19–21]. In order to improve the effectiveness and safety of SWL, it is therefore imperative to fully understand the mechanisms through which cavitation may contribute to both stone removal and vascular injury.

The relationship between cavitation and bioeffects, however, remains poorly understood in comparison to that between cavitation and stone comminution. Indeed, even fundamental inquiries regarding vascular rupture, such as how it is initiated and what the size of injurious bubbles are, remain to be clarified. In attempt to do so, the present study considers the numerical simulation of the shock-induced bubble collapse in the free-field and a vessel phantom. The overarching objective is to quantify and compare the resulting pressure fields, strain fields and vessel wall displacements with available experimental data in order to characterize the potential for vascular rupture and its underlying mechanisms under a variety of physiological and clinical SWL conditions.

1.2 Historical perspective

Hemorrhage is a nearly inevitable side effect of SWL [26] and understanding the interaction between cavitation bubbles and surrounding tissue is paramount to reducing it. In both experiments and simulations, however, characterization of the bubble-vessel dynamics has been difficult. Experimentally, the challenges of performing measurements and observations in tissue and blood vessels are exacerbated by small spatial and fast temporal scales. As a result, experimental work has primarily been carried out *in vitro*, typically utilizing gels and vessel phantoms to simulate tissue and blood vessels, respectively [13, 14, 73, 118]. The first observations of *ex vivo* bubble dynamics in blood vessels and under clinical conditions were reported by Caskey *et al.* [17], in the case of ultrasonic cavitation of microbubbles in rat cecum. Their results were cast in the context of gene therapy and localized drug delivery and did not specifically address the potential mechanisms of vascular injury. These mechanisms were the focus of subsequent work by Chen *et al.* [19–22], who performed analogous experiments in *ex vivo* rat mesentery. Utilizing high-speed microphotography, they measured the transient bubble-vessel interactions and correlated observable injuries with the magnitude of the vessel deformations. They concluded that in the context of SWL, three mechanisms can potentially result in the mechanical failure of blood vessels due to cavitation. These include vessel distention due to bubble growth, vessel invagination due to bubble collapse, and finally, puncturing of the vessel wall due to bubble jetting.

Identifying these same mechanisms in numerical simulations has its own set of challenges. In particular, the understanding of the rheology of tissue is incomplete. Recent efforts to study vessel rupture mechanisms due to cavitating bubbles have circumvented this issue, modeling the wall of the blood vessel in great detail and omitting the tissue in which it is embedded. These simulations, performed by Ye and Bull [117] and Miao *et al.* [84], were carried out in an axisymmetric geometry, with both the bubble and vessel wall immersed in an incompressible fluid. Their efforts were successful in demonstrating that ultrasonically excited microbubbles could generate sufficiently high vessel wall stresses during distention as to induce rupture. Unfortunately, due to the axisymmetry and incompressibility assumptions, the wall stresses that would arise from bubble collapse and liquid jet impact could not be addressed.

The damage potential of bubble jetting was considered in the axisymmetric compressible flow simulations of Freund *et al.* [43] and Kobayashi *et al.* [72], but in the context of the shock-induced collapse of a bubble near a planar tissue simulant. Freund *et al.* set the properties of the simulant to those of water but varied its shear viscosity in order to study how effectively various experimental measurements in tissue could suppress the penetration of the liquid jet. Values between 0.01 and 10 Pa·s were considered. The results of the study showed that the penetration depth of the jet into the boundary could greatly be suppressed by the larger viscosity measurements. The resulting viscous shear stresses, however, were estimated to be sufficiently large on the surface of the tissue as to potentially damage cells. Freund *et al.* postulated that this mechanism could be responsible for the observed damage to the endothelium, a thin layer of cells that lines the inner surface of a vessel wall. Kobayashi *et al.* [72] subsequently built on this work by examining the effects of tissue density and stiffness in the inviscid case. Axisymmetric simulations of shock-induced bubble collapse were performed near a tissue layer governed by the stiffened gas equation of state (EOS). Several common tissues and tissue simulants, including fat, liver and a gelatin/water mixture were modeled by matching their density and sound speed. Only minor variations in penetration depth were noted across the different materials.

1.3 Contributions and outline

In the present work, we build upon the computational efforts of Freund *et al.* [43] and Kobayashi *et al.* [72] and parametrically study the three-dimensional (3D) shock-induced bubble collapse in a vessel phantom, as well as in a free-field, in an effort to correlate the resulting flow features to the damage potential of the collapse and jetting mechanisms. Resultantly, the main contributions of this thesis are:

- Development and verification of a high-order accurate, quasi-conservative, shock- and interface-capturing numerical scheme for the simulation of viscous and compressible multicomponent flows.
- Characterization of the shock-bubble-vessel interaction as a function of vessel wall pressures and displacements, across a parameter space that includes the geometric configuration of the problem as well as estimates of tissue viscosity.
- Development of a methodology to extract the time-dependent, finite strain fluid deformations from a 3D flow by utilizing particle tracking.
- Characterization of the finite strain flow deformations resulting from the shock-induced collapse of a bubble in the free-field as a function of shockwave pressure.
- Correlation of vessel wall pressures and displacements, as well as finite strain flow deformations, to vascular damage potential of the collapse and jetting mechanisms.
- Estimates of the minimum bubble sizes needed to rupture the blood vessels in the microvasculature as a function of the estimates of tissue viscosity and elasticity.

The remainder of this work is organized as follows. In Chapter 2, the physical model is first motivated by a discussion on the origin and size of preexisting bubbles in the microvasculature, as well as the structure and material properties of the latter, with a special emphasis on the physics of importance when the two interact during SWL treatment. Subsequently, the governing equations for viscous and compressible multicomponent flows are introduced and modeling considerations for the contents of the bubble, the surrounding blood, and soft tissue are discussed. In Chapter 3, the numerical method utilized to simulate the shock-induced collapse of a bubble in a vessel phantom and free-field is derived and verified, with challenging 1D, 2D and 3D test cases considered. The results of the simulations are presented in Chapter 4, outlining the differences between the collapse of a bubble in a free-field and a vessel phantom, as well as discussing how vascular damage potential is expected to vary as a function of the problem geometry and tissue viscosity. Lastly, in Chapter 5, finite strain flow deformations are extracted from free-field collapse simulations in order to estimate the minimum bubble sizes that can result in vascular rupture during collapse and jetting. A spherical bubble dynamics model and a jetting model are utilized to account for the effects of tissue viscosity and elasticity in the results. Concluding remarks and suggestions for future work are made in Chapter 6.

Chapter 2

Physical model

2.1 Problem description

2.1.1 Origin and size distribution of bubbles in tissue

In SWL, preexisting bubbles originate as cavitation nuclei and grow more numerous, as well as larger, as the treatment progresses [91]. These nuclei are present in the blood stream even under normal physiological conditions, *i.e.* prior to the start of the treatment, and are the product of homogeneous and heterogeneous nucleation [10]. Their initial distribution, however, is thought to be scarce, at most 2.7 nuclei per liter of blood [18], and their size small, at most 1 μm in diameter [10]. But with ongoing treatment, bubble splitting is thought to grow the population of these nuclei, while rectified diffusion is anticipated to increase their size [44]. Bubbles $\mathcal{O}(10)$ μm in diameter can be expected once extensive cavitation and injury are detected during treatment [32, 44].

It is hypothesized then that the bubble diameters for which a shock-induced collapse might result in injury lie between 1 and 100 μm. The lower bound is given by the largest estimated bubble size that might be available under normal physiological conditions, while the upper bound is approximately the largest bubble size that can be expected upon the onset of extensive cavitation. Presently, the focus is further narrowed down to bubble sizes that can fit inside the average lumen diameter of the confining microvasculature, the structure of which is discussed next.

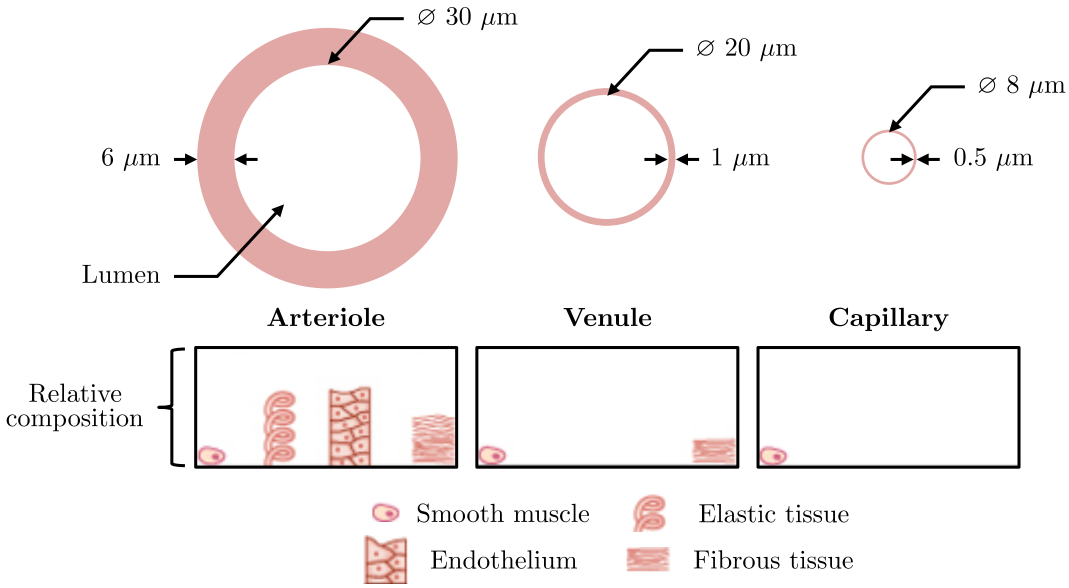

Figure 2.1: The average inner diameter, or lumen diameter, and average wall thickness of arterioles, venules and capillaries. The depicted dimensions of the vessels are scaled correctly with respect to one another. The relative soft tissue composition of the vessel walls is also indicated, with the contribution of the basement membrane difficult to visualize, and thus neglected, on this scale. The figure is adapted from Burton [15] and Koeppen and Stanton [74].

2.1.2 Structure and material properties of the microvasculature

The microvasculature of the kidney is particularly susceptible to cavitation damage during SWL [35, 114], presumably because the size and supporting structure of small blood vessels is insufficient to either accommodate or suppress the growth and collapse of cavitation bubbles [19, 118]. Small blood vessels are comprised of capillaries, venules and arterioles, whose lumen and walls are on average only 8, 20 and 30 μm in diameter and 0.5, 1 and 6 μm in thickness [74], see Figure 2.1. Capillaries are expected to be the most fragile of the three vessels, with a wall composed of only endothelial cells mounted on a basement membrane. Venules, on the other hand, are anticipated to be stronger than capillaries due to the presence of an additional wall layer comprised of fibrous tissue, but weaker than arterioles, whose vessel wall, in addition to a layer of fibrous tissue, is also comprised of a thick layer of smooth muscle and elastic tissue. The blood vessels are also provided limited support by the surrounding connective tissue, see Koeppen and Stanton [74] for further details on the microvascular anatomy. The present aim is to establish reasonable estimates for the material properties of the structural components of microvessels.

A significant obstacle to doing so, however, is the complex, nonlinear, viscoelastic response of soft tissue, which is dependent on both strain and strain rate. Specifically, soft tissue behaves like a non-Newtonian fluid, with a viscosity that usually decreases with increasing strain rate and an elasticity that typically increases with increasing strain and/or strain rate [38, 95, 105, 115]. Both the viscosity and elasticity of tissue can then be expected to vary across several orders of magnitude during the shock-induced collapse of a bubble in a blood vessel [41], which will span infinitesimal to finite tissue strains, and easily achieve strain rates beyond the megascale, based on the bubble sizes and shockwave strengths expected in clinical SWL applications[33]. Establishing estimates for the material properties of the structural components of microvessels thus requires material testing results across a broad range of deformations and deformation rates, which unfortunately are only available for certain tissues and even then, only for a narrow range of strains and strain rates. Consequently, the available data are utilized here only to establish reasonable estimates for the values of tissue viscosity and elasticity that could be expected during shock-induced collapse in SWL.

Material testing results indicate that the first structurally important layer in the microvasculature is the basement membrane, which has a remarkably high stiffness for a biological material [104, 115]. Indeed, for capillaries and venules in *ex vivo* rabbit kidney with a scrubbed endothelium, Welling *et al.* [115] reports a Young's modulus of $Y = 2 - 5$ MPa for low strains and $Y = 20 - 30$ MPa for high strains under quasi-static distention, with only negligible deviations in the measured moduli noted in the cases with an intact endothelium. The basement membrane, however, is approximately only 0.1 μm thick and typically only constitutes a small fraction of the vessel wall [104, 115]. *In vivo* distensibility experiments in cat mesentery at low strains and strain rates suggest elastic moduli for the whole wall that are an order of magnitude smaller, $Y = 0.37$ MPa for capillaries and $Y = 0.39$ MPa for venules [104]. At small strains but fast strain rates, $6 - 20$ MHz, the ultrasound measurements of Yang and Church [116] on the *ex vivo* porcine kidney capsule exhibit a comparable stiffness, $Y = 0.546$ MPa, but can be expected to be an order of magnitude smaller at lower strain rates, $\mathcal{O}(10)$ Hz, according to the parallel plate rheometer experiments on the *ex vivo* porcine kidney cortex of Nasseri *et al.* [87]. The experiments of Nasseri *et al.* also suggest that tissue viscosity at such small strain rates is quite large, $\mu_{\mathrm{t}} = \mathcal{O}(10)$ Pa·s, but is shown to decrease significantly at the rapid strain rates utilized by Yang and Church, who measured $\mu_{\mathrm{t}} = 0.0046$ Pa·s. A recent numerical study by Hosseinkhah *et al.* [57], however, which fitted a linear viscoelastic model to the relaxation data of Chen *et al.* [23] for a venule in *ex vivo* rat mesentery distended by an ultrasound activated contrast agent at 1 MHz, suggests that $\mu_{\mathrm{t}} = 0.9$ Pa·s, which is arguably a more relevant measurement to the present study. Based on these measurements, tissue viscosities and elasticities in the ranges $0.01 \leq \mu_{\mathrm{t}} \leq 10$ Pa·s and $0.01 \leq G \leq 10$ MPa will be considered, where G is the shear modulus and is approximately equal to one third of Young's modulus since tissue is nearly incompressible. The switch to the shear modulus is motivated by the convention of describing non-Newtonian fluid elasticity.

Lastly, the characterization of the material response of microvessels is completed with a discussion of the structural failure thresholds of tissue, which though not well understood for bubbles collapsing in the vasculature, have been studied on the macroscale, predominantly with standard uniaxial loading tests in *ex vivo* tissue. Though such tests are typically carried out at strain rates significantly slower than would be expected in SWL, the rupture strain, *i.e.* ultimate strain, is shown to decrease as a function of increasing strain rate for individual tissues [38, 95, 105], such that the available experimental data can be used to establish conservative estimates.

Overall, it is expected that tissue can deform significantly prior to rupturing. Uniaxial tensile tests of the porcine renal capsule at a strain rate of 200 s^{-1} suggest an ultimate Green-Lagrange strain of $E_{\mathrm{u}} = 0.29$ [105], which is comparable to that observed for the human liver parenchyma at a strain rate of 10 s^{-1}, where $E_{\mathrm{u}} = 0.24$ [95], Tissue seems more difficult to rupture under compression, however, with analogous tests of the human liver parenchyma showing an ultimate strain of $E_{\mathrm{u}} = -0.35$ at a nearly equivalent deformation rate, 7 s^{-1} [95]. The porcine kidney cortex fails at approximately the same level of deformation as the human liver parenchyma, but at a much slower strain rate, $\mathcal{O}(10^{-1})$ s^{-1} [38]. Finally, in the study of the distensibility of basement membranes in *ex vivo* rabbit kidney, Welling *et al.* [115] reports two cases in which the membrane ruptured. An average of the two samples suggests an ultimate strain of $E_{\mathrm{u}} = 0.23$ for the basement

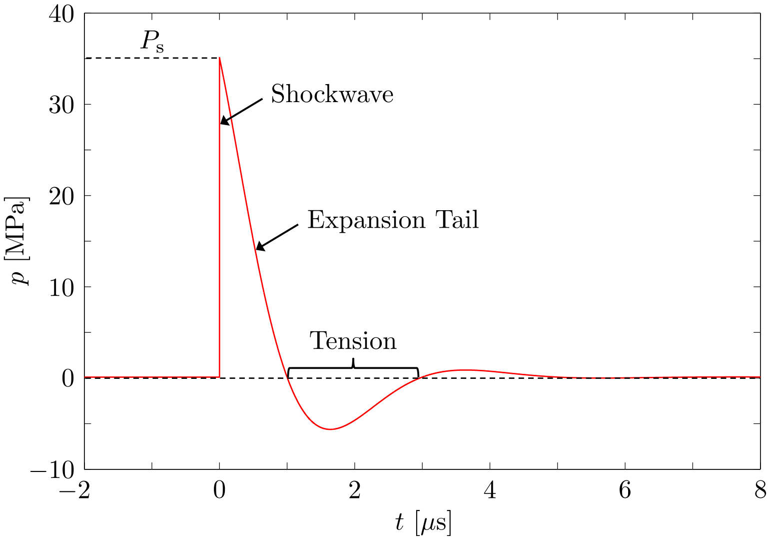

Figure 2.2: Qualitative pressure waveform of a typical lithotripter at its focal region. The compression front, or shockwave, along with the expansion tail, which includes a tensile component, are indicated. The amplitude of the shockwave is given by P_s. The pulse is generated with the model of Church [24].

membrane under quasi-static loading. All of these measurements will be utilized in establishing a range for the vascular rupture criterion, see Section 5.2.

2.1.3 Characteristics of the lithotripter waveform

Recall from Section 1.1 that the lithotripter pulse is composed of both a compression front and an expansion tail that includes a tensile component. In Figure 2.2, these features are illustrated with a qualitative pressure waveform taken at the focal point of a typical lithotripter. *In vitro*, the compression front, or shockwave, has a fast rise time, $\mathcal{O}(10)$ ns in water, while the subsequent expansion and release of pressure to ambient conditions occurs on the microscale, $\mathcal{O}(1)$ μs [26]. As the lithotripter pulse travels through tissue, the amplitude of the shockwave is attenuated by approximately 30%, and the rise time nearly doubles, though it remains on the nanoscale. The expansion tail, on the other hand, is largely unaffected, as is the waveform qualitatively, due to negligible dispersive effects of tissue inhomogeneities [27].

The interaction of the lithotripter pulse with a bubble first results in its shock-induced collapse and is immediately followed by its growth due to the expansion tail. For bubble diameters under consideration, $1 \leq D_\mathrm{b} \leq 30$ μm, the collapse occurs in $\mathcal{O}(10)$ ns in the free-field and can be expected to be on the same order inside a blood vessel, as the confinement offered by the latter is unlikely to be sufficient to significantly suppress the volumetric change [41, 43]. The collapse of the bubble therefore occurs on the same time scale as the shockwave and the expansion component of the lithotripter pulse should only play an important role in the dynamics of bubble growth and not during the collapse phase. In the study of shock-induced collapse then, only the compression front is considered and typical SWL pressures in the range $30 \leq P_\mathrm{s} \leq 110$ MPa are investigated [26]. The attenuation of the shockwave amplitude in tissue is presently unaccounted for, since as to date, only one study has investigated the effect.

2.1.4 Physics of shock-induced collapse in microvessels

Following the model of Church and Yang [25], which describes spherical bubble dynamics in a liquid confined by a linear viscoelastic material, see Section 5.5.1 for details, the physics of the shock-induced collapse of a bubble in a blood vessel can be expected to be governed by several nondimensional parameters. These include the Reynolds numbers in the liquid, "l", and tissue, "t"; $Re_\mathrm{l} = \rho_\mathrm{l} U D_\mathrm{b} / \mu_\mathrm{l}$ and $Re_\mathrm{t} = \rho_\mathrm{l} U D_\mathrm{b} / \mu_\mathrm{t}$; the Weber number, $We = \rho_\mathrm{l} U^2 D_\mathrm{b} / \sigma$; and the Cauchy number, $Ca = \rho_\mathrm{l} U^2 / G$, where ρ_l is the density of the liquid, U is the characteristic velocity and σ is the surface tension coefficient between the contents of the bubble and surrounding liquid. The dimensionless quantities are arbitrarily defined with respect to the density of the liquid, which is presumably blood, and has approximately the same density as tissue [36]. Following other studies of shock-induced collapse [33, 43, 72], the characteristic velocity is given by $U = \sqrt{P_\mathrm{s} / \rho_\mathrm{l}}$. It is akin to a sound speed, which again is approximately the same in both tissue and blood [36]. The Reynolds, Weber and Cauchy numbers correspond to the ratios of inertial to viscous, capillary and elastic forces, respectively, and describe the relative importance of these effects on the dynamics of bubble and tissue. Other effects, such as mass and heat transfer, characterized by the Schmidt and Prandtl dimensionless numbers, need not be considered based on the length of their time scales, which are expected to be much greater than that of shock-induced collapse [66].

The relevant dimensionless groups are first studied in the case of the shock-induced collapse of a bubble in the absence of the vessel. Under such circumstances and under typical clinical SWL conditions, $30 \leq P_\mathrm{s} \leq 110$ MPa [26], the dynamics of the bubble are expected to be primarily driven by inertia [66]. Indeed, based on the density and viscosity of blood, $\rho_\mathrm{l} = 1027$ kg/m^3 and $\mu_\mathrm{l} = 0.001$ Pa·s [12, 36], the Reynolds number, Re_l, is expected to range between $\mathcal{O}(10^2)$ and $\mathcal{O}(10^4)$ across the estimated bubble sizes, $1 \leq D_\mathrm{b} \leq 30$ μm, and typical shockwave amplitudes in SWL. This suggests that the effects of viscosity, compared to the effects of inertia, should play a minor role in the dynamics of the bubble. Similarly, inertial forces are anticipated to play a more prominent role than capillary forces, given the surface tension coefficient between blood and air, $\sigma = 0.056$ N/m [58], which yields a Weber number between $\mathcal{O}(10^2)$ and $\mathcal{O}(10^4)$.

In the presence of a blood vessel, however, the dynamics of the bubble may no longer be inertia driven. In fact, the highest estimate of tissue viscosity considered, $\mu_\mathrm{t} = 10$ Pa·s, suggests the possibility of a Reynolds number, Re_t, in the Stokes' flow regime, *i.e.* $\mathcal{O}(10^{-2})$, while the highest estimate of tissue elasticity, $G = 10$ MPa, yields a Cauchy number that is $\mathcal{O}(1)$ – a flow regime where the contributions of elastic and inertial forces are comparable. An inertial response can still be expected, however, for the lowest estimates of tissue viscoelasticity considered, $\mu_\mathrm{t} = 0.01$ Pa·s and $G = 0.01$ MPa, which suggest Reynolds and Cauchy numbers that are $\mathcal{O}(10^3)$ and $\mathcal{O}(10^4)$, respectively.

Of course, a significant caveat in the above analysis is that it does not account for the change in the relative contributions of inertia, surface tension, viscosity, and elasticity as a function of time. In particular, beyond the collapse phase, the jetting of the bubble will introduce finer spatial scales across which viscous dissipation and surface tension will play an increasingly larger role. The viscoelastic response of tissue can also be expected to become stronger at later times, with the progressive arrest of the jetting of the bubble. Nevertheless, the magnitude ranges of the Reynolds, Weber and Cauchy numbers based on the estimated bubble sizes and tissue properties suggest the possibility of a flow regime that, at least during the early stages of shock-induced collapse, is inertia driven. The latter also suggest that in the case that tissue viscoelasticity cannot be neglected, tissue viscosity will play a larger role in suppressing the dynamics of the bubble than its elasticity. Both of these assertions are further investigated and verified in Sections 4.3.7 and 5.5.2.

2.2 Idealized problem

2.2.1 Shock-induced collapse in a free-field

As discussed in Section 2.1.4, the smallest estimates of tissue viscosity and elasticity, as well as the negligible mismatch in density and sound speed between blood and tissue, seem to indicate that the simplest problem that can be considered in the study of shock-induced collapse in a blood vessel is actually the collapse of a bubble in the free-field. Though the study of such a problem may initially appear of limited value, its results are presently utilized not only to understand fundamental shock-bubble dynamics, Section 4.2, which in the limit that tissue can be neglected are not expected to be any different inside a blood vessel, but also to fit a model of jet propagation in viscous tissue so to draw conclusions regarding vascular injury in the jetting phase as a function of tissue viscosity, Section 5.6. Finally, finite strain deformations are also post-processed from the flow field surrounding the bubble, Section 5.3, to provide a means of direct comparison with the estimated ultimate strains of tissue.

The schematic of the initial condition and computational domain for the shock-induced bubble collapse in a free-field is shown in Figure 2.3. The problem is characterized by the initial diameter of the bubble, D_b, as well as the shockwave and ambient pressures, P_s and P_o, respectively. In the schematic, the shockwave, modeled as a step discontinuity, is shown traveling in blood toward the bubble, a spherical cavity in the plasma. Reflective boundary conditions (RBC) are utilized to describe the symmetry of the problem across the x-y and x-z planes of the computational domain, while non-reflective boundary conditions (NRBC) describe the free-field. Further modeling and numerical considerations for the problem are discussed in Section 2.3 and Chapter 3, respectively.

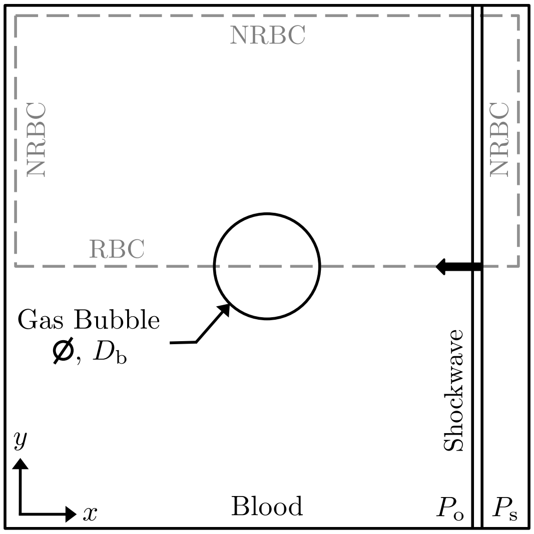

Figure 2.3: Schematic of the 3D initial condition and computational domain (– –) for the shock-induced collapse of a bubble in a free-field in the x-y plane of symmetry.

2.2.2 Shock-induced collapse in a vessel phantom

In addition to the study of shock-induced collapse in a free-field, the collapse in a vessel phantom is also considered. In this case, a tissue simulant is added to the free-field to confine the gas bubble and surrounding blood. The simulant matches the density, sound speed, and viscosity of tissue but neglects its elasticity, as elastic effects are expected to play a minor role in suppressing vascular deformations compared to viscous effects, see Section 2.1.2. The tissue simulant also behaves like a fluid, as motivated by the rapid strain rates anticipated during shock-induced collapse. The primary motivation for the study of this problem is the characterization of the shock-vessel-bubble interaction as a function of geometry, Sections 4.3.4–4.3.6, and tissue viscosity, Section 4.3.7. In contrast to the study of free-field collapse, vessel wall pressures and displacements are utilized in the present case to characterize the vascular damage potential of the collapsed bubble.

The schematic of the initial condition and computational domain for the shock-induced collapse in a vessel phantom is shown in Figure 2.4. The problem is characterized by the initial bubble and vessel diameters, D_{b} and D_{v}, the x- and y-coordinates of the bubble centroid, H_x and H_y, the shockwave and ambient pressures, P_{s} and P_{o}, and finally, the tissue viscosity, μ_{t}. In the schematic, the shockwave is shown traveling in tissue toward a cylindrical, blood-filled cavity that contains a

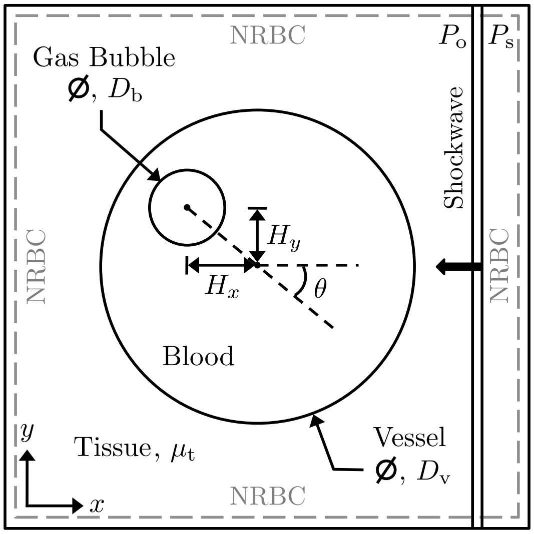

Figure 2.4: Schematic of the 3D initial condition and computational domain (– –) for the shock-induced collapse of a bubble in a vessel phantom in the x-y plane of symmetry.

gas bubble – a spherical cavity in blood. A RBC is utilized to describe the symmetry of the problem across the x-y plane of the computational domain, while NRBCs extend the tissue to infinity. Further modeling and numerical considerations for the problem are discussed in Section 2.3 and Chapter 3, respectively.

2.3 Governing equations

2.3.1 Five-equation model

In the absence of mass transfer, the shock-induced collapse of a bubble inside a blood vessel may be modeled as a multicomponent flow – a multiphase flow for which the individual species, *i.e.* the gas in the bubble, the blood in the vessel and the surrounding tissue, are immiscible. By further neglecting the effects of surface tension and heat transfer, the motion of each species in the flow may be described by the compressible Navier-Stokes equations. For two fluids, this constitutes a five-equation model for viscous and compressible multicomponent flows, Equations (2.1)–(2.5), which was first introduced in its inviscid form by Allaire *et al.* [3] and Massoni *et al.* [83] and subsequently extended to include viscous effects by Perigaud and Saurel [90]. The model consists of two continuity equations, Equations (2.1) and (2.2); a momentum and an energy equation, Equations (2.3) and (2.4), respectively; as well as an advection equation for the volume fraction of one of the two fluids, Equation (2.5); so to identify their material interface:

$$\frac{\partial(\alpha_1\rho_1)}{\partial t} + \nabla\cdot(\alpha_1\rho_1\mathbf{u}) = 0, \tag{2.1}$$

$$\frac{\partial(\alpha_2\rho_2)}{\partial t} + \nabla\cdot(\alpha_2\rho_2\mathbf{u}) = 0, \tag{2.2}$$

$$\frac{\partial(\rho\mathbf{u})}{\partial t} + \nabla\cdot(\rho\mathbf{u}\mathbf{u} + p\mathbf{I} - \mathbf{T}) = \mathbf{0}, \tag{2.3}$$

$$\frac{\partial E}{\partial t} + \nabla\cdot((E+p)\,\mathbf{u} - \mathbf{T}\cdot\mathbf{u}) = 0, \tag{2.4}$$

$$\frac{\partial\alpha_1}{\partial t} + \mathbf{u}\cdot\nabla\alpha_1 = 0, \tag{2.5}$$

where ρ is the density, $\mathbf{u} = (u,v,w)^{\mathrm{T}}$ is the velocity, p is the pressure, E is the total energy, α is the volume fraction, $\mathbf{T}$ is the viscous stress tensor, and the subscripted variables indicate those quantities which are specific to the individual fluids. The viscous stress tensor is given by

$$\mathbf{T} = 2\mu\left(\mathbf{D} - \frac{1}{3}(\nabla\cdot\mathbf{u})\,\mathbf{I}\right), \tag{2.6}$$

where μ is the shear viscosity and

$$\mathbf{D} = \frac{1}{2}\left(\nabla\mathbf{u} + (\nabla\mathbf{u})^{\mathrm{T}}\right) \tag{2.7}$$

is the deformation rate tensor. The shear viscosity of each fluid is assumed to be constant and the effects of bulk viscosity are neglected. The five-equation model is easily extended to account for additional fluids by supplementing the equations of motion with a continuity equation and a volume fraction advection equation for each new fluid that is added. For the sake of conciseness, however, only the case with two fluids is presently discussed, with extensions to the more general case considered when necessary.

Though other models may be utilized to describe viscous and compressible multicomponent flows, the five-equation model is chosen because it meets several key criteria, foremost of which is that it is cast in a quasi-conservative form that ensures that when using a shock- and interface-capturing scheme, such as that developed in Chapter 3, critical physical quantities are conserved, while spurious oscillations at the material interfaces are avoided, see Allaire *et al.* [3]. The compressible Navier-Stokes equations, Equations (2.1)–(2.4), are written in conservative form and conserve the mass of the individual fluids, as well as the total momentum and energy. The advection equation for the volume fraction, on the other hand, Equation (2.5), is not written in conservative form. This choice, along with that of the transported quantity, ensures that the advection equation is consistently coupled with the compressible Navier-Stokes equations so as to lead to an oscillation-free behavior at material interfaces.

There are also multiple alternatives to the five-equation model that meet the above criteria. The differences between these models and the present equations of motion range from conserving the total mass of the two fluids, versus the mass of each, to transporting alternate scalar quantities, most notably functions of the EOS parameters, versus the volume fraction [1, 97, 101–103]. However, in an interface-capturing method, the former difference will typically lead to mass transfer between the supposedly immiscible fluids, while advecting functions of the EOS parameters will not only lead to the dependence of the complexity of the equations of motion on the EOS, but can also result in a non-uniquely defined material interface position [67]. The latter two issues are further exacerbated when more intricate EOS are considered and/or there are more than two fluids in the flow.

2.3.2 Stiffened gas EOS

In order to provide closure to the five-equation model, it is necessary to specify the appropriate EOS, relating the density, internal energy, and pressure for the gas in the bubble, the blood inside the vessel and the surrounding tissue. The gas in the bubble is usually a mixture of vapor and non-condensible gas, the ratio between which is dictated by the effects of mass transfer. Since those effects are neglected here, the bubble is assumed to be strictly composed of air, a common modeling assumption for the type of problem under consideration and one to which the jetting dynamics are not sensitive [43]. The blood and tissue are modeled by water and 10% gelatin, respectively,

Table 2.1: Properties of air, helium, water and 10% gelatin at normal temperature and pressure. These include the density, ρ, the sound speed, c, and the stiffened gas EOS fitting parameters, γ and π_∞.

Fluid	ρ [kg/m^3]	c [m/s]	γ	π_∞ [Pa]
Air	1.204	343	1.40	0
Helium	0.166	1008	1.67	0
Water	1000	1450	6.12	3.43×10^8
10% Gelatin	1030	1553	6.72	3.70×10^8

since water closely approximates the density and sound speed of plasma and 10% gelatin those of soft tissue, like the liver and kidney [50]. Each of these components may then be described by the stiffened gas EOS [40], which has widely been utilized in compressible multicomponent flow applications to simultaneously describe pure gases, liquids and solids [30, 96, 97]:

$$p = (\gamma - 1)\,\rho\varepsilon - \gamma\pi_\infty, \tag{2.8}$$

where ε is the specific internal energy, with $\rho\varepsilon = E - \frac{1}{2}\rho\mathbf{u}\mathbf{u}$, γ and π_∞ are fitting parameters deduced from fluid shockwave Hugoniot data, and $c = \sqrt{\gamma\,(p + \pi_\infty)\,/\rho}$ is the EOS sound speed. The properties of air, water and 10% gelatin are tabulated in Table 2.1, along with those of helium, which will be utilized in the verification of the numerical scheme in Section 3.6. The fitting parameters for water and 10% gelatin are obtained based on the shockwave Hugoniot data of Gojani *et al.* [49], following the fitting procedure of Cocchi *et al.* [30]. In the case of air and helium $\pi_\infty = 0$ Pa and the stiffened gas EOS reduces to the ideal gas law, with γ the specific heat ratio.

2.3.3 Mixture relationships

The closure of the five-equation model is completed with a set of rules for the properties of fluid mixtures, which will arise in simulations as an artifact of numerical diffusion and are not a product of mixing on a molecular level. The mixtures of fluids are confined to thin regions of space neighboring material interfaces and despite being artificial, their properties must be determined in a thermodynamically consistent manner in order to avoid introducing spurious oscillations in simulations. It is common practice to define the following rules for the mixture volume fraction, Equation (2.9), density, Equation (2.10), and internal energy, Equation (2.11):

$$1 = \alpha_1 + \alpha_2, \tag{2.9}$$

$$\rho = \alpha_1 \rho_1 + \alpha_2 \rho_2, \tag{2.10}$$

$$\rho\varepsilon = \alpha_1 \rho_1 \varepsilon_1 + \alpha_2 \rho_2 \varepsilon_2. \tag{2.11}$$

Two additional rules may then be derived by assuming that each pure fluid of which the mixture is composed is at the same pressure. This is referred to as the isobaric assumption and it is consistent with the modeled flow physics in that in the absence of surface tension the pressure across an isolated material interface should not vary, see Allaire *et al.* [3] for a more rigorous consistency analysis. Combining Equations (2.8) and (2.11) with the isobaric assumption yields the mixture rules for two functions of the stiffened gas EOS parameters:

$$\Gamma = \alpha_1 \Gamma_1 + \alpha_2 \Gamma_2, \tag{2.12}$$

$$\Pi_\infty = \alpha_1 \Pi_{\infty,1} + \alpha_2 \Pi_{\infty,2}, \tag{2.13}$$

where $\Gamma = 1/(\gamma - 1)$ and $\Pi_\infty = \gamma\pi_\infty/(\gamma - 1)$. The closure of the five-equation model is finalized by defining a mixture rule for the coefficient of shear viscosity. Following Perigaud and Saurel [90], we choose

$$\mu = \alpha_1 \mu_1 + \alpha_2 \mu_2. \tag{2.14}$$

All of the above mixture properties are obtained through the linear combination of the analogous properties of the pure fluids composing it. As such, extending Equations (2.9)–(2.14) to account for additional fluids is straightforward.

Table 2.2: Dimensionless parameter space for the study of the shock-induced collapse of a bubble in a free-field and inside a vessel phantom. Parametric studies are carried out for the shockwave strength, $P_\mathrm{s}/P_\mathrm{o}$, in the free-field, and for vessel confinement, D_v^*, vessel proximity, H_x^*, shockwave angle, $\theta = \tan^{-1}(H_y^*/H_x^*)$, and tissue viscosity, Re_t, in the vessel phantom.

	Free-field	Vessel phantom			
Parameter	Shockwave strength	Vessel confinement	Vessel proximity	Shockwave angle	Tissue viscosity
$P_\mathrm{s}/P_\mathrm{o}$	$[296, 1086]$	395	395	395	395
D_v^*	∞	$[1.1, 4.0]$	3.0	3.0	1.3
H_x^*	0.00	0.00	$[-0.75, 0.75]$	$\sqrt{0.75^2 - {H_y^*}^2}$	0.00
H_y^*	0.00	0.00	0.00	$[0.00, 0.75]$	0.00
Re_t	∞	∞	∞	∞	$[10, \infty)$

2.3.4 Nondimensionalization and parameter space

In the study of the shock-induced bubble collapse in both a free-field and a vessel phantom, the five-equation model is solved in dimensionless form – nondimensionalized by the diameter of the bubble, D_b, the density of water, ρ_l, the shockwave pressure, P_s, and the characteristic velocity, $U = \sqrt{P_\mathrm{s}/\rho_\mathrm{l}}$. The resulting change of variables is given by

$$t^* = t\frac{U}{D_\mathrm{b}}, \quad \mathbf{x}^* = \frac{\mathbf{x}}{D_\mathrm{b}}, \quad \rho^* = \frac{\rho}{\rho_\mathrm{l}}, \quad \mathbf{u}^* = \frac{\mathbf{u}}{U}, \quad p^* = \frac{p}{P_\mathrm{s}}, \tag{2.15}$$

where a superscripted star denotes a dimensionless quantity. The purpose of the nondimensionalization is to minimize the number of parameters governing the physics of each of the problems. The physics of shock-induced bubble collapse in a free-field are governed by a single dimensionless parameter, the shockwave to ambient pressure ratio, $P_\mathrm{s}/P_\mathrm{o}$. The physics of the bubble collapse in a vessel phantom, on the other hand, are governed by four additional parameters, including the vessel to bubble diameter ratio, D_v^*, the ratio of the x-coordinate of the bubble to its diameter, H_x^*, the tissue Reynolds number, Re_t, and the shockwave angle, $\theta = \tan^{-1}(H_y^*/H_x^*)$.

A parametric study is carried out across each dimensionless parameter, as detailed in Table 2.2, where the span of the parameter space is not only a product of the discussion of the bubble sizes, vascular structure and physics of shock-induced collapse in microvessels of Section 2.1, but also constrained by resolution and, more generally, computational cost considerations. In the case of free-field collapse, the shockwave to ambient pressure ratio spans the typical shockwave pressures of clinical SWL, 30 to 110 MPa. The parametric studies of collapse in a vessel phantom, on the other hand, are carried out at a single shockwave strength corresponding to 40 MPa, the output of a widely utilized clinical and research lithotripter, the Dornier HM3 [28]. In the study of vessel confinement, vessel to bubble diameter ratios below 1.1 are not considered in order that the bubble-vessel interaction may properly be resolved, while ratios larger than 4.0 are neglected by merit of negligible interaction. The range in the study of vessel proximity, on the other hand, is essentially bound by the dimensionless vessel diameter. Finally, since the parametric study of shockwave angle imposes a decreased degree of problem symmetry in simulations and that of tissue viscosity requires simulations to take small time steps at large viscosities, only $0 \leq \theta \leq \pi/2$ and $Re_{\mathrm{t}} \geq 10$, *i.e.* $\mu_{\mathrm{t}} \geq 0.4$ Pa·s, are presently considered in order to reduce computational cost.

Chapter 3

Numerical method

3.1 Numerical simulations of interfaces and shockwaves

Following the scaling analysis of Section 2.1.4, recall that both the shock-induced collapse of a bubble in the free-field and inside a vessel phantom may be viewed as a multiphase flow and in particular, a multicomponent flow, since the mass diffusion between the pure fluids is expected to be negligible. A primordial feature of the multicomponent flows in this study is the interaction between material interfaces and shockwaves, which presents unique challenges to the numerical method. Indeed, the latter should satisfy three important criteria. It should maintain discrete conservation of the total mass, momentum and energy to correctly identify the position of important flow features. It should not generate spurious oscillations across either shockwaves or material interfaces to preserve numerical stability. And finally, for efficiency, it should be high-order accurate in smooth regions of the flow, away from discontinuities. Attempts at designing numerical schemes that meet these criteria can be classified into two categories based on their treatment of material interfaces. They are the interface-tracking and the interface-capturing methods. The advantages and disadvantages of each method are discussed in Section 3.1.1, with the present numerical scheme introduced in Section 3.1.2.

3.1.1 Interface-tracking versus interface-capturing methods

Interface-tracking methods have the distinct advantage of treating material interfaces in a natural way, as sharp discontinuities. Arbitrary Lagrangian-Eulerian [81], free-Lagrange [7], front-tracking [29, 46, 47, 107] and level set/ghost fluid [2, 39, 59, 60, 77–79, 86, 88] schemes all belong in this category. Their sharp treatment of material interfaces enables two fluids sharing an interface to have starkly different EOS and while at mechanical equilibrium, generally avoid the onset of spurious oscillations at the interface. They also have the advantage of rendering the implementation of any interfacial physics rather straightforward. Their primary drawback, however, is that they are typically not discretely conservative at material interfaces, which may lead them to incorrectly predict their position, as well as those of shockwaves, if the two flow features happen to interact during the computation.

Achieving discrete conservation in interface-capturing methods, on the other hand, is relatively simple. It is sufficient to solve the continuity, momentum and energy equations in conservative form, while relaxing the sharp character of material interfaces and thus allowing them to numerically diffuse over a small but finite region [1, 3, 64, 67, 82, 83, 90, 97, 101–103]. This numerical diffusion, unfortunately, gives rise to unphysical mixtures of fluids during computations, which, if not treated in a thermodynamically consistent manner and evolved in a fashion that is consistent with the continuity, momentum and energy equations, can lead to spurious oscillations at material interfaces. As a result, interface-capturing methods make the implementation of EOS that strongly differ from one another across material interfaces challenging and further, make it nontrivial to simulate a material interface that is simultaneously in mechanical equilibrium and void of spurious oscillations. Attempts to achieve the latter have even led some authors to sacrifice discrete conservation [61, 68, 69, 93].

For both interface-tracking and interface-capturing methods, solutions to the aforementioned problems do exist. Discretely conservative interface-tracking methods have been developed in the past [7, 47, 60, 79, 81] and requirements to consistently treat mixtures of fluids while maintaining oscillation-free material interfaces and discrete conservation in interface-capturing methods are well-understood [1, 64, 67]. In this study, we prefer to develop an interface-capturing framework because achieving discrete conservation in it is straightforward and robust strategies for the treatment of mixtures of fluids and suppression of spurious oscillations at interfaces separating them are readily available. Moreover, we choose to develop an interface-capturing scheme because they generally are more efficient than interface-tracking methods and their complexity does not increase with simulation dimensionality or number of fluids.

3.1.2 A conservative, high-order and non-oscillatory, interface-capturing scheme

In order to simultaneously achieve a discretely conservative, high-order and non-oscillatory interface-capturing scheme, several requirements must be satisfied. As previously mentioned, discrete conservation is the easiest to obtain and merely requires that the mass, momentum and energy equations be solved in conservative form. An oscillation-free behavior, on the other hand, is the most challenging. Foremost, it requires that material interfaces be evolved with an advection equation that is written in non-conservative form and is consistent with the conservation equations for mass, momentum and energy [1]. Mass fractions, volume fractions or specific functions of the EOS parameters are typically evolved. An oscillation-free interface-capturing method also requires that these equations of motion be closed by a thermodynamically consistent set of mixture rules, which are typically derived by assuming that mixtures are in mechanical equilibrium [3]. Care must then be taken when solving the resulting governing equations. They must be cast in a finite-volume framework and discretized with a non-oscillatory spatial and temporal method, with the primitive state variables, rather than the conservative ones, spatially reconstructed [64]. In order to achieve high-order accuracy while maintaining nearly non-oscillatory behavior, weighted essentially non-oscillatory (WENO) spatial reconstructions [8, 56, 62, 80] and total variation diminishing (TVD) Runge-Kutta (RK) time-steppers [51] have been shown to perform well.

An interface-capturing scheme that meets nearly all of the above requirements was developed by Johnsen and Colonius [64] and applied to a compressible multicomponent flow model first introduced by Shyue [101]. The model consists of the Euler system of equations coupled with two advection equations, one for each function of the stiffened gas EOS parameters. To solve it, the numerical scheme of Johnsen and Colonius utilizes a fifth-order finite-volume WENO spatial reconstruction [62], the Harten-Lax-van Leer-contact (HLLC) approximate Riemann solver [111] and a third-order TVD RK time-stepper [51]. The numerical method is discretely conservative and non-oscillatory but unfortunately, despite being advertised as such, is not formally high-order accurate. The authors fail to identify the propagation of a second-order spatial error that arises from the procedure utilized to obtain the cell average primitive variables from their conservative counterparts prior to reconstruction. The problem goes unnoticed in the convergence analysis as a consequence of considering a nearly linear test case. Presently, we propose a fix and extend their numerical framework to the more general five-equation model introduced in Section 2.3, 3D and include viscous effects. The five-equation model is more general than that of Shyue in that it conserves the mass of each fluid in the flow, rather than just the total mass, and advects the volume fraction of each fluid, rather than functions of the stiffened gas EOS parameters. We choose it because it has the distinct advantage of explicitly tracking each fluid in the flow, which facilitates the treatment of mixtures composed of more than two fluids. In order to extend the numerical scheme for this model to 3D, we follow the work of Titarev and Toro [110] on finite-volume WENO schemes for 3D conservation laws. The effects of viscosity are included based on the work of Perigaud and Saurel [90].

For the remainder of this chapter, we proceed as follows. In Section 3.2, we first introduce the finite-volume spatial discretization of the five-equation model, followed by a discussion in Section 3.3 on the flow variables that must be reconstructed to achieve high-order accuracy and oscillation-free behavior. The temporal discretization is then discussed in Section 3.4, with issues of numerical stability addressed in Section 3.5. Several benchmark problems for the numerical scheme in 1D, 2D and 3D are then presented in Section 3.6. The benchmarks validate our numerical method and corroborate its high-order accuracy, discrete conservation and oscillation-free behavior. Lastly, we summarize in Section 3.7.

3.2 Spatial discretization

The five-equation model is a hyperbolic and quasi-conservative system of equations [3] and is well suited for numerical approximation by Godunov-type schemes. The latter are reconstruct-evolve-average methods and rely on reconstructed values of the cell averages of the solution at the cell faces for the determination of the average fluxes at the cell faces, which are subsequently utilized to evolve the cell averages of the solution in time [76, 111]. We seek to design such a method for the five-equation model and have it satisfy three important criteria: high-order accuracy, discrete conservation, and non-oscillatory behavior. We begin by spatially discretizing the equations of motion in their conservation-law form:

$$\frac{\partial \mathbf{q}}{\partial t} + \frac{\partial \mathbf{f}^{\mathrm{a}}(\mathbf{q})}{\partial x} + \frac{\partial \mathbf{g}^{\mathrm{a}}(\mathbf{q})}{\partial y} + \frac{\partial \mathbf{h}^{\mathrm{a}}(\mathbf{q})}{\partial z} = \frac{\partial \mathbf{f}^{\mathrm{d}}(\mathbf{q})}{\partial x} + \frac{\partial \mathbf{g}^{\mathrm{d}}(\mathbf{q})}{\partial y} + \frac{\partial \mathbf{h}^{\mathrm{d}}(\mathbf{q})}{\partial z} + \mathbf{s}(\mathbf{q}), \tag{3.1}$$

where $\mathbf{q}$ is the vector of state variables, $\mathbf{f}$, $\mathbf{g}$ and $\mathbf{h}$ are vectors of fluxes, $\mathbf{s}$ is the vector of source terms and the superscripts “a” and “d” denote advective and diffusive fluxes, respectively, see Appendix A for details. The transport equation for the volume fraction takes a different but mathematically equivalent form in Equation (3.1) compared to in Equation (2.5):

$$\frac{\partial \alpha_1}{\partial t} + \nabla \cdot (\alpha_1 \mathbf{u}) = \alpha_1 \nabla \cdot \mathbf{u}. \tag{3.2}$$

This form was introduced by Johnsen and Colonius [64] and is necessary to later adapt the HLLC approximate Riemann solver to the advection equation. Equation (3.1) is discretized on a finite-volume Cartesian grid by considering an arbitrary cell in the grid and integrating Equation (3.1) over its control volume, $I_{i,j,k}$, denoted by

$$I_{i,j,k} = \left[x_{i-1/2}, x_{i+1/2}\right] \times \left[y_{j-1/2}, y_{j+1/2}\right] \times \left[z_{k-1/2}, z_{k+1/2}\right], \tag{3.3}$$

where i, j and k are the indices of the cell in the x-, y- and z-directions, respectively, and $x_{i\pm1/2}$, $y_{j\pm1/2}$ and $z_{k\pm1/2}$ are the positions of the cell faces. The result of the spatial integration, simplified by the application of the divergence theorem, yields the following semi-discrete form of Equation (3.1):

$$\begin{aligned}\frac{\mathrm{d}\mathbf{q}_{i,j,k}}{\mathrm{d}t} =& \frac{1}{\Delta x_i}\left[\left(\mathbf{f}^{\mathrm{a}}_{i-1/2,j,k} - \mathbf{f}^{\mathrm{a}}_{i+1/2,j,k}\right) - \left(\mathbf{f}^{\mathrm{d}}_{i-1/2,j,k} - \mathbf{f}^{\mathrm{d}}_{i+1/2,j,k}\right)\right] \\ &+ \frac{1}{\Delta y_j}\left[\left(\mathbf{g}^{\mathrm{a}}_{i,j-1/2,k} - \mathbf{g}^{\mathrm{a}}_{i,j+1/2,k}\right) - \left(\mathbf{g}^{\mathrm{d}}_{i,j-1/2,k} - \mathbf{g}^{\mathrm{d}}_{i,j+1/2,k}\right)\right] \\ &+ \frac{1}{\Delta z_k}\left[\left(\mathbf{h}^{\mathrm{a}}_{i,j,k-1/2} - \mathbf{h}^{\mathrm{a}}_{i,j,k+1/2}\right) - \left(\mathbf{h}^{\mathrm{d}}_{i,j,k-1/2} - \mathbf{h}^{\mathrm{d}}_{i,j,k+1/2}\right)\right] + \mathbf{s}_{i,j,k},\end{aligned} \tag{3.4}$$

where the state variables and the source term are now averages over the cell volume, while the flux vectors are averages over the cell faces. These spatial averages take the following form:

$$\mathbf{q}_{i,j,k} = \frac{1}{V_{i,j,k}} \int_{z_{k-1/2}}^{z_{k+1/2}} \int_{y_{j-1/2}}^{y_{j+1/2}} \int_{x_{i-1/2}}^{x_{i+1/2}} \mathbf{q}\left(x, y, z, t\right)\, \mathrm{d}x\, \mathrm{d}y\, \mathrm{d}z, \tag{3.5}$$

$$\mathbf{f}^{\mathrm{a}}_{i+1/2,j,k} = \frac{1}{\Delta y_j \Delta z_k} \int_{z_{k-1/2}}^{z_{k+1/2}} \int_{y_{j-1/2}}^{y_{j+1/2}} \mathbf{f}^{\mathrm{a}}\left(\mathbf{q}\left(x_{i+1/2}, y, z, t\right)\right)\, \mathrm{d}y\, \mathrm{d}z, \tag{3.6}$$

$$\mathbf{s}_{i,j,k} = \frac{1}{V_{i,j,k}} \int_{z_{k-1/2}}^{z_{k+1/2}} \int_{y_{j-1/2}}^{y_{j+1/2}} \int_{x_{i-1/2}}^{x_{i+1/2}} \mathbf{s}\left(\mathbf{q}\left(x, y, z, t\right)\right)\, \mathrm{d}x\, \mathrm{d}y\, \mathrm{d}z, \tag{3.7}$$

where $\Delta x_i = x_{i+1/2} - x_{i-1/2}$, $\Delta y_j = y_{j+1/2} - y_{j-1/2}$, $\Delta z_k = z_{k+1/2} - z_{k-1/2}$, and $V_{i,j,k} = \Delta x_i \Delta y_j \Delta z_k$. Only the form of one flux vector is provided, as the forms of the remaining ones are analogous. Equation (3.4) is the end result of the spatial discretization of Equation (3.1). It remains, however, an exact relationship and must now be numerically approximated.

We proceed by first numerically approximating the right-hand side (RHS) of Equation (3.4). To do so, the surface integrals of the fluxes, *e.g.* Equation (3.6), and the volume integral of the source term, Equation (3.7), need to be estimated. Titarev and Toro [110] suggest utilizing a two-point, fourth-order, Gaussian quadrature rule, as it offers a good balance between accuracy and computational cost when paired with a high-order WENO spatial reconstruction scheme. Then, applying the two-point Gaussian quadrature rule to Equation (3.6), we get

$$\mathbf{f}^{\mathrm{a}}_{i+1/2,j,k} \approx \frac{1}{4} \sum_{m=1}^{2} \sum_{l=1}^{2} \mathbf{f}^{\mathrm{a}}\left(\mathbf{q}\left(x_{i+1/2}, y_{j_l}, z_{k_m}, t\right)\right), \tag{3.8}$$

where y_{j_l} and z_{k_m} are the y- and z-coordinates of the Gaussian quadrature points and are given by

$$y_{j_l} = y_j + (2l - 3)\frac{\Delta y_j}{2\sqrt{3}} \quad \text{and} \quad z_{k_m} = z_k + (2m - 3)\frac{\Delta z_k}{2\sqrt{3}}, \tag{3.9}$$

with the indices j_l and k_m defined as

$$j_l = j + (2l - 3)\frac{1}{2\sqrt{3}} \quad \text{and} \quad k_m = k + (2m - 3)\frac{1}{2\sqrt{3}}. \tag{3.10}$$

The surface integrals of the remaining fluxes are treated analogously. Next, we seek to apply the two-point Gaussian quadrature rule to the volume integral of the source term. In doing so, however, we must ensure that the velocity utilized in the numerical integration of the source term is consistent with that utilized in the numerical integration of the fluxes. To satisfy this requirement for the source term of the advection equation, we follow the work of Johnsen and Colonius [64] in approximating its volume integral with a midpoint rule and the divergence of the velocity therein with a centered scheme. As a result, we get

$$\begin{aligned}(\alpha_1 \nabla \cdot \mathbf{u})_{i,j,k} \approx \alpha_{1_{i,j,k}} \bigg[& \frac{1}{\Delta x_i}\left(u_{i+1/2,j,k} - u_{i-1/2,j,k}\right) \\ & + \frac{1}{\Delta y_j}\left(v_{i,j+1/2,k} - v_{i,j-1/2,k}\right) \\ & + \frac{1}{\Delta z_k}\left(w_{i,j,k+1/2} - w_{i,j,k-1/2}\right) \bigg],\end{aligned} \tag{3.11}$$

which utilizes the same velocity as Equation (3.4) to evaluate the fluxes. Though Equation (3.11) is formally only second-order accurate, the error is zero everywhere except near material interfaces, which are not resolvable beyond first-order accuracy in any case. The above simplification now requires us to numerically integrate the source term as a surface integral, rather than a volume one. Specifically, we must now apply the two-point Gaussian quadrature rule to the surface integrals of the velocity components in Equation (3.11). In doing so, we get

$$u_{i+1/2,j,k} \approx \frac{1}{4} \sum_{m=1}^{2} \sum_{l=1}^{2} u \left(\mathbf{q} \left(x_{i+1/2}, y_{j_l}, z_{k_m}, t \right) \right) , \tag{3.12}$$

with the remaining velocity components treated analogously.

The last step to finalizing the numerical approximation of the RHS of Equation (3.4) is to reconstruct the state variables at the Gaussian quadrature points on every cell face in order to be able to evaluate the quadrature rule for all of the fluxes, *e.g.* Equation (3.8), and the velocity components in the source term, *e.g.* Equation (3.12). To obtain high-order accuracy spatially and avoid introducing spurious oscillations, we utilize a fifth-order WENO scheme to reconstruct the state variables from both the left and the right side of each cell face. An appropriate monotone function of the dual values of the state variables is then utilized to evaluate the fluxes, *e.g.*

$$\mathbf{f}^{\mathrm{a}}_{i+1/2,j,k} \approx \frac{1}{4} \sum_{m=1}^{2} \sum_{l=1}^{2} \hat{\mathbf{f}}^{\mathrm{a}} \left(\mathbf{q}^{\mathrm{L}}_{i+1/2,j_l,k_m}, \mathbf{q}^{\mathrm{R}}_{i+1/2,j_l,k_m} \right) , \tag{3.13}$$

and the velocity components in the source term, *e.g.*

$$u_{i+1/2,j,k} \approx \frac{1}{4} \sum_{m=1}^{2} \sum_{l=1}^{2} \hat{u} \left(\mathbf{q}^{\mathrm{L}}_{i+1/2,j_l,k_m}, \mathbf{q}^{\mathrm{R}}_{i+1/2,j_l,k_m} \right) , \tag{3.14}$$

where “L” and “R” denote the state variables reconstructed from the left and the right side of a cell face, respectively, and the hat superscript indicates the monotone function counterpart of the superscripted variable. The choice of a monotone function enables us to compute a singular value of the fluxes at each cell face and achieve the familiar telescoping property of the fluxes [76, 111], which guarantees that the numerical method is discretely conservative. Further details on the WENO reconstruction may be found in Appendix C, while those on the choice of a monotone function are provided in the overview of the HLLC approximate Riemann solver, in Appendix D.

3.3 Reconstructed variables

The choice of the reconstructed state variables is not unique and in practice, it is preferable not to reconstruct the conservative variables as this will introduce spurious oscillations near material interfaces, as well as in regions where discontinuities of different characteristic fields interact [54, 92]. In order to avoid introducing spurious oscillations near material interfaces, Johnsen and Colonius [64] showed that the primitive variables should be reconstructed. They further demonstrated that by projecting the primitive variables onto the characteristic fields prior to the reconstruction and thus reconstructing the characteristic variables, the introduction of spurious oscillations in regions where discontinuities of different characteristic fields interact could also be avoided.

Recall, however, that at the beginning of each time-step, only the cell average conservative variables are available. To remedy this, Johnsen and Colonius [64] suggest obtaining a second-order estimate of the cell average primitive variables by directly computing them from the conservative ones. They argue that a WENO interpolation of this second-order approximation will nevertheless result in a high-order reconstruction. But, as we illustrate in Section 3.6.4, this is in general not the case and in fact, usually reduces the formal order of the spatial accuracy of the numerical method to second-order. We recover a high-order scheme by discretizing the volume integral of the primitive variables, $\mathbf{v}$, *i.e.*

$$\mathbf{v}_{i,j,k} = \frac{1}{V_{i,j,k}} \int_{z_{k-1/2}}^{z_{k+1/2}} \int_{y_{j-1/2}}^{y_{j+1/2}} \int_{x_{i-1/2}}^{x_{i+1/2}} \mathbf{v}\left(\mathbf{q}\left(x,y,z,t\right)\right)\ \mathrm{d}x\ \mathrm{d}y\ \mathrm{d}z, \tag{3.15}$$

with the two-point Gaussian quadrature rule to get a fourth-order accurate estimate of the cell average primitive variables:

$$\mathbf{v}_{i,j,k} \approx \frac{1}{8} \sum_{n=1}^{2} \sum_{m=1}^{2} \sum_{l=1}^{2} \mathbf{v}\left(\mathbf{q}\left(x_{i_l}, y_{j_m}, z_{k_n}, t\right)\right), \tag{3.16}$$

where $\mathbf{v}$ is defined in Appendix B. Then, at the beginning of each time-step, in order to obtain the cell average primitive variables, the cell average conservative variables must first be reconstructed at the

Gaussian quadrature points in the cell volume. The cell average primitive variables may subsequently be projected onto the characteristic fields by following the procedure outlined in Appendix B.

In addition to the characteristic variables, the cell average of the gradient of the velocity must also be reconstructed at the Gaussian quadrature points of both the left and right side of each cell face. This is necessary in order to evaluate the viscous terms in the diffusive fluxes. We evaluate the cell average of the gradient of the velocity by applying the divergence theorem to the volume integral of each of its terms in order to obtain the following surface integral:

$$\nabla \mathbf{u}_{i,j,k} = \frac{1}{V_{i,j,k}} \int_{V_{i,j,k}} \nabla \mathbf{u} \; \mathrm{d}V = \frac{1}{V_{i,j,k}} \int_{\partial V_{i,j,k}} \mathbf{nu} \; \mathrm{d}A, \tag{3.17}$$

which may then be evaluated to obtain, for example, the first column vector of $\nabla \mathbf{u}_{i,j,k}$:

$$\frac{\partial \mathbf{u}_{i,j,k}}{\partial x} = \frac{\mathbf{u}_{i+1/2,j,k} - \mathbf{u}_{i-1/2,j,k}}{\Delta x_i}, \tag{3.18}$$

with the remaining column vectors, those for the spatial derivatives of the cell average velocity in the y- and z-direction, taking a similar form. Note from Equation (3.18) that in order to obtain all of the elements of $\nabla \mathbf{u}_{i,j,k}$ and reconstruct them at the cell faces, the average velocity at the cell faces must first be computed. In Appendix E, we outline all of the variables that must be reconstructed and the order in which their reconstruction must be carried out.

3.4 Temporal integration

To complete the design of the numerical method, the semi-discrete approximation of the equations of motion must now be temporally integrated. Since the latter is a system of ordinary differential equations, we choose a RK time-marching scheme to evolve the state variables in time. In particular, to achieve high-order accuracy temporally and avoid introducing spurious oscillations, we follow Johnsen and Colonius [64] and Titarev and Toro [110] in choosing the low-storage, third-order, TVD RK time-marching scheme of Gottlieb and Shu [51]:

$$\left.\begin{aligned}
\mathbf{q}^{(1)}_{i,j,k} &= \mathbf{q}^{n}_{i,j,k} + \Delta t \mathbf{L}\left(\mathbf{q}^{n}_{i,j,k}\right), \\
\mathbf{q}^{(2)}_{i,j,k} &= \frac{3}{4}\mathbf{q}^{n}_{i,j,k} + \frac{1}{4}\mathbf{q}^{(1)}_{i,j,k} + \frac{1}{4}\Delta t \mathbf{L}\left(\mathbf{q}^{(1)}_{i,j,k}\right), \\
\mathbf{q}^{n+1}_{i,j,k} &= \frac{1}{3}\mathbf{q}^{n}_{i,j,k} + \frac{2}{3}\mathbf{q}^{(2)}_{i,j,k} + \frac{2}{3}\Delta t \mathbf{L}\left(\mathbf{q}^{(2)}_{i,j,k}\right),
\end{aligned}\right\} \tag{3.19}$$

where Δt is the time-step size, $\mathbf{L}$ is the operator evaluating the numerically approximated RHS of Equation (3.4), the superscripts (1) and (2) denote the intermediate time-stages between two consecutive time-steps, and the superscripts n and $n+1$ denote the current and the subsequent time-steps, respectively. With the choice of time-stepper made, the design of the numerical scheme is now complete and satisfies the desired criteria previously outlined, *i.e.* it is high-order accurate, discretely conservative and non-oscillatory.

3.5 Stability

The stability of the numerical scheme is dictated by the Courant-Friedrichs-Lewy (CFL) number, C, and the diffusion number, D. Unfortunately, as a result of the nonlinear behavior of both the equations of motion and the WENO reconstruction, the stability bounds of either criterion are not readily obtainable by analytic methods. Though these bounds could be determined through extensive numerical experimentation, in practice, it is more convenient to guide the choice of a stable time-step by relying on the readily available stability results for a forward in time, centered in space, numerical scheme applied to the linear advection-diffusion equation. Then, based on the latter, a stable time-step for a given simulation is chosen by ensuring that throughout the duration of the simulation the time-step satisfies

$$\Delta t = C \cdot \min_{i,j,k}\left(\frac{\Delta x_i}{|u_{i,j,k}| + c_{i,j,k}}, \frac{\Delta y_j}{|v_{i,j,k}| + c_{i,j,k}}, \frac{\Delta z_k}{|w_{i,j,k}| + c_{i,j,k}}\right), \quad 0 < C \leq \frac{1}{3}, \tag{3.20}$$

for the CFL number, as well as

$$\Delta t = D \cdot \min_{i,j,k} \left(\frac{\Delta x_i^2}{\nu_{i,j,k}}, \frac{\Delta y_j^2}{\nu_{i,j,k}}, \frac{\Delta z_k^2}{\nu_{i,j,k}} \right), \quad 0 < D \leq \frac{1}{6}, \tag{3.21}$$

for the diffusion number, where $\nu = \mu/\rho$ is the kinematic viscosity [48, 110]. The strong time-step restriction imposed by the diffusion number can be removed by an implicit treatment of the viscous terms, by utilizing a semi-implicit RK method for example [70], as done in [43]. For simulations in less than three dimensions, Equations (3.20) and (3.21) must be simplified accordingly, while the stability bounds for both the CFL number and the diffusion number may be relaxed. In N dimensions, the latter are given by

$$0 < C \leq \frac{1}{N}, \quad 0 < D \leq \frac{1}{2N}, \tag{3.22}$$

see [48] for details. Finally, since a linear stability is being utilized for a nonlinear problem, the largest time-step allowed by Equations (3.20)–(3.22) is in all likelihood not a conservative upper limit. In general, to achieve stability, the need for a smaller time-step than that predicted by the above strategy should be expected.

Of course, since the numerical scheme is not TVD due to the WENO reconstruction, even for a forbiddingly small choice of time-step, stability cannot be guaranteed in the long-term when evolving a general initial condition. This issue is particularly relevant to the simulation of flows featuring the interaction of shockwaves and material interfaces with high pressure and density ratios, respectively. In such cases, WENO may not be able to find a smooth stencil during reconstruction and may interpolate values for a variable that a) are outside its physical range, b) will be outside its physical range once it is updated and/or c) will result in other variables, which are computed from the one that is reconstructed, to lay outside their physical range. In the worst-case scenario, a simulation may have to be abruptly terminated. In our experience, this is typically the case when an unphysical sound speed is recovered.

Some authors have proposed partly alleviating this problem by either reducing the order of the reconstruction [110] or utilizing flux limiters [53, 100, 113] in the affected regions of the flow . This, however, may lead to excessive smearing of material interfaces as they evolve or, in the case that an interface-sharpening technique is employed as a remedy, a loss of discrete conservation [100]. While it is true that discretely conservative interface-sharpening techniques do exist for diffuse interface methods [106], their robustness remains to be rigorously documented when applied to material interfaces with high density ratios and which are interacting with strong shockwaves.

To maintain the desired properties of our numerical scheme, we do not utilize any of the above methods. Instead, when necessary, we primarily increase stability by initially smearing material interfaces over a few cells, as well as reducing the number of WENO reconstructions per time-step near them. The latter is achieved by omitting all of the reconstructions at the Gaussian quadrature points. This neither affects the formal order of accuracy near material interfaces, nor, in our experience, negatively impacts their smearing. We also utilize monotonicity-preserving bounds for WENO near material interfaces to prevent the reconstruction of a variable outside its physical range [8]. Finally, for viscous simulations, we limit the coefficient of shear viscosity in mixture regions to the range established by the components composing the mixture in order to avoid the onset of anti-diffusion.

Though the above-proposed strategies are sufficient to maintain numerical stability in the challenging test cases considered in this study, it is difficult to predict *a priori* whether they will be adequate for an arbitrarily chosen initial condition since the numerical scheme remains non-TVD. In the case that they are not, reducing the order of the reconstruction or using flux limiters, as in [53, 100, 110, 113], may be inevitable to increase stability, in spite of the additional smearing of material interfaces. If necessary, these strategies can be implemented at relatively low computational cost and effort in the present numerical scheme.

3.6 Verification

In the sections that follow, we present 1D, 2D and 3D test cases to validate and verify our numerical scheme. Specifically, we show that the present algorithm is high-order accurate in smooth regions of the flow, discretely conserves the mass of each component, along with the total momentum and energy, and does not generate spurious oscillations. Also unless it is specified otherwise, the properties of the fluids utilized in each test case may be found in Table 2.1.

3.6.1 Isolated interface advection

The onset of spurious oscillations at material interfaces can have a detrimental impact on both the quality and reliability of computed solutions. It can result in the pollution of fine flow features [67], the premature growth of physical instabilities [64], and the thickening of material interfaces [69]. Worse, it may even result in the computation of the wrong solution [2] or the fatal termination of the computation [69]. Of course, the severity of these problems will depend on the initial condition [1]. To illustrate some of these issues for a numerical scheme plagued by spurious oscillations and to confirm that the proposed numerical scheme does not experience them, we consider an initial condition relevant to many multicomponent flow computations – the advection of an isolated air/water interface.

In particular, we consider an air/water interface under atmospheric pressure, advected in a periodic domain and at a constant velocity. The initial condition for this problem, nondimensionalized by the density and sound speed of water, is given by

$$(\alpha_1\rho_1, \alpha_2\rho_2, u, p, \alpha_1) = \begin{cases} (1.204\times10^{-3}, 0, 0.01, 4.819\times10^{-5}, 1) & \text{for} \quad -1 \le x < 0, \\ (0, 1, 0.01, 4.819\times10^{-5}, 0) & \text{for} \quad 0 \le x < 1. \end{cases} \tag{3.23}$$

It is evolved with a constant time-step, $\Delta t = 5\times10^{-3}$, on a uniform grid composed of 200 cells, for exactly one period, *i.e.* until the material interface has returned to its original position. Three different methods are utilized to compute the numerical solution. In the first, the conservative variables, instead of the primitive variables, are reconstructed at the cell boundaries in order to demonstrate how the onset of spurious oscillations at the material interface corrupts the numerical solution. In the second, following Johnsen and Colonius [64], the primitive variables are reconstructed from their second-order accurate cell averages in order to recover an oscillation-free material interface. Finally,

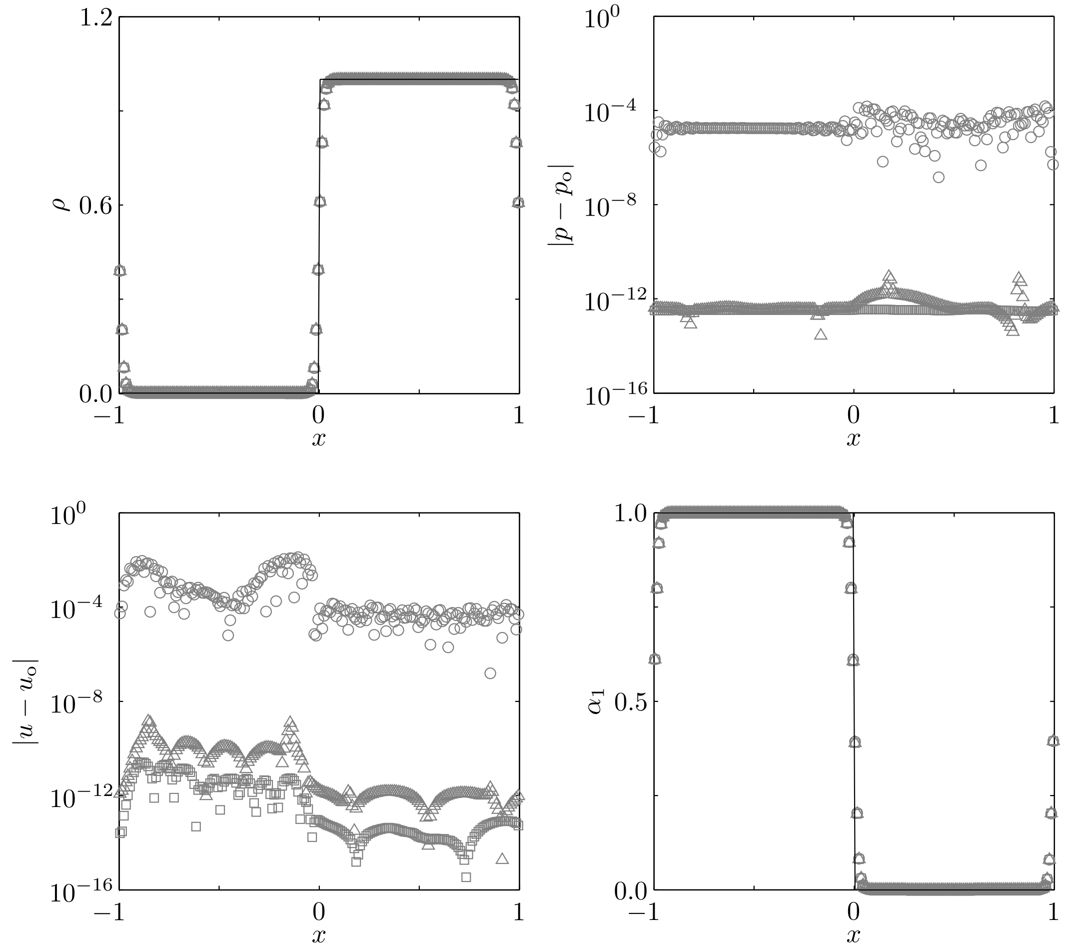

Figure 3.1: Plots of density, magnitude of the error in velocity and pressure, and volume fraction for the isolated interface advection problem given by Equation (3.23). The exact solution (—), along with three numerical solutions distinguished by the type and order of accuracy of the cell average variables that are reconstructed at the cell boundaries, are compared at $t = 200$. The latter include the conservative variables (○), the second-order accurate primitive variables (□), following Johnsen and Colonius [64], and the fourth-order accurate primitive variables (△), following the present numerical scheme.

the initial condition is also evolved with the present numerical scheme, where the primitive variables are reconstructed from their fourth-order accurate cell averages, to confirm that the oscillation-free character of the material interface, recovered by the previous method, is conserved.

In Figure 3.1, we compare the results obtained by all three methods, both to each other, as well as to the exact solution. We include the plots for density, velocity, pressure, and volume fraction. In order to be able to visualize the spurious oscillations in velocity and pressure for all three methods, on the same plots, the absolute value of the difference between the approximate and exact solutions is plotted for these quantities, instead of the quantities themselves. The results in Figure 3.1 are as expected. When the conservative variables are reconstructed, spurious oscillations are generated at the material interface. For the chosen initial condition, these are unacceptably large, at times matching, and even surpassing, the order of magnitude of the uniform velocity and pressure. As a result, though not shown, the pressure computed by this method often becomes negative, which is supported by the stiffened gas EOS, but is bound to mispredict a change in phase, if the latter physics were to be included. Nevertheless, the plots of density and volume fraction indicate that the position of the material interface, as well as the jump in these quantities across it, are correctly computed.

When the primitive variables are reconstructed from their second-order accurate cell averages, on the other hand, the spurious oscillations are reduced to the order of the round-off error. In the current case, for both the velocity and pressure, this corresponds to $\mathcal{O}(10^{-12})$, which is well below the order of magnitude of the corresponding uniform values. Reconstructing the primitive variables from their fourth-order accurate cell averages only marginally compromises this result, suggesting that the present numerical scheme conserves the oscillation-free character at material interfaces. Though not shown, comparable results were also obtained for other initial conditions. Finally, in both cases, the correct density and volume fraction profiles are also computed.

3.6.2 Shock-interface interaction

As previously indicated, the interaction between a shockwave and a material interface is a challenging problem for numerical schemes that have sacrificed discrete conservation at the material interface to either sharpen it or to avoid spurious oscillations. Most commonly, such methods will miscalculate the position and speed of the waves resulting from the interaction, with the error becoming increasingly worse with an increasing loss in conservation. To study the behavior of our numerical scheme when applied to such problems, we consider here the interaction between a strong shockwave in helium and an air/helium interface.

The original problem was studied by Liu *et al.* [77] and later, in modified form, by Johnsen [63].

As given by the latter, the problem consists of a Mach 8.96 shockwave traveling in helium toward a material interface with air, which is simultaneously moving toward the shockwave. Both the unprocessed helium and the air are at atmospheric pressure. The initial condition for this problem, utilizing the fluid properties and nondimensionalization as in [63], is given by

$$(\alpha_1\rho_1, \alpha_2\rho_2, u, p, \alpha_1) = \begin{cases} (0.386, 0, 26.59, 100, 1) & \text{for} \quad -1 \leq x < -0.8, \\ (0.1, 0, -0.5, 1, 1) & \text{for} \quad -0.8 \leq x < -0.2, \\ (0, 1, -0.5, 1, 0) & \text{for} \quad -0.2 \leq x \leq 1. \end{cases} \tag{3.24}$$

The solution is evolved with a constant time-step, $\Delta t = 10^{-4}$, on a uniform grid composed of 200 cells, and consists of the original shockwave partly transmitted into the air and partly reflected back into the helium.

In Figure 3.2, the exact and numerical solutions for the density, velocity, pressure, and volume fraction are given at $t = 0.07$. The numerical solution compares well to the exact one, correctly identifying the position and speed of all of the waves in the problem. Once again, no spurious oscillations at the material interface are observed. However, some oscillations in the wake of the reflected shockwave are present. These are a consequence of the high-order accuracy of the spatial reconstruction and, though not shown, disappear as the latter is reduced.

3.6.3 Gas-liquid Riemann problem

The last 1D test case that we consider is a gas-liquid Riemann problem originally studied by Cocchi *et al.* [30], and subsequently by Shyue [101], as a model for underwater explosions. It is a challenging shock tube problem and provides an excellent test of the stiffened gas EOS. The left state of the problem consists of compressed air, while the right state is water at atmospheric pressure. The initial condition for this problem, utilizing the fluid properties and nondimensionalization as in [30],

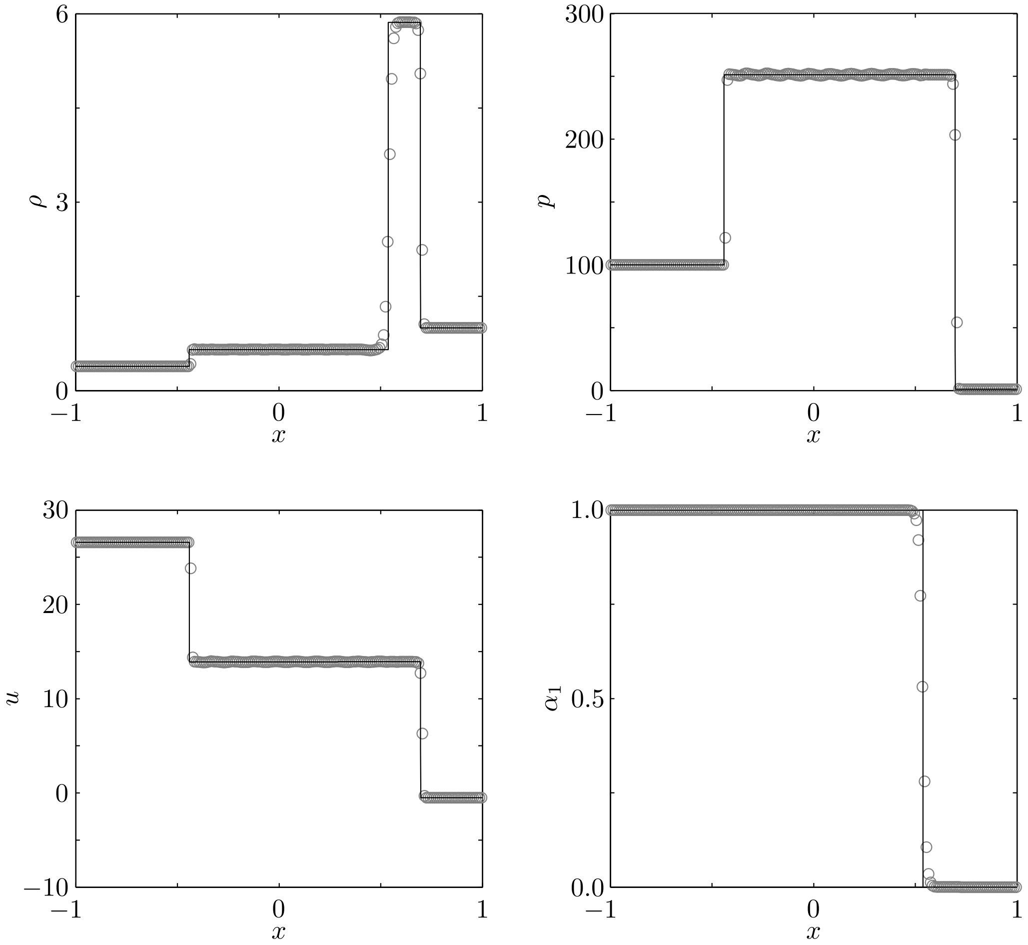

Figure 3.2: Plots of density, velocity, pressure, and volume fraction for the shock-interface interaction problem given by Equation (3.24). The exact (—) and numerical (○) solutions are compared at $t = 0.07$.

is given by

$$(\alpha_1\rho_1, \alpha_2\rho_2, u, p, \alpha_1) = \begin{cases} (1.241, 0, 0, 2.753, 1) & \text{for} \quad -1 \leq x < 0, \\ (0, 0.991, 0, 3.059 \times 10^{-4}, 0) & \text{for} \quad 0 \leq x \leq 1. \end{cases} \tag{3.25}$$

It is evolved with a constant time-step, $\Delta t = 10^{-3}$, on a uniform grid composed of 200 cells, and consists of a left-moving rarefaction wave and a right-moving shockwave and material interface.

In Figure 3.3, the exact and numerical solutions for the density, velocity, pressure, and volume fraction are given at $t = 0.2$. As in the previous test cases, the numerical solution compares well to the exact one and correctly identifies the position and speed of all of the waves in the problem.

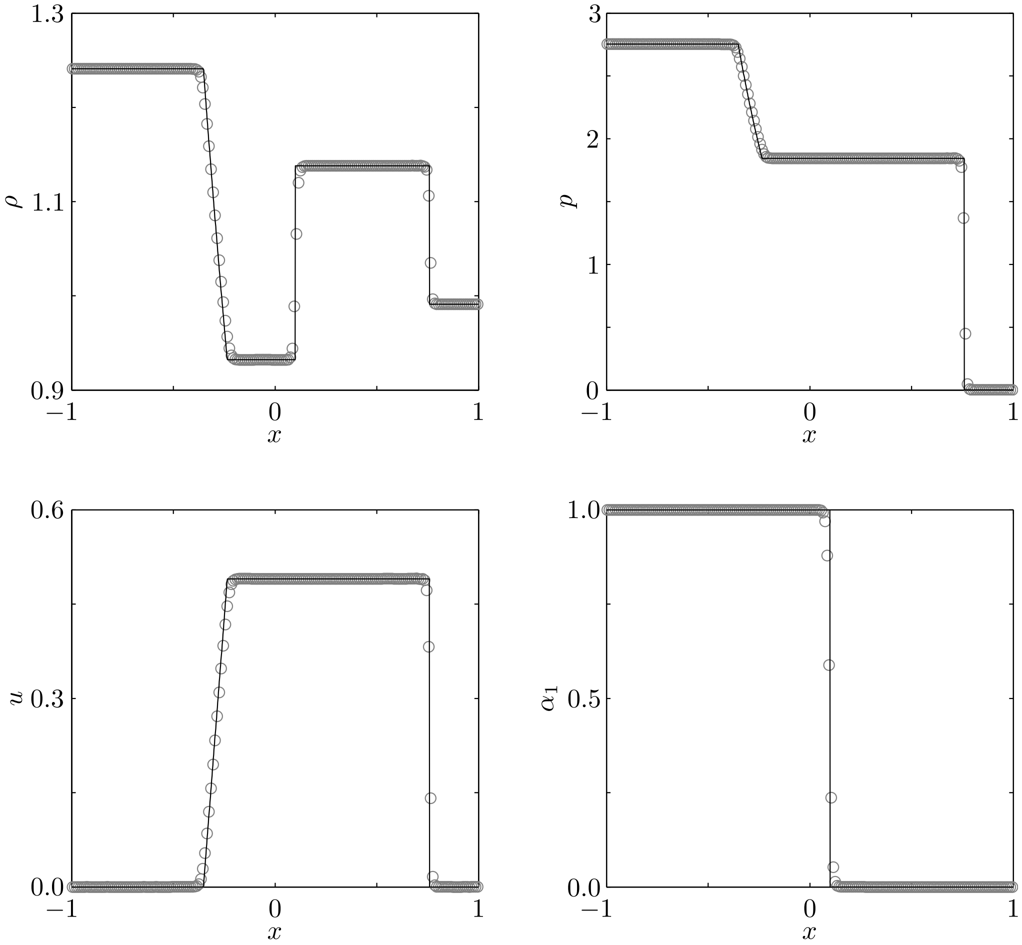

Figure 3.3: Plots of density, velocity, pressure, and volume fraction for the gas-liquid Riemann problem given by Equation (3.25). The exact (—) and numerical (○) solutions are compared at $t = 0.2$.

Moreover, there are no visible oscillations at the material interface or elsewhere in the solution.

3.6.4 Isentropic vortex

We consider next a 2D problem governed by the Euler equations for which an analytical solution is readily available – the evolution of an isentropic vortex. The problem was studied by Balsara and Shu [8] and subsequently by Titarev and Toro [110] in order to assess the convergence properties of increasingly higher-order accurate WENO schemes for smooth solutions to the Euler equations. Similarly, we study this problem here to verify that the present numerical scheme achieves high-order accuracy away from shockwaves and material interfaces and also to demonstrate that the original method of Johnsen and Colonius [64] fails to do the same.

The isentropic vortex is a perturbation superimposed on the mean flow of an ideal gas and its initial condition may compactly be written in terms of the perturbed velocities, u' and v', and temperature, T':

$$\left.\begin{aligned} u' &= \frac{\epsilon}{2\pi}\exp\left[\alpha\left(1-r^2\right)\right]y, \\ v' &= -\frac{\epsilon}{2\pi}\exp\left[\alpha\left(1-r^2\right)\right]x, \\ T' &= -\frac{(\gamma-1)}{16\alpha\gamma\pi^2}\exp\left[2\alpha\left(1-r^2\right)\right], \end{aligned}\right\} \tag{3.26}$$

where ϵ is the strength of the vortex, α is its decay rate, $r^2 = x^2+y^2$ and the usual primitive variables may be obtained from the ideal gas law, $p = \rho T$, and the isentropic relationship $p = \rho^\gamma$. It is typical to superimpose the vortex on a nonzero, but uniform, velocity field of air and to evolve the resulting initial condition on a domain with periodic boundary conditions. However, without any loss in the generality of the convergence study, we choose here quiescent air instead, $(u, v, T) = (0, 0, 1)$, as well as extrapolation boundary conditions, in order to facilitate the extension of the study to nonuniform grids. We evolve the initial condition on a square domain, $x, y \in [-5, 5]$, and choose the strength, $\epsilon = 5$, and decay rate, $\alpha = 1$, of the vortex such that it has compact support in this region. A fixed CFL number, $C = 0.3$, is selected for the convergence study and a fifth-order RK time-stepping scheme, with the coefficients of Cash and Karp [16], is provisionally utilized instead of the third-order TVD RK method to ensure that the order of accuracy of the temporal discretization does not mask that of the spatial discretization. The nonuniform grids are generated by a continuously differentiable hyperbolic tangent function and are stretched at the domain boundaries. In Figure 3.4, the cell size distribution for the coarsest grid, 25×25 cells, is shown in the plot on the left. The numerical solution is computed on grid sizes up to 400×400 cells with an output time of $t = 1$. Since the isentropic vortex is stationary, the exact solution at the given output time is simply the initial condition to the problem and any discrepancy between the exact and numerical solutions is due to numerical diffusion.

The convergence study is performed on the density, for which the initial condition is shown in the left plot of Figure 3.4. In the right plot of the same figure, the results of the study are pre-

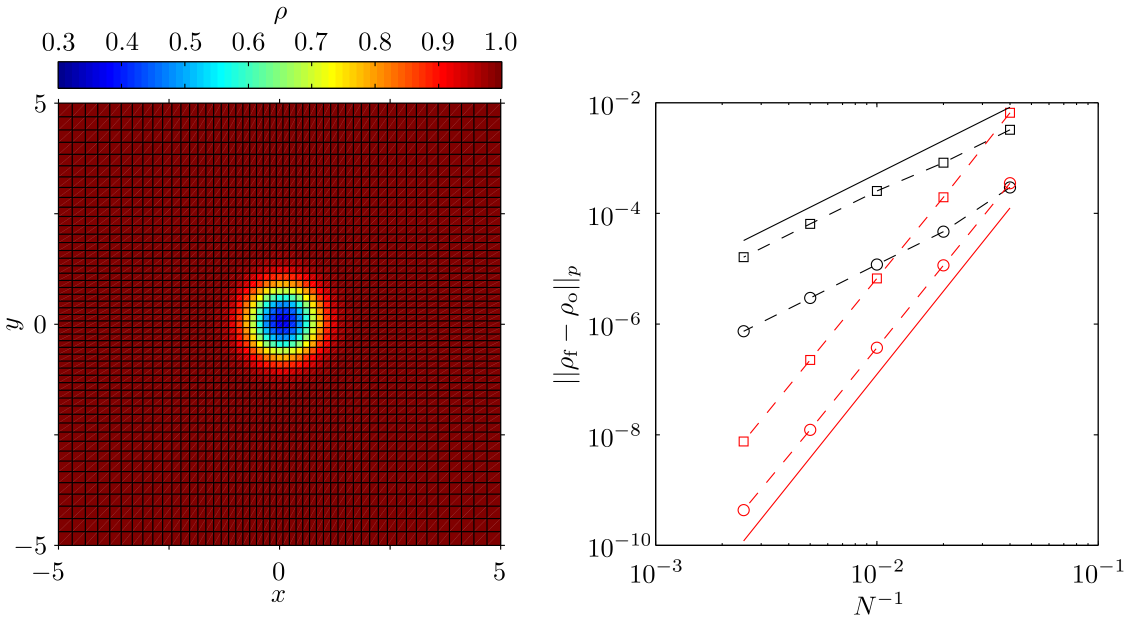

Figure 3.4: Plots of the density at $t = 0$, ρ_{o}, on the coarsest nonuniform grid, 25×25 cells (left), and p-norm of the error between the density at $t = 0$ and $t = 1$, ρ_{f}, as a function of the grid size, $N \times N$ (right), for the stationary isentropic vortex problem given by Equation (3.26). The grid convergence of the L_1- and L_∞-norm is shown for both when the primitive variables are reconstructed at the cell boundaries from their second-order accurate cell averages (–○– and –□–, respectively), following Johnsen and Colonius [64], and their fourth-order accurate cell averages (–○– and –□–, respectively), following the present scheme. Reference slopes for the second-order (—) and fifth-order (—) convergence rates are also included.

sented. These include the L_1- and L_∞-norms of the error in density as a function of the grid size for both the present numerical scheme and that of Johnsen and Colonius [64]. The reference slopes for both the second- and fifth-order convergence rates are also included. The results indicate that reconstructing the primitive variables at the cell boundaries from their second-order accurate cell averages, contrary to the conclusions of Johnsen and Colonius, does not lead to a high-order accurate numerical scheme. Instead, the resulting method is second-order accurate at best, as indicated by the second-order convergence rate of the corresponding L_1- and L_∞-norms. On the other hand, the results show that the present numerical scheme, by reconstructing the primitive variables at the cell boundaries from their fourth-order accurate cell averages, recovers high-order accuracy. In this case, the corresponding L_1- and L_∞-norms achieve a fifth-order convergence rate. This is higher than the optimal fourth-order convergence rate that is expected as a result of utilizing a two-point Gaussian quadrature rule. It agrees, however, with the results of the analogous convergence study by Titarev

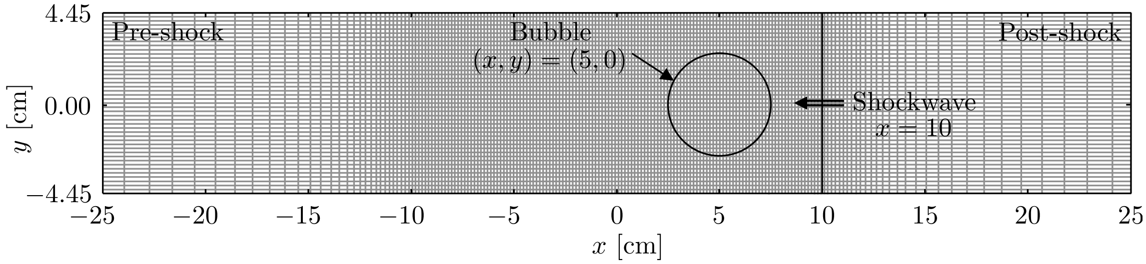

Figure 3.5: Schematic of the initial condition and the computational grid (only one of every 40 cells shown) for the shock-bubble interaction problem. As a result of the symmetry of the initial condition, only the top half of the displayed computational grid is utilized in the simulation.

and Toro [110], who also observed superconvergence.

Finally, though its parameters and results are not detailed here, we have also performed a convergence study on the typical isentropic vortex problem, *i.e.* where the vortex is superimposed on a nonzero, but uniform, air flow, $(u, v, T) = (1, 1, 1)$, and evolved on a domain with periodic boundary conditions. Uniform grids, with a range of sizes comparable to those used before, were utilized to study the convergence properties of only the present numerical scheme, with the third-order TVD RK time-stepping method. A little better than fourth-order convergence was achieved in both the L_1- and L_∞-norms, despite the third-order accuracy of the temporal discretization. This superconvergence is consistent with the results of Titarev and Toro [110].

3.6.5 Shock-bubble interaction

We consider next the 2D interaction between a helium bubble and a weak shockwave in air. The problem was experimentally studied by Haas and Sturtevant [52] and subsequently often utilized as a validation case for multicomponent flow algorithms, see [39, 55, 59, 64, 79, 82, 93, 100, 106, 107] to name a few. It consists of a 5 cm in diameter bubble, which is vertically centered inside a shock tube and filled with helium. The helium in the bubble is not pure, but contaminated by the surrounding air, 28% by mass concentration. The bubble is impacted by a Mach 1.22 shockwave traveling in air at atmospheric pressure. A schematic of the initial condition for this problem is shown in Figure 3.5 and the corresponding state variables are given by

$$(\alpha_1\rho_1, \alpha_2\rho_2, u, v, p, \alpha_1) = \begin{cases} (0, 1.204, 0, 0, 101325, 0) & \text{for} \quad \text{Pre-shock}, \\ (0, 1.658, -114.49, 0, 159060, 0) & \text{for} \quad \text{Post-shock}, \\ (0.158, 0.061, 0, 0, 101325, 0.95) & \text{for} \quad \text{Bubble}, \end{cases} \tag{3.27}$$

where the densities, velocities and pressures are in kg/m^3, m/s and Pa, respectively.

As illustrated in Figure 3.5, we utilize a 6000×890 nonuniform computational grid to evolve the initial condition. A RBC is used along both the top of the grid, to model the shock tube wall, and along its lengthwise centerline, to model the symmetry of the problem for computational efficiency. Inflow and outflow boundary conditions are implemented on the right and left of the grid, respectively, and are smoothly stretched away from the shock-bubble interaction region to prevent any reflections off of these boundaries from polluting the solution. The grid in the shock-bubble interaction region, $x \in [-10, 10]$ cm, on the other hand, is uniform with $\Delta x = \Delta y = 50$ μm. The solution is evolved at a fixed CFL number, $C = 0.4$, and until $t = 983$ μs. The latter is measured from the moment the shockwave impacts the bubble and is the last time at which Haas and Sturtevant [52] report shadowgraph images from the experiment.

In Figure 3.6, as a qualitative form of validation of our numerical scheme, we compare the numerical Schlieren images of the shock-bubble interaction to the shadowgraphs of Haas and Sturtevant [52] at approximately the same times. The images depict the configuration of the waves resulting from the shock-bubble interaction, as well as the eventual involution of the bubble to form a jet and subsequently a vortex ring. The results of the simulation compare well to those of the experiment. There are no visible spurious oscillations in the numerical Schlieren images, despite the fact that they accentuate small fluctuations in density. A common startup error, however, is generated by the shockwave and appears as a weak vertical line near the upstream interface of the bubble in nearly every Schlieren [4]. Fortunately, since it is nearly stationary and outside the region where the shockwave and bubble interact, it has no adverse dynamic effect on the numerical solution.

We validate our numerical scheme quantitatively by comparing the experimental velocity measurements of key flow features, as obtained by Haas and Sturtevant [52], to those obtained in the

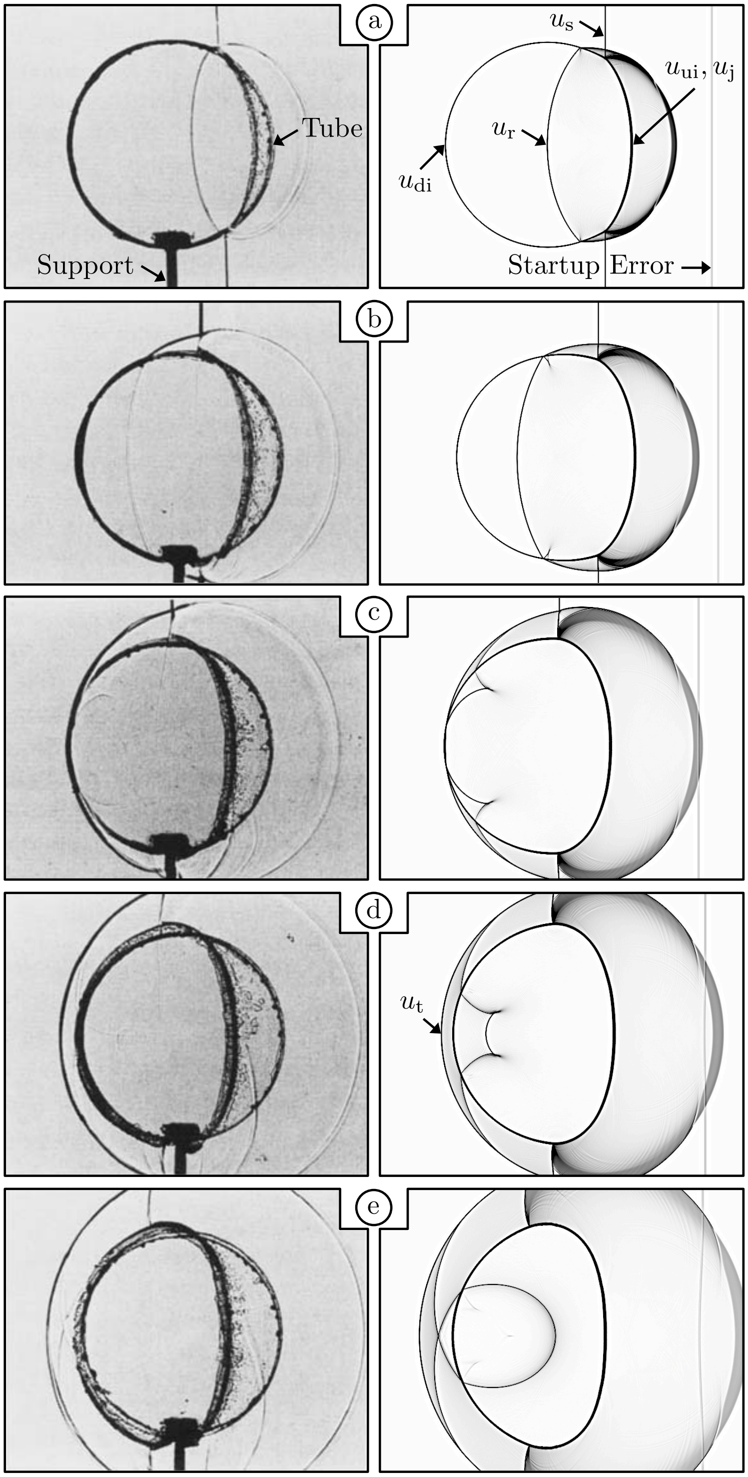

Figure 3.6: Comparison between the experimental shadowgraphs of Haas and Sturtevant [52] (left) and numerical Schlieren images from simulation (right) for the shock-bubble interaction problem. The numerical Schlieren imaging technique is adapted from [93]. Temporal snapshots are included at a) 26 (32), b) 37 (52), c) 52 (62), d) 62 (72) and e) 80 (82) μs, where the shadowgraph time stamps are given in parentheses when different from those of numerical Schlieren images. Experimental images ©Cambridge University Press 1987. Reprinted with permission.

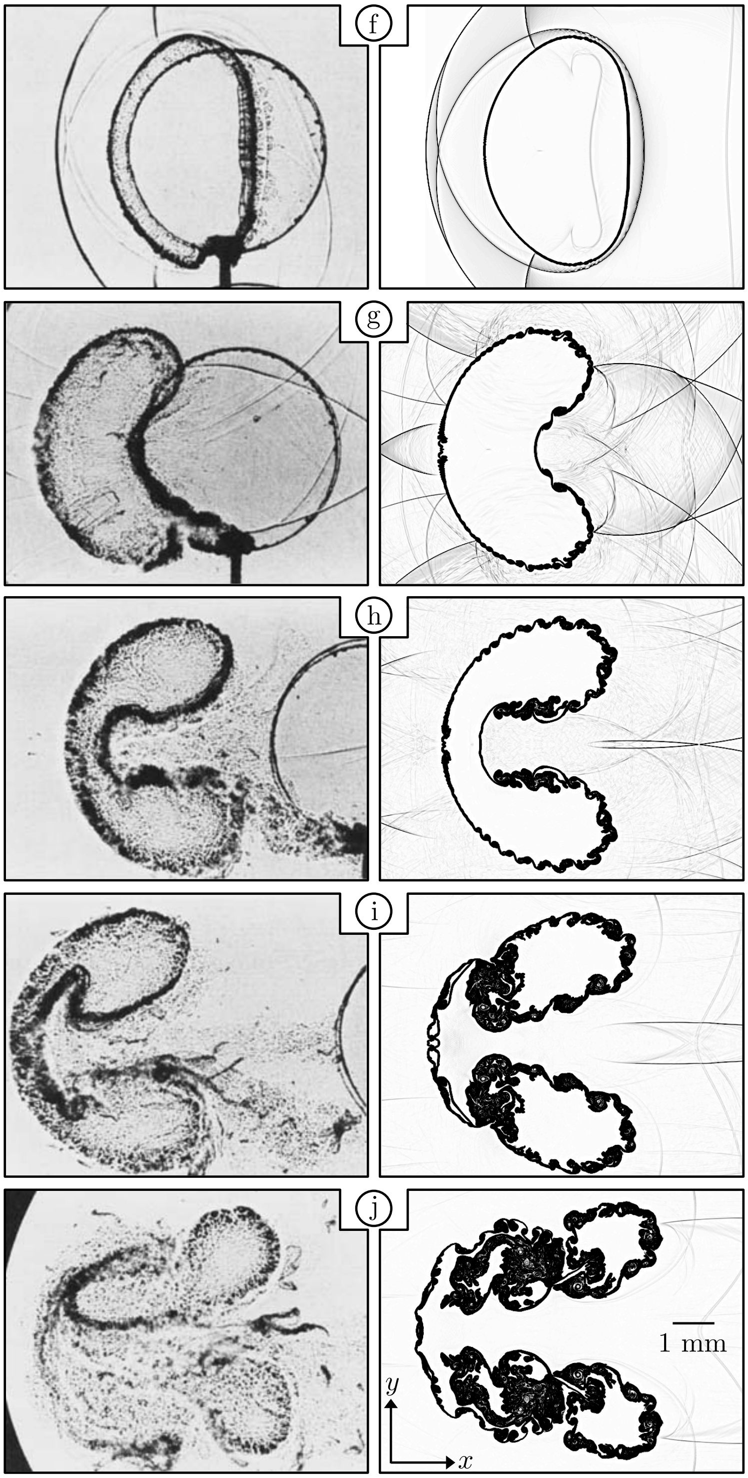

Figure 3.6: (Cont.) Comparison between the experimental shadowgraphs of Haas and Sturtevant [52] (left) and numerical Schlieren images from simulation (right) for the shock-bubble interaction problem. The numerical Schlieren imaging technique is adapted from [93]. Temporal snapshots are included at f) 102, g) 245, h) 427, i) 674 and j) 983 μs. Experimental images ©Cambridge University Press 1987. Reprinted with permission.

Table 3.1: Comparison between the present simulation and the experiment of Haas and Sturtevant [52] of the velocities of various flow features for the shock-bubble interaction problem. These include, along with the time interval in the simulation over which they were averaged, the velocities of the incident shock, u_s $[-60, 0]$, refracted shock, u_r $[0, 52]$, transmitted shock, u_t $[52, 240]$, upstream interface, u_ui $[10, 52]$, downstream interface, u_di $[140, 240]$, and jet, u_j $[140, 240]$. The velocities and time intervals are given in m/s and μs, respectively, and the corresponding flow features are identified in Figure 3.6. All measurements are taken along the x-axis.

Data	u_s	u_r	u_t	u_ui	u_di	u_j
Simulation	420	945	379	173	145	230
Experiment	410 ± 41	900 ± 90	393 ± 39	170 ± 17	145 ± 15	230 ± 23

simulation. The flow features include the incident shock, refracted shock, transmitted shock, upstream interface, downstream interface and jet, and are annotated in the numerical Schlieren images a) and d) of Figure 3.6. In Table 3.1, a side-by-side comparison of the experimental and simulation results is made. The velocity measurements from the simulation are all within the 10% experimental error associated with the measurements of Haas and Sturtevant and, in general, fall within 5% of the experimental mean values. Though we do not report the uncertainty in the velocity measurements from the simulation, we expect it to be small and solely a function of the grid resolution. Indeed, since all conserved variables are conserved within round-off error, $\mathcal{O}(10^{-12})$ in this case, we expect that all flow features move with the correct velocities.

Lastly, we compare the present results to those of recent numerical simulations performed at a higher or comparable resolution. These include the work of Hejazialhosseini *et al.* [55], who utilized a level set method on wavelet-adapted grids with an effective resolution of $\Delta x = \Delta y = 6$ μm, and the work of So *et al.* [106], who utilized a diffuse interface method with interface sharpening on a uniform grid with $\Delta x = \Delta y = 63$ μm. Their results are consistent with ours, as we recover qualitatively similar large- and small-scale flow features. In particular, the Kelvin-Helmholtz instability that develops along the interface of the bubble, and is clearly visible in images g)–j) of Figure 3.6, is in good agreement. The instability is triggered at an earlier time in the simulations of Hejazialhosseini *et al.* and So *et al.*, however, primarily because the ongoing diffusion of the material interface in the present simulation acts to regularize the material interface and delays the growth of the instability.

3.6.6 Taylor-Green vortex

We verify our numerical scheme for the Navier-Stokes equations by studying the evolution of a 3D Taylor-Green vortex. The latter is a typical test problem for high-order methods and one of the simplest in which the production of small scales can be studied. The initial condition for the Taylor-Green vortex is given by

$$\left.\begin{aligned} u &= u_\mathrm{o} \sin\left(\frac{x}{L}\right)\cos\left(\frac{y}{L}\right)\cos\left(\frac{z}{L}\right), \\ v &= -u_\mathrm{o} \cos\left(\frac{x}{L}\right)\sin\left(\frac{y}{L}\right)\cos\left(\frac{z}{L}\right), \\ w &= 0, \\ p &= p_\mathrm{o} + \frac{\rho_\mathrm{o} u_\mathrm{o}^2}{16}\left(\cos\left(\frac{2x}{L}\right) + \cos\left(\frac{2y}{L}\right)\right)\left(\cos\left(\frac{2z}{L}\right) + 2\right), \end{aligned}\right\} \tag{3.28}$$

where L, ρ_o, u_o and p_o are the reference length scale, density, velocity, and pressure in the problem, respectively. The fluid in which the vortex propagates is air, initially at uniform reference temperature, T_o, such that the initial condition for the density field is obtained from that for the pressure field using the ideal gas law. We evolve the vortex at a relatively low Reynolds number, $Re = \rho_\mathrm{o} u_\mathrm{o} L/\mu = 100$; an effectively incompressible Mach number, $M_\mathrm{o} = u_\mathrm{o}/c_\mathrm{o} = 0.1$; and in a periodic domain, $x, y, z \in [-\pi L, \pi L]$. The domain is discretized by a uniform grid with $200 \times 200 \times 200$ cells and we enforce fixed CFL and diffusion numbers, $C = 0.15$ and $D = 0.10$, to maintain stability throughout the simulation.

We evolve the Taylor-Green vortex until nondimensional time $t u_\mathrm{o}/L = 10$ in order to capture both the generation of the small scales, which result from 3D vortex stretching, and their subsequent dissipation, which is due to viscous damping. In Figure 3.7, we depict the former process with a plot of the isosurfaces of the z-component of the nondimensional vorticity, $\omega_z L/u_\mathrm{o}$, at the initial and final moments of the simulation, where the vorticity is given by $\boldsymbol{\omega} = \nabla \times \mathbf{u}$. In Figure 3.8, both processes are illustrated with a plot of the rate of dissipation of the nondimensional kinetic energy, $\epsilon L/u_\mathrm{o}^3$, as a function of the nondimensional time. The rate of dissipation of the kinetic energy is

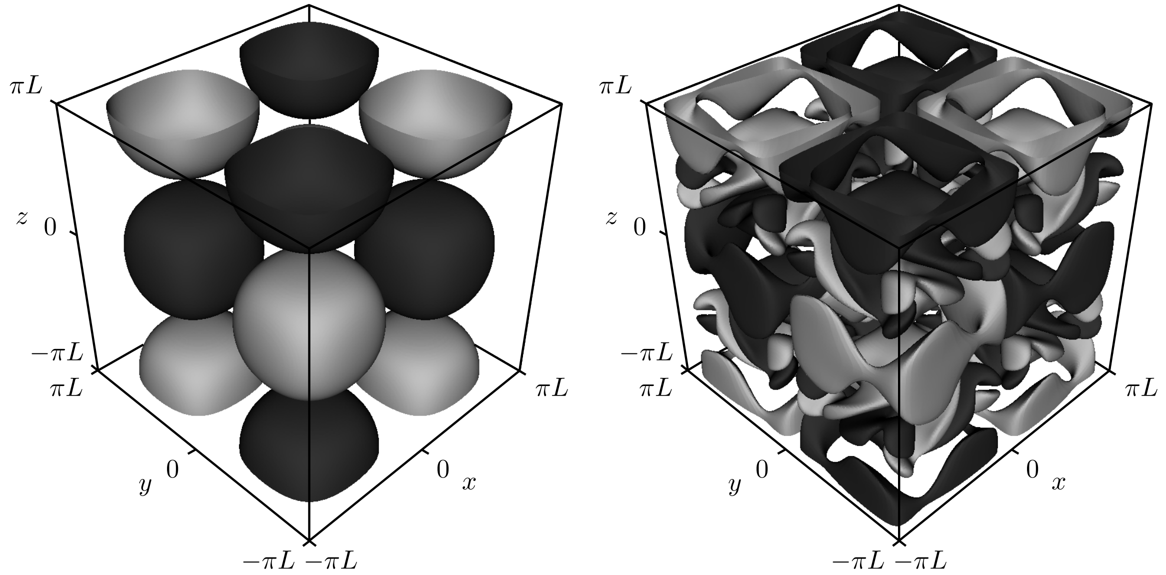

Figure 3.7: Plot of the isosurfaces of the z-component of the nondimensional vorticity, $\omega_z L/u_\text{o}$, for the Taylor-Green vortex problem at nondimensional times $tu_\text{o}/L = 0$ ($\omega_z L/u_\text{o} = \pm 0.33$, left) and $tu_\text{o}/L = 10$ ($\omega_z L/u_\text{o} = \pm 0.67$, right). The negative and positive isosurfaces of $\omega_z L/u_\text{o}$ are colored in black and gray, respectively.

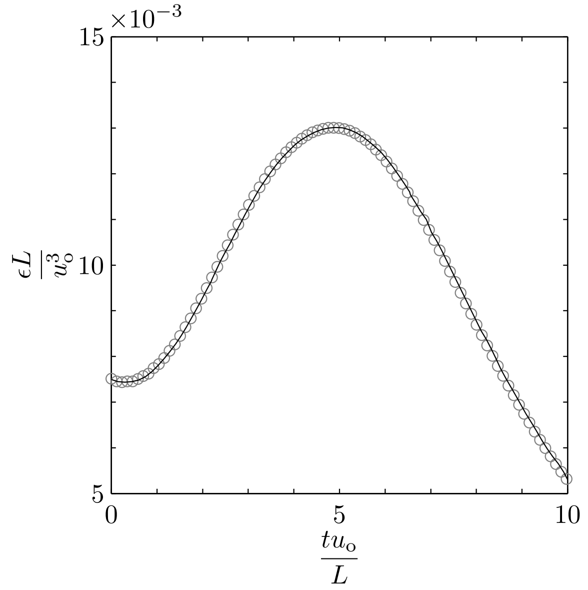

Figure 3.8: The rate of dissipation of the nondimensional kinetic energy as a function of the nondimensional time for the Taylor-Green vortex problem. The solution from the present numerical scheme (○) is compared to the direct spectral numerical solution of Brachet *et al.* [11] (—).

computed over the entire volume of the computational domain, V, by

$$\epsilon = -\frac{1}{\rho_\mathrm{o} V}\frac{\mathrm{d}}{\mathrm{d}t}\int_V \frac{1}{2}\rho\mathbf{u}\mathbf{u}\;\mathrm{d}V. \tag{3.29}$$

From Figure 3.8, we can see that the strength of the vortex stretching initially grows, until $tu_\mathrm{o}/L \approx 5$, when the effects of viscous dissipation begin to dominate. The present numerical solution compares well to the direct spectral numerical solution of Brachet *et al.* [11], which is also included in the figure. Though not shown, the Taylor-Green vortex eventually decays away, due to the absence of forcing.

3.7 Summary

In this chapter, a shock- and interface-capturing numerical scheme was developed for the simulation of multicomponent flows governed by the compressible Navier-Stokes equations. The numerical framework is general, derived in 3D and on nonuniform grids. The resulting method is high-order accurate, discretely conserves the mass of each component in the flow, along with the total momentum and energy, and does not generate spurious oscillations. Moreover, it is capable of handling flows that feature large density, pressure, and viscosity ratios, as well as components with significantly different stiffened gas EOS parameters. In Chapter 4, the method is adapted for the simulation of the shock-induced collapse of a bubble in the free-field and a vessel phantom.

Chapter 4

Results

4.1 Simulation parameters

In this chapter, results of numerical simulations across the parameter space defined in Section 2.3.4 are presented. The simulations are carried out utilizing the numerical scheme of Chapter 3, with two notable exceptions: 1) A one-point Gaussian quadrature rule, rather than the two-point one that is described in Section 3.2, is employed to compute cell face averages and 2) the cell average primitive variables are computed directly from the cell average conservative variables, as in the original numerical method of Johnsen and Colonius [64], rather than from the point-wise reconstructed conservative variables, as proposed in Section 3.3. The latter choices are motivated by the significant reduction in computational cost that they provide, alongside the negligible impact that they have on key metrics extracted from the simulations, in spite of the fact that the simulations now only achieve second-order spatial accuracy in smooth flow regions. A detailed cost-benefit analysis of recovering high-order spatial accuracy in smooth regions of the flow is presently omitted. However, performance benchmarks of the modified numerical scheme are included and discussed in detail in Appendix F.

Each numerical simulation in the parameter space is carried out at a spatial resolution of $\Delta x^* = \Delta y^* = \Delta z^* = 6.26 \times 10^{-3}$, following the results of the convergence analyses of Johnsen and Colonius [66] and Freund *et al.* [43], who studied axisymmetric shock-induced collapse in the free-field and near a viscous fluid layer, respectively, at comparable pressures and viscosities investigated in the present work. Based on their findings, the chosen spatial resolution is expected to ensure that the minimum bubble volume and the extrema in the vessel wall displacements are sufficiently resolved, so that inherently, the remaining metrics describing the shock-induced collapse of the bubble and the resulting flow field deformations can also be expected to be correctly captured. A computational domain with $x^* \in [-2.5, 2.5]$ and y^*, $z^* \in [0.0, 2.5]$ is utilized in all free-field simulations, as well as in those of the vessel phantom, when the bubble is located on the x-axis, *i.e.* $\theta = 0$. For $\theta > 0$, a computational domain with x^*, $y^* \in [-2.5, 2.5]$ and $z^* \in [0.0, 2.5]$ is used instead. The mesh is uniform in all simulations, with non-reflective Thompson boundary conditions used to emulate the free-field [108, 109]. Following the discussion of Section 3.5, the material interfaces of the bubble and vessel are initially smeared in order to increase numerical stability. The smearing is performed over only five cells, based on the findings of Johnsen [63], which suggest that the present smearing will result in only negligible differences in the computed solutions. Finally, a fixed CFL number, $C = 0.1$, and diffusion number, $D = 0.1$, are utilized to maintain a stable time-step during the simulations.

4.2 Shocked-bubble dynamics in a free-field

The shock-induced collapse of a bubble in a free-field was simulated across several shockwave pressure ratios, $P_\mathrm{s}/P_\mathrm{o}$, spanning typical clinical SWL conditions, *i.e.* $P_\mathrm{s}/P_\mathrm{o} = 296$, 353, 493, 691, 888 and 1086. The resulting bubble dynamics, however, are generally well-understood and thus presently only broadly discussed in the context of a comparison between the results of this work and that of Johnsen and Colonius [66]. Such a comparison is necessary in order to verify that the chosen simulation parameters, discussed in Section 4.1, lead to adequately resolved solutions. For a more detailed analysis of free-field, shocked-bubble dynamics, the reader is referred to recent experimental [89, 94] and numerical [63, 112] studies which have particular relevance to SWL. The results of the present free-field simulations are also further explored in Section 5.4, but from the perspective of the flow field deformations induced by the shocked bubble.

In Figure 4.1, the simulation results of the present work are compared to those of Johnsen and

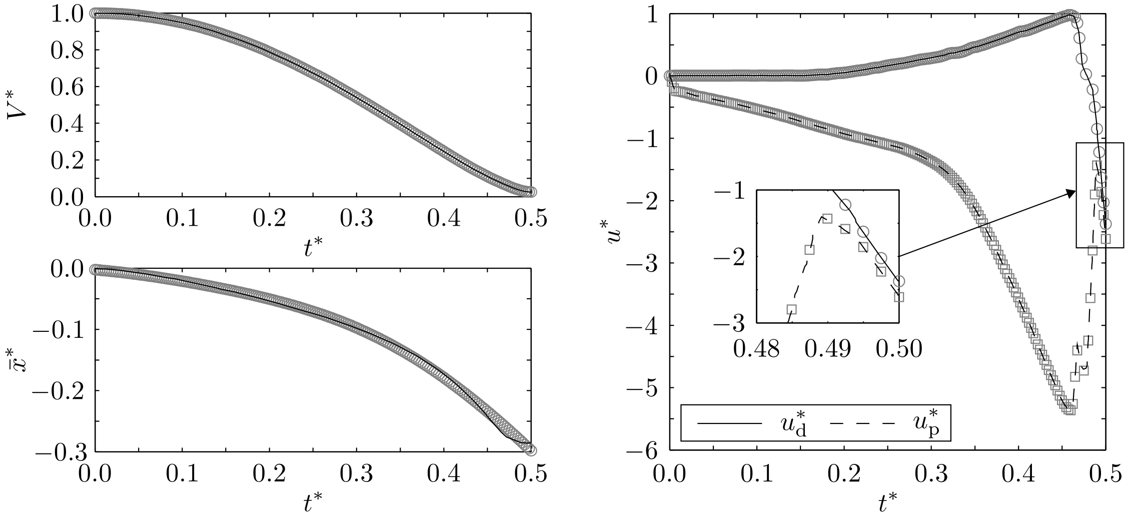

Figure 4.1: Time history of the bubble volume ($V^* = V/V_\text{o}$, top left), x-coordinate of the centroid ($\bar{x}^*$, bottom left) and distal and proximal interface velocities (u^*_d and u^*_p, right) for a free-field shock-induced collapse with $P_\text{s}/P_\text{o} = 353$. The present simulation results, which are plotted at discrete times, are compared to those of Johnsen and Colonius [66] up to the end of the collapse phase. A schematic of the measurement locations of u^*_d and u^*_p may be found in Figure 4.2.

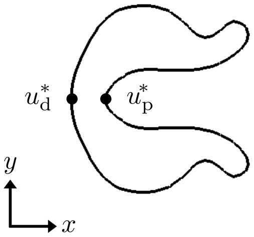

Figure 4.2: Schematic of the bubble in the x-y cross section of the 3D domain and at an arbitrary instant of its life cycle. It denotes the measurement locations of the distal and proximal bubble interface velocities (u^*_d and u^*_p).

Colonius [66] for the case of a shock-induced, free-field, bubble collapse with a pressure ratio of $P_\text{s}/P_\text{o} = 353$. The time history of the bubble volume, V^*, x-coordinate of the bubble centroid, $\bar{x}^*$, and the distal and proximal bubble interface velocities, u^*_d and u^*_p, are plotted up until the end of the collapse phase, when the minimum bubble volume is achieved. The measurement locations of the distal and proximal bubble interface velocities are indicated in Figure 4.2. Overall, the comparison with the simulation results of Johnsen and Colonius is favorable, demonstrating that the present simulation parameters are adequate to capture the dynamics of the bubble. Specifically, the minimum volume of the bubble, the motion of its centroid as it jets in the direction of the shockwave, as well as the extrema in the bubble interface velocities during jetting, are all in good agreement with the results of Johnsen and Colonius, indicating that sufficient grid resolution is used to resolve relevant flow features. Only a small discrepancy in the motion of the bubble centroid may be noted toward the end of the collapse phase, where the present simulation predicts the unhindered displacement of the bubble in the direction of travel of the shockwave, while the results of Johnsen and Colonius suggest that the displacement of the bubble is slowed. The latter behavior, however, is inconsistent with the results of previous studies [33, 72], which support the present findings. This inconsistency is unlikely to be symptomatic of a larger problem with the work of Johnsen and Colonius, based on the excellent agreement obtained with the remaining flow quantities, and perhaps only suggests a small issue with the post-processing methodology of the bubble centroid, which is exacerbated when the bubble volume becomes exceedingly small. The present simulation parameters thus adequately resolve the shocked-bubble dynamics in a free-field and moreover, are also expected to adequately resolve the bubble dynamics in a vessel phantom, as the latter occur on comparable spatial and temporal scales.

4.3 Shocked-bubble dynamics in a vessel phantom

4.3.1 Characterization of the time-dependent behavior

The shock-bubble interaction is now examined in the presence of a vessel phantom for a shockwave pressure ratio of $P_\mathrm{s}/P_\mathrm{o} = 395$. The strictest volumetric bubble confinement of the parametric study, *i.e.* $D_\mathrm{v}^* = 1.1$, see Table 2.2, is analyzed first to facilitate observations of the coupled shock-vessel-bubble dynamics. The bubble is centered inside the vessel, which is inviscid, and the travel direction of the shockwave is perpendicular to the vessel's axis, *i.e.* $(H_x^*, \theta) = (0, 0)$ and $Re_\mathrm{t} \to \infty$. Figures 4.3 and 4.4 document the shock-vessel-bubble interaction for this geometric configuration with time snapshots of notable instants of the shock-induced collapse. In Figure 4.3, the deformations of the bubble and vessel wall are rendered by isosurfaces of air and 10% gelatin, respectively, while in Figure 4.4, the interactions between different waves and material interfaces in the x-z plane are illustrated

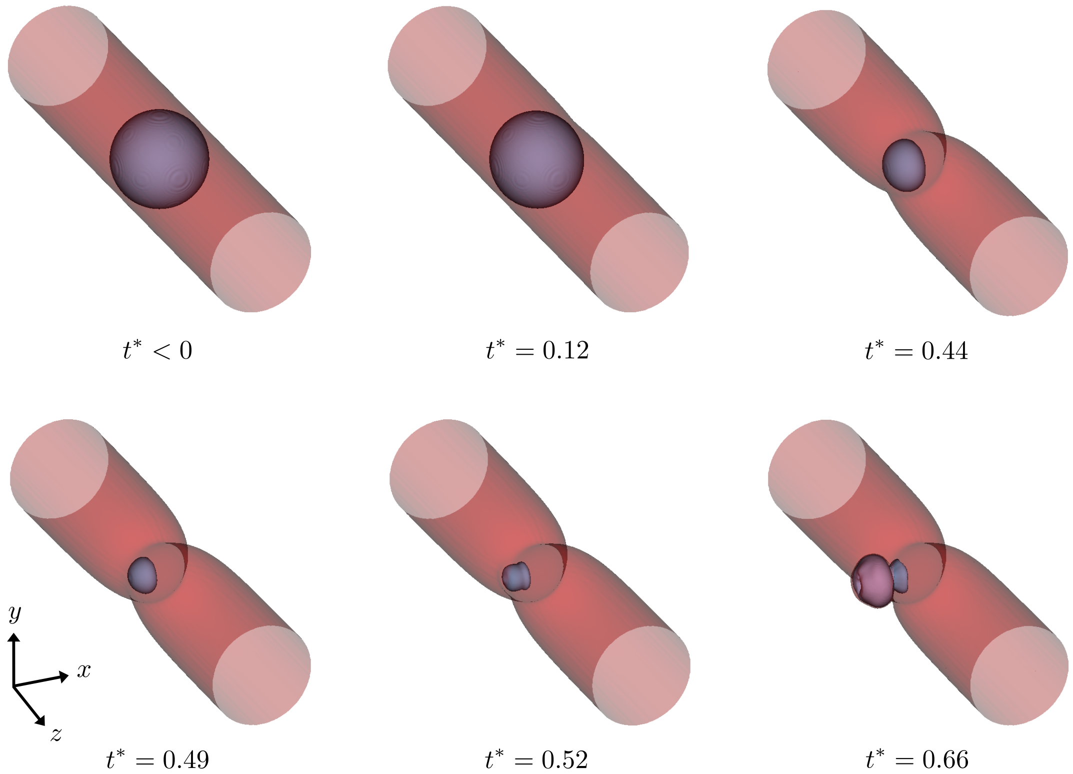

$t^* < 0$ $t^* = 0.12$ $t^* = 0.44$

$t^* = 0.49$ $t^* = 0.52$ $t^* = 0.66$

Figure 4.3: Time snapshots of the deformation of the bubble and the vessel wall for $(D_\mathrm{v}^*, H_x^*, \theta) = (1.1, 0, 0)$. The bubble is depicted by the 0.5 isosurface of the volume fraction of air and the vessel wall by the one of 10% gelatin.

by the pressure and velocity fields. The dynamics of the shock-vessel-bubble system are initiated as the left-moving shockwave, originally traveling in 10% gelatin, or tissue, for $t^* < 0$, is transmitted through the cylindrical water column, or vessel, and impacts the air bubble at $t^* = 0$. Since the acoustic impedance mismatch, *i.e.* ρc, between 10% gelatin and water is small, but that between water and air is large, the shockwave is predominantly transmitted through the vessel but only partly so through the bubble, against which it also reflects and diffracts in the form of an expansion wave. At $t^* = 0.12$, the shockwave has almost fully traversed the vessel but, due to the significantly lower sound speed in air compared to water, has only began to transmit through the bubble. This difference in sound speeds induces the proximal interface of the bubble, *i.e.* the side originally closest to the shockwave, to collapse first, invaginating the proximal wall of the vessel along the way. By $t^* = 0.44$, the shockwave has long left the domain and as a result, the distal interface of the bubble has also begun to collapse, invaginating the distal wall of the vessel. As the collapse progresses,

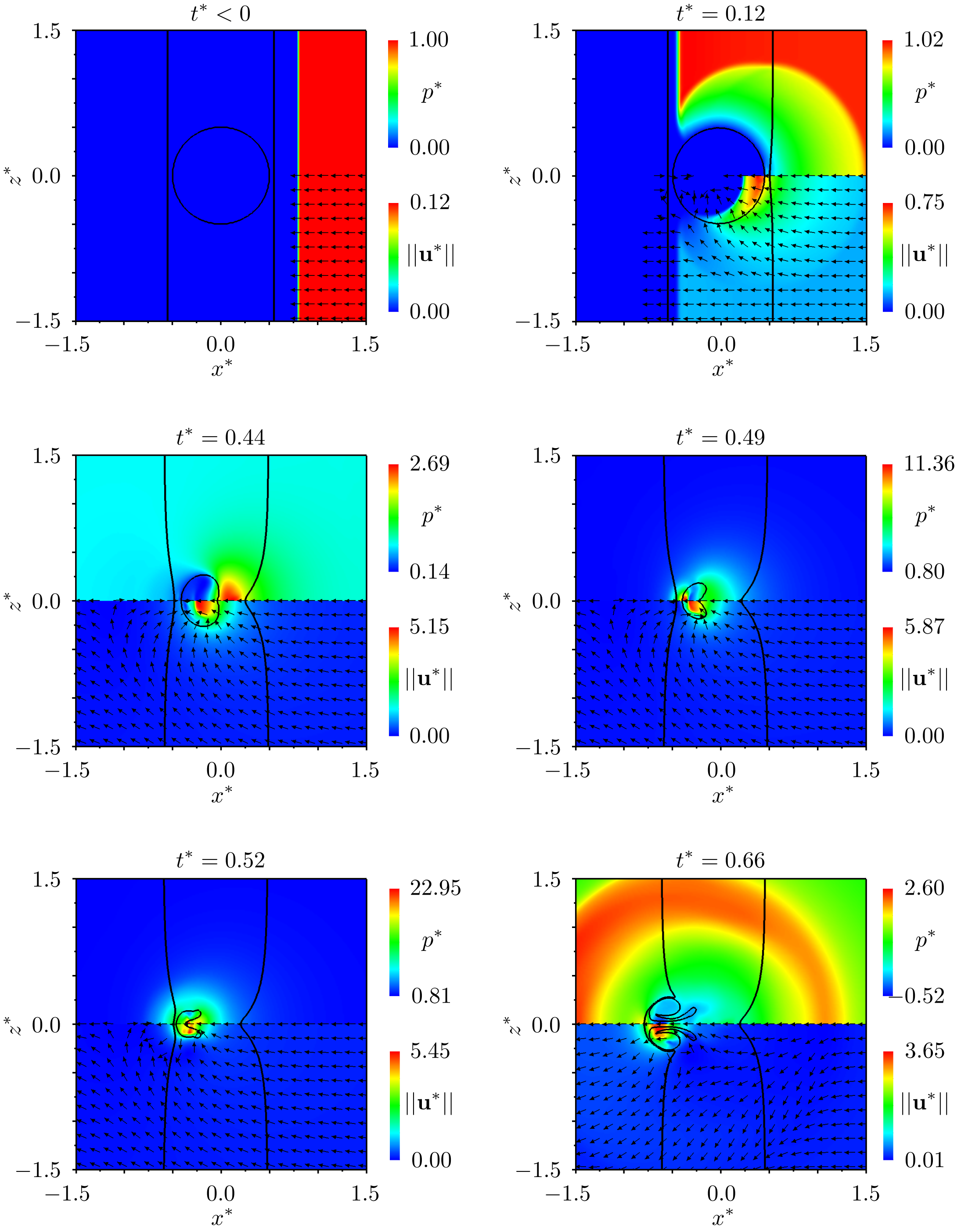

Figure 4.4: Time snapshots of the filled pressure contours (p^*, upper panel half), the filled velocity magnitude contours ($||\mathbf{u}^*||$, lower panel half) and the velocity vector field ($\mathbf{u}^*$, lower panel half) in the x-z cross section of the 3D domain for $(D_\mathrm{v}^*, H_x^*, \theta) = (1.1, 0, 0)$. For clarity, isopleths of the volume fractions of air and 10% gelatin are included as in Figure 4.3

.

the bubble continues to shrink and, in addition, translates in the direction of the propagation of the shockwave. The latter effect enhances the invagination of the proximal wall of the vessel, while discouraging that of the distal, which at $t^* = 0.49$ has reached its maximum. From here on, the bubble begins to directly interact with the proximal vessel wall, pushing it outward as it translates. The translation of the bubble is accelerated by the formation of the liquid jet, the presence of which is already evident in this snapshot, but far more pronounced at $t^* = 0.52$, when the minimum bubble volume is achieved. As the liquid jet forms, it impacts the distal bubble interface and vessel wall producing a strong water-hammer shockwave in the process. The latter propagates spherically from the point of origin, generating large pressures on both the proximal and distal vessel walls. Shortly after the water-hammer shockwave is emitted, the maximum invagination of the proximal vessel wall is achieved, while the distal vessel wall begins to distend, pushed outward by the force of the liquid jet. The final moments of the shock-vessel-bubble interaction, as simulated in this study, are captured at $t^* = 0.66$ and characterized by the continued distention of the distal vessel wall by a bubble that is now shaped like a vortex ring. At this instant in time, the water-hammer shockwave is also still visible, propagating outward, near the outskirts of the domain.

4.3.2 Influence of the vessel on the dynamics of the bubble

To better understand how the bubble dynamics are influenced by the presence of the vessel, the time history of various bubble metrics is charted in Figure 4.5. The metrics include the bubble volume, V^*, x-coordinate of the centroid, $\bar{x}^*$, and distal and proximal interface velocities, u_d^* and u_p^*, respectively; the measurement locations for the latter are annotated on the contour of the bubble in the x-z plane, in the schematic of Figure 4.2. The dynamics of the bubble are initially excited by the impact of the shockwave on its proximal interface, an event that is denoted by the sudden jump in the corresponding velocity. As this velocity grows in time, the proximal interface involutes, inducing the volume occupied by the bubble to slowly shrink and its centroid to begin traveling in the direction of the propagation of the shockwave. At $t^* = 0.16$, the passing shockwave has completed processing the bubble such that its distal interface has also begun to involute. As the

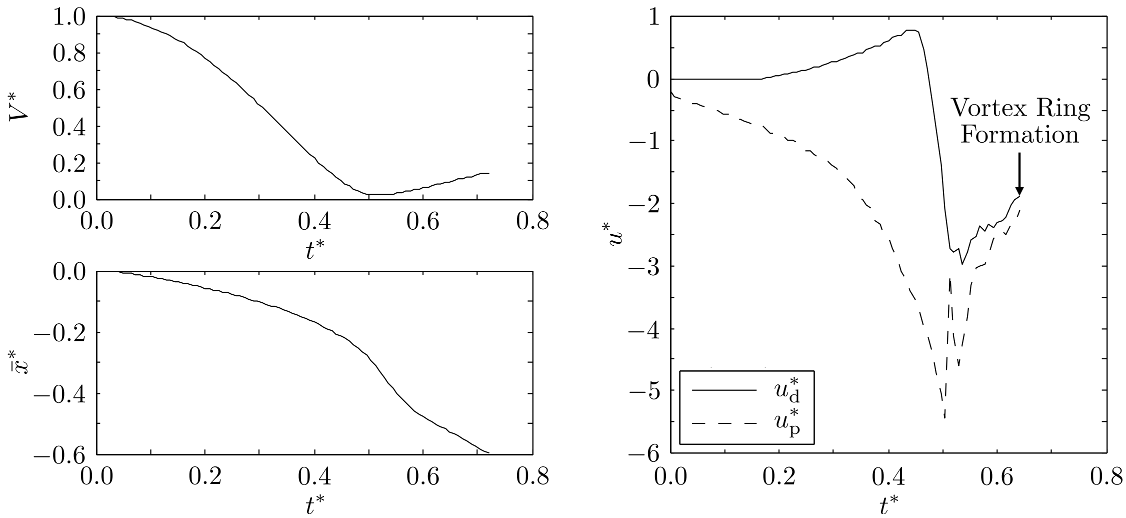

Figure 4.5: Time history of the bubble volume ($V^* = V/V_\mathrm{o}$, top left), x-coordinate of the centroid ($\bar{x}^*$, bottom left) and distal and proximal interface velocities (u_d^* and u_p^*, right) for $(D_\mathrm{v}^*, H_x^*, \theta) = (1.1, 0, 0)$. A schematic of the measurement locations of u_d^* and u_p^* may be found in Figure 4.2.

collapse of the bubble progresses, the pace accelerates, peaking shortly before the minimum bubble volume is reached. The minimum volume, $V^* = 2.19 \times 10^{-2}$, occurs at $t^* = 0.52$ and marks the end of the collapse phase. The liquid jet reaches its largest velocity, $u_\mathrm{p}^* = -5.43$, at $t^* = 0.50$. As the liquid jet nears the distal bubble interface, it begins to noticeably slow down, with the ensuing collision preceding the occurrence of the minimum volume. The formation and impact of the liquid jet leads both the distal and proximal bubble interfaces to travel in the direction of the propagation of the shockwave. Since the velocity of the proximal interface is larger, it eventually coalesces with the distal interface and the bubble forms a vortex ring at $t^* = 0.64$. In the final moments of the simulation, the bubble is in its rebound phase and so as its centroid continues to travel in the direction of the propagation of the shockwave, its volume slowly increases.

The extrema of the bubble metrics plotted in Figure 4.5 for $D_\mathrm{v}^* = 1.1$ are contrasted in Table 4.1 with those for $D_\mathrm{v}^* = 4.0$, a nearly fourfold difference in the diameter of the vessel that ensures that in the latter case the bubble negligibly interacts with the vessel walls. In Table 4.1, the minimum bubble volume, x-coordinate of the centroid and proximal interface velocity are listed. For both diameters, the values of these bubble metrics at $t^* = 0$ are $V^* = 1$, $\bar{x}^* = 0$ and $u_\mathrm{p}^* = 0$, so that the minima represent a significant deviation from the initial values. Table 4.1 indicates that the impact

Table 4.1: The minimum bubble volume, V^*_{min}, x-coordinate of the centroid, $\bar{x}^*_{\text{min}}$, and proximal interface velocity, $u^*_{\text{p,min}}$ and $u_{\text{p,min}}$, for $(D^*_{\text{v}}, H^*_x, \theta) = (1.1, 0, 0)$ and $(D^*_{\text{v}}, H^*_x, \theta) = (4.0, 0, 0)$.

D^*_{v}	V^*_{min}	$\bar{x}^*_{\text{min}}$	$u^*_{\text{p,min}}$	$\lvert u_{\text{p,min}}\rvert$ [m/s]
1.1	2.19×10^{-2}	-5.98×10^{-1}	-5.43	1061
4.0	2.30×10^{-2}	-6.02×10^{-1}	-5.04	985

of the vessel walls on the dynamics of the bubble are marginal. In fact, for the almost fourfold increase in the diameter of the vessel, between the largest and the smallest vessel confinement, the percent change in any one of the minima does not exceed 7%. Nevertheless, the collapse is somewhat stronger when the vessel walls are closer to the bubble, as suggested by the smaller bubble volume and larger liquid jet velocity that are achieved in this case. It is likely that this is primarily due to the internal reflections of the primary shockwave inside the vessel, which additionally process the bubble and induce a stronger collapse. This mechanism would play a smaller role in the case of a less restrictive vessel confinement since the shockwaves reflected inside the vessel would have to travel farther to once again process the bubble. The analogous mechanism is reported by Johnsen [63] for the shock-induced collapse of a bubble near a rigid wall. The data in Table 4.1 is consistent with previous findings and indicates that overall the vessel has a limited influence on the behavior of the bubble [41]. Since the properties of 10% gelatin are similar to those of water, see Table 2.1, this is not all that surprising and ultimately suggests that from the point of view of the bubble, the shock-induced collapse inside a vessel can adequately be approximated to that in a free-field. The maximum liquid jet speeds for $D^*_{\text{b}} = 1.1$ and 4.0 are listed in Table 4.1 and agree well with expected free-field values, around 1000 m/s [63, 71]. This finding is especially valuable from a computational cost perspective, since free-field simulations must evolve less flow variables and have potentially a higher degree of symmetry than simulations with a vessel phantom. Based on the performance benchmarks of the numerical scheme, see Appendix F, this suggests a 22% reduction in computational cost if only the number of flow variables in the problem is reduced and up to an 81% reduction in computational cost if the symmetry of the problem is also increased.

4.3.3 Vessel wall pressures and deformations

Seeing that the collapse of the bubble is insensitive to the presence of the vessel, from this point forward this study focuses on the reverse coupling. In Figure 4.6, the latter is explored through the time history of the distal and proximal vessel wall pressures, p_{d}^* and p_{p}^*, and deformations, d_{d}^* and d_{p}^*. The measurement locations of these metrics are annotated on the contour of the vessel wall in the x-z plane, in the schematic of Figure 4.7, and are selected based on the expected locations of the vessel wall pressure and deformation extrema. In Figure 4.6, the influence of the dynamics of the bubble onto those of the vessel is evident almost immediately after the impact of the primary shockwave on the proximal bubble interface. The latter, at $t^* = 0$, marks the beginning of the involution of that side of the bubble, which nearly simultaneously drives the invagination of the proximal vessel wall. The invagination of the distal vessel wall follows soon thereafter, around $t^* = 0.16$, when the shockwave has completed processing the entire bubble and the distal bubble interface involutes. In both cases, the invagination is due to the sink flow produced by the volumetric contraction of the bubble, which persists until the end of the collapse phase, at $t^* = 0.52$. However, the largest invagination of the distal vessel wall, $d_{\mathrm{d}}^* = -0.13$, is achieved before the end of the collapse phase, at $t^* = 0.49$, while that of the proximal vessel wall, $d_{\mathrm{p}}^* = -0.28$, is achieved afterward, at $t^* = 0.54$. This is attributable to the translation of the bubble, which, as the collapse progresses, moves away from the proximal vessel wall and closer to the distal wall. This is also the primary reason why the proximal vessel wall invaginates more than the distal one and ultimately, why the invagination of the latter is arrested shortly before the end of the collapse phase. Once the invagination of the vessel is complete, the remaining deformations are primarily due to the jetting of the bubble. The liquid jet impacts the distal bubble interface and vessel wall, almost simultaneously, at $t^* = 0.51$, and generates a water-hammer shockwave. This impact is immediately followed by a sustained decrease in the invagination of the distal vessel wall and a tremendous spike in its pressure, which peaks at $t^* = 0.53$ with $p_{\mathrm{d}}^* = 11.04$ and is due to the passage of the water-hammer shockwave. The proximal vessel wall remains largely unaffected by these events, only experiencing a slight reduction in its invagination when the water-hammer shockwave finally reaches it. This occurs at $t^* = 0.56$ and

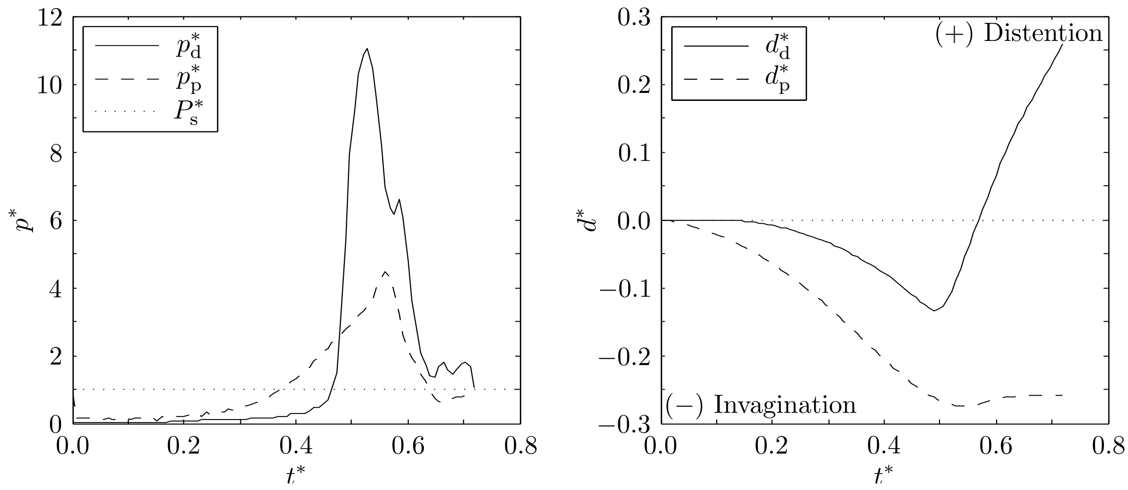

Figure 4.6: Time history of the distal and proximal vessel wall pressures (p_d^* and p_p^*, left) and deformations (d_d^* and d_p^*, right) for $(D_\mathrm{v}^*, H_x^*, \theta) = (1.1, 0, 0)$. The pressure associated with the initial shockwave, P_s^*, is plotted against p_d^* and p_p^* to illustrate the ability of the shock-induced collapse to amplify the strength of the primary shockwave. For a schematic of the measurement locations of p_d^*, p_p^*, d_d^* and d_p^* please refer to Figure 4.7.

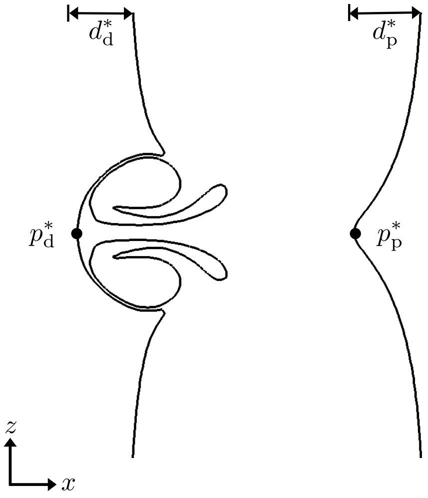

Figure 4.7: Schematic of the bubble and vessel in the x-z cross section of the 3D domain and at an arbitrary instant of their interaction for $\theta = 0$. It denotes the measurement locations of the distal and proximal vessel wall pressures (p_d^* and p_p^*) and deformations (d_d^* and d_p^*).

corresponds to the brief increase in the proximal vessel wall pressure, which peaks at $p_\mathrm{p}^* = 4.46$. From here on, since dissipative and elastic effects are neglected, the distal vessel wall continues to deform under the forcing of the liquid jet, while the proximal one remains invaginated. As such, the last moments of the simulation are characterized by the distention of the distal vessel wall, which is first achieved at $t^* = 0.57$ and further simulated until $t^* = 0.72$, when $d_\mathrm{d}^* = 0.26$.

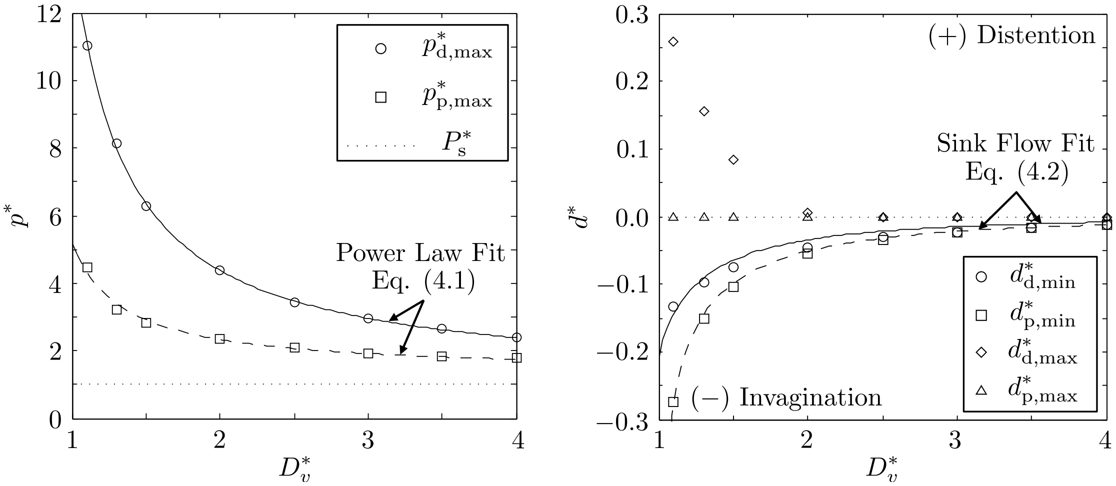

Figure 4.8: Effects of vessel confinement, D_{v}^*, on the extrema of the distal and proximal vessel wall pressures (p_{d}^* and p_{p}^*, left) and deformations (d_{d}^* and d_{p}^*, right) for $(H_x^*, \theta) = (0, 0)$. The pressure associated with the initial shockwave, P_{s}^*, is plotted against p_{d}^* and p_{p}^* to illustrate the ability of the shock-induced collapse to amplify the strength of the primary shockwave. For a schematic of the measurement locations of p_{d}^*, p_{p}^*, d_{d}^* and d_{p}^* please refer to Figure 4.7.

4.3.4 Effects of vessel confinement

Recall that in SWL, the onset of vascular injury is predominantly limited to small blood vessels, such as capillaries, arterioles and venules [26, 114, 118]. This suggests that the level of volumetric confinement of the bubble dynamics within a particular vessel may play a significant role in determining whether the latter is damaged or not during treatment. Then, to characterize the potential for vascular injury as a function of the vessel confinement, the vessel diameter is parametrically varied, $1.1 \leq D_{\mathrm{v}}^* \leq 4.0$, with the remaining aspects of the geometry of the problem held fixed, $(H_x^*, \theta) = (0, 0)$. The resulting extrema of the distal and proximal vessel wall pressures and deformations are plotted in Figure 4.8 and show a strong direct relationship between the strength of the volumetric confinement of the bubble and the potential for injury of the vessel. In other words, for the shock-induced collapse of a fixed-size bubble, centered inside a vessel, an increase in the diameter of the vessel brings about a decrease in the extrema of the distal and proximal vessel wall pressures and deformations and thus inherently, a decrease in the potential for vascular injury. The relationship between the vessel diameter and its wall pressure is readily fitted by a power law, Equation (4.1), while the analogous relationship for the wall invagination closely adheres to the potential theory of a sink flow, Equation (4.2)*:

$$p^*_{\text{max}}\left(D^*_{\text{v}}\right) = \frac{A}{D^*_{\text{v}} + 2\bar{x}^*_{\text{c}}} + B, \tag{4.1}$$

$$d^*_{\text{min}}\left(D^*_{\text{v}}\right) = \frac{1}{2}\left[\left({D^*_{\text{v}}}^3 + C\right)^{\frac{1}{3}} - D^*_{\text{v}}\right]. \tag{4.2}$$

In Equations (4.1) and (4.2), A, B and C are the fitting parameters and $\bar{x}^*_{\text{c}}$ is the x-coordinate of the centroid of the bubble at the end of the collapse phase, which is approximately equal to 0.33 for all vessel diameters, since the dynamics of the bubble are largely uninfluenced by the presence of the vessel, as discussed in Section 4.3.2. For the distal vessel wall, the fitting parameters are given by $A = 2.25$, $B = 1.05$, and $C = -0.80$, while those for the proximal vessel wall are given by $A = 0.66$, $B = 1.36$ and $C = -1.17$. The power law is typically used to correctly model the relationship between the maximum pressure experienced at a rigid planar wall and the distance of the latter away from a bubble at collapse [63, 65, 66, 72]. It fits the pressure data well, however, despite the compliance and displacement of the distal and proximal vessel walls. The sink flow model also constitutes a good fit to the invagination data, regardless of the displacement of the bubble and the asymmetry of its collapse.

4.3.5 Effects of bubble proximity

The effects of the proximity of the bubble to the distal and proximal vessel walls are parametrically investigated by varying the initial location of the bubble inside the vessel, along the x-axis, $-0.75 \leq H^*_x \leq 0.75$, while maintaining the remaining aspects of the geometry of the problem fixed, $(D^*_{\text{v}}, \theta) = (3, 0)$. The results are plotted in Figure 4.9 and illustrate the relationships between the proximity of the bubble to the distal and proximal vessel walls and the extrema of the measured vessel wall pressures and deformations. These relationships confirm, as one would already anticipate, that the extrema of the pressures and deformations at a particular vessel wall increase in magnitude with a decreasing stand-off distance of the initial position of the bubble, while the opposite is true

---

[*] This equation may be derived by assuming a 3D sink flow at the initial position of the bubble, described by the velocity potential $\phi(r) = -\frac{m}{4\pi r}$, where m is the sink strength and r is the radial distance from its origin, and evaluating the induced displacements at the position of the vessel walls along the x-axis.

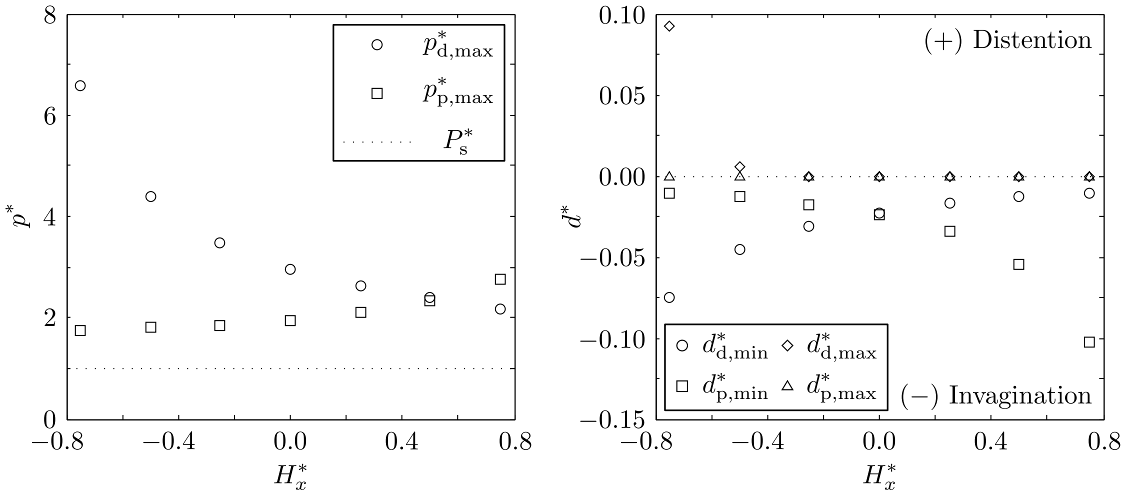

Figure 4.9: Effects of bubble proximity, H^*_x, on the extrema of the distal and proximal vessel wall pressures (p^*_{d} and p^*_{p}, left) and deformations (d^*_{d} and d^*_{p}, right) for $(D^*_{\mathrm{v}}, \theta) = (3, 0)$. The pressure associated with the initial shockwave, P^*_{s}, is plotted against p^*_{d} and p^*_{p} to illustrate the ability of the shock-induced collapse to amplify the strength of the primary shockwave. For a schematic of the measurement locations of p^*_{d}, p^*_{p}, d^*_{d} and d^*_{p} please refer to Figure 4.7.

when the stand-off distance increases. Naturally, the associated potential for vessel wall injury is expected to obey the exact same trend so that, as a result, an optimization problem regarding the minimization of the cumulative damage to the distal and proximal vessel walls arises with respect to the initial stand-off distance of the bubble from each side of the vessel. From Figure 4.9, the solution to the problem is evident and may be read off of the plot of the deformation data which indicates that when the bubble is approximately centered, the extrema of the distal and proximal vessel wall deformations are collectively lowest. This result is expected to be sensitive to the vessel to bubble diameter ratio and so, as part of future work, it may be instructive to perform a bubble proximity parametric study with respect to several of its values. This study would also address the complementary maximization problem, the solution to which identifies the position of a bubble within a vessel that leads to the largest cumulative damage. Ultimately, however, it would allow us to pinpoint the position and size of the smallest bubble, within a particular vessel, for which the shock-induced collapse induces sufficient vascular deformations to cause injury.

4.3.6 Effects of shockwave angle

The angle at which the shockwave impacts the blood vessel, as well as the bubble inside it, is likely to play a significant role in the assessment of the potential for vascular injury due to shock-induced collapse in SWL. Thus, as a first step, this study examines the range of incident shockwave angles defined by $0 \leq \theta \leq \pi/2$, in an otherwise fixed geometric configuration, where $D^*_\mathrm{v} = 3.0$ and $H^{*2}_x + H^{*2}_y = 0.75^2$. More precisely, four discrete shockwave angle values are considered; $\theta = 0$, $\pi/6$, $\pi/3$, and $\pi/2$, and their effect on the potential for vascular injury is evaluated by measuring the resulting extrema of the pressures and deformations at the vessel wall. At this time, the convention regarding the distal and proximal vessel walls is no longer practical, so that the extrema of the measured wall pressures and deformations are simply denoted by p^*_max, d^*_min and d^*_max, and are reported where they are the highest, which is usually in the vicinity of the location at which the bubble collapses. The results of this parametric study confirm that the shockwave angle plays a substantial role in determining whether a vessel wall near a collapsing bubble sustains any damage. This is supported by the sharp decrease in the maximum pressure and distention, associated with the impact of the liquid jet, that results from an increase of the angle of incidence of the shockwave from $\theta = 0$ to $\pi/2$. Recall that at $\theta = 0$ the liquid jet is directly aimed at the vessel wall and is therefore optimally oriented to induce injury, generating both a large vessel wall pressure, $p^*_\mathrm{max} = 6.57$, and distention, $d^*_\mathrm{max} = 9.27 \times 10^{-2}$. However, at $\theta = \pi/2$, the angle of incidence of the shockwave is such that the generated liquid jet predominantly travels alongside the curvature of the vessel, with the tip of the jet further away from the closest vessel surface, which results in a significantly reduced vessel wall pressure from the water hammer shockwave, $p^*_\mathrm{max} = 3.85$, and no distention. The maximum invagination of the vessel wall, on the other hand, associated with the decrease in the bubble volume, is far better sustained as a function of the shockwave angle, with $d^*_\mathrm{min} = -7.45 \times 10^{-2}$ at $\theta = 0$ and $d^*_\mathrm{min} = -8.97 \times 10^{-2}$ at $\theta = \pi/2$. This is not wholly unexpected since the sink flow which causes the invagination, though asymmetric, does act in all directions and is bound to be more insensitive to the angle of the shockwave than the liquid jet.

4.3.7 Effects of tissue viscosity

The parametric study of tissue viscosity is motivated by the magnitude of some of its larger estimates, see Section 2.1.2, which suggest that viscous effects may be able to significantly suppress vascular deformations induced by a collapsing bubble and thus prevent injury. Indeed, in a numerical study of shock-induced collapse near a planar viscous tissue simulant layer, Freund *et al.* [43] demonstrated that the collapse of a $D_\mathrm{b} = 20$ μm bubble by a $P_\mathrm{s} = 40$ MPa shockwave, *i.e.* $P_\mathrm{s}/P_\mathrm{o} = 395$, produced negligible deformations of a layer with a shear viscosity of $\mu_\mathrm{t} = 10$ Pa·s, *i.e.* $Re_\mathrm{t} = 0.4$, even if the bubble was initially in direct contact with the layer. A similar study is warranted in the case of a cylindrical vessel phantom, based on the added confinement that the geometry introduces. Presently, tissue Reynolds numbers as small as $Re_\mathrm{t} = 10$ are considered, based on the limitations of the numerical scheme, which due to the explicit treatment of viscous terms requires forbiddingly small time-steps at smaller Reynolds numbers. The smallest Reynolds number expected in tissue, $\mathcal{O}(10^{-2})$, see Section 2.1.4, is therefore not simulated. However, the latter also corresponds to estimated values of tissue viscosity measured at slow strain rates, $\mathcal{O}(10)$ Hz, and that at the megahertz deformation rates expected in SWL, the estimates of tissue viscosity are typically in excess of two orders of magnitude smaller, with the Reynolds number correspondingly larger. The $Re_\mathrm{t} = 10$ case is therefore arguably more relevant in application than studies at considerably smaller Reynolds numbers. Finally, though simulations at $Re_\mathrm{t} = 50$, 100 and 200 were also carried out, the differences with respect to the inviscid case were found to be negligible. As a result, only the $Re_\mathrm{t} = 10$ case is presently discussed and contrasted with the case without viscosity.

For comparison, the interaction between the bubble and vessel for both the inviscid and viscous case is illustrated in Figure 4.10 for $(D_\mathrm{v}^*, H_x^*, \theta) = (1.3, 0, 0)$ with snapshots of the solution along the x-z plane at important times during the life cycle of the bubble. These include a) the instant the proximal side of the bubble first involutes, b) when the minimum bubble volume is reached, c) when the vortex ring first forms and d) the last time at which the solution is computed. As anticipated, the effect of tissue viscosity is to inhibit the deformation of the vessel walls. This suppression, however, is less pronounced during the invagination of the proximal wall, where $d_{\mathrm{p,max}}^* = -0.15$ for $Re_\mathrm{t} \to \infty$

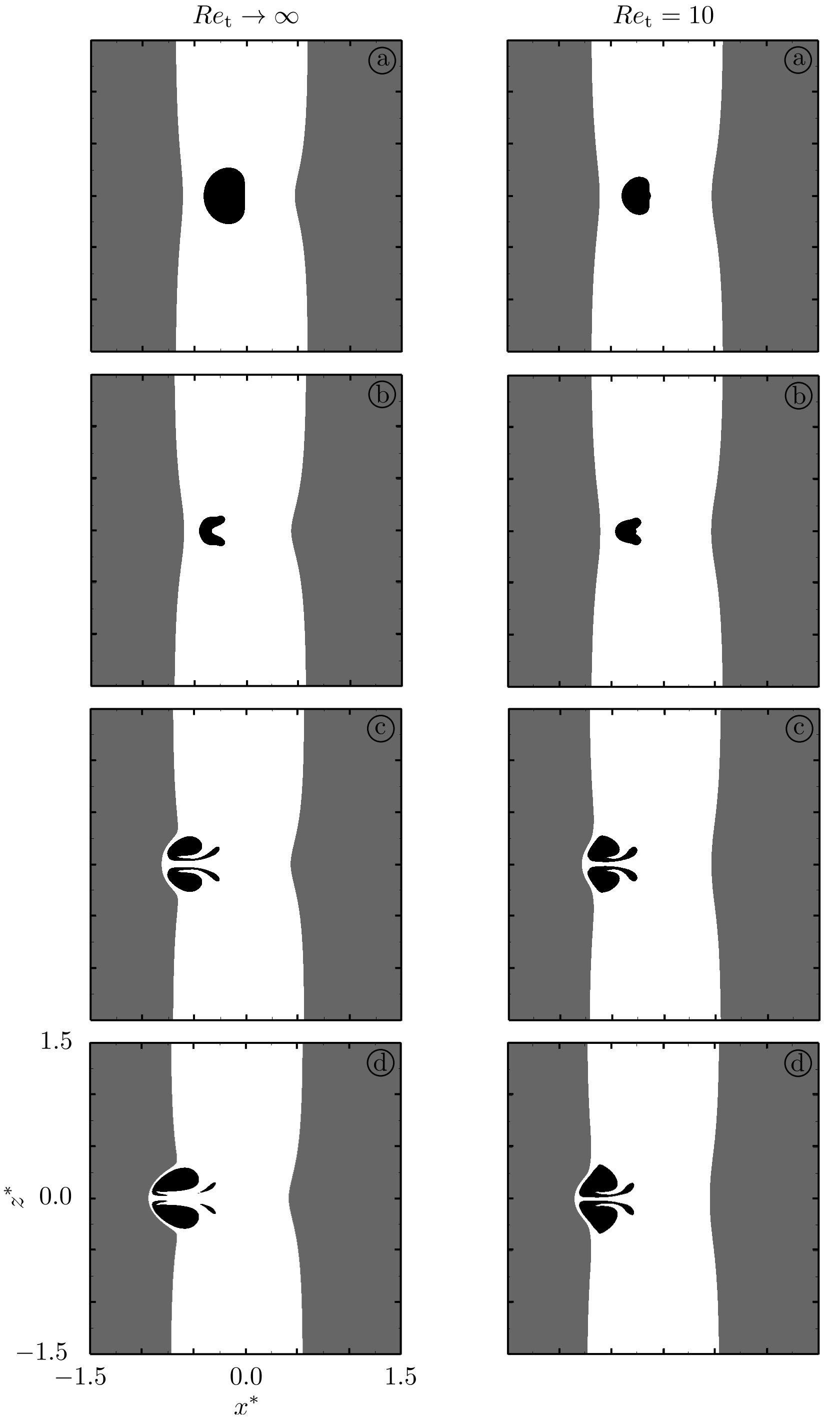

Figure 4.10: Temporal snapshots of the filled contours of the volume fractions of air (black), water (white) and 10% gelatin (gray) in the x-z plane of the 3D domain for the shock-induced collapse of a bubble in a viscous vessel phantom. The contour colors are saturated for volume fractions greater than 0.5. Results are shown for $Re_\mathrm{t} = 10$ (right panels) and t^* values of a) 0.51, b) 0.55, c) 0.71 and 0.79, as well as $Re_\mathrm{t} \to \infty$ (left panels) and t^* values of a) 0.45, b) 0.53, c) 0.70 and d) 0.79, for comparison.

and $d^*_{\mathrm{p,max}} = -0.12$ for $Re_{\mathrm{t}} = 10$, than the distention of the distal wall, where $d^*_{\mathrm{d,max}} = 0.22$ for $Re_{\mathrm{t}} \to \infty$ and $d^*_{\mathrm{d,max}} = 0.11$ for $Re_{\mathrm{t}} = 10$, most likely as a result of the finer spatial scales exhibited by the liquid jet, which are expected to enhance viscous effects. The difference in the distal wall deformation between the inviscid and viscous case will further increase as the jet propagates, since there is essentially no mechanism to suppress the penetration of the jet in the absence of viscosity. The difference in the vessel wall pressures, on the other hand, is nearly negligible between the two cases on both the distal side, where $p^*_{\mathrm{d,max}} = 8.31$ for $Re_{\mathrm{t}} \to \infty$ and $p^*_{\mathrm{d,max}} = 8.30$ for $Re_{\mathrm{t}} = 10$, and proximal side, where $p^*_{\mathrm{p,max}} = 3.23$ for $Re_{\mathrm{t}} \to \infty$ and $p^*_{\mathrm{p,max}} = 3.04$ for $Re_{\mathrm{t}} = 10$, suggesting not only that the strength of the collapse is not affected for this tissue viscosity and geometric configuration, but also that vessel wall pressure measurements are not robust indicators of the potential for vascular injury. Indeed, while small vessel wall pressures are typically measured alongside small vessel wall deformations, see Sections 4.3.4–4.3.6, and are thus suggestive of a low potential for vascular injury, the same direct relationship does not necessarily hold for large vessel wall pressures and a high potential for vascular injury, since the vessel wall deformations need not also be large. Brujan *et al.* [14] made comparable observations in an experimental study of the collapse of laser-induced cavitation bubbles near elastic boundaries.

While the strength of the bubble collapse is not affected, however, the shape of the bubble is significantly altered by tissue viscosity and the important moments in its life cycle are delayed compared to those of the inviscid case. The reason is that as the bubble collapses it seeks to draw fluid in, predominantly along the paths of least resistance. These lie along the primary axis of the vessel, while the paths of highest resistance are perpendicular to this axis and require the deformation of the vessel walls, which is resisted by the tissue viscosity. In particular, it is most difficult for the bubble to draw fluid in along its centerline, on its proximal side, as the wall of the bubble at that location is closest to the wall of the vessel, as measured in the direction of the propagation of the shockwave. This leads to a lag in the involution of the proximal bubble wall along the centerline and therefore the onset of a protrusion at this location in the early stages of the collapse, which is visible in Figure 4.10 snapshots a) and b) of $Re_{\mathrm{t}} = 10$, but not in the analogous snapshots of

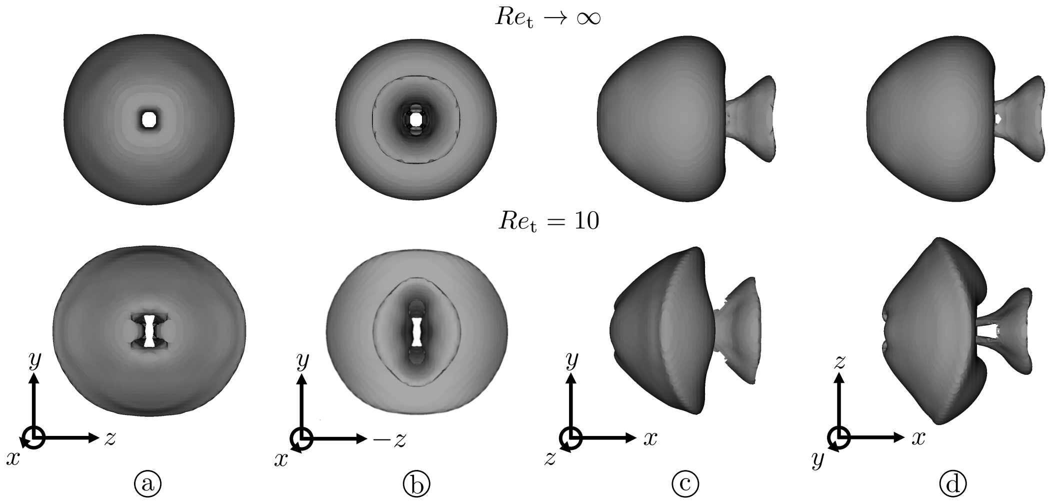

$Re_{\mathrm{t}} \to \infty$

$Re_{\mathrm{t}} = 10$

Figure 4.11: The a) front, b) back, c) side and d) top views of the shape of the bubble at $t^* = 0.79$ for the shock-induced bubble collapse in a viscous vessel phantom. The shape is given by the 0.5 isosurface of the volume fraction of air. Results are shown for $Re_{\mathrm{t}} = 10$ (bottom) and $Re_{\mathrm{t}} \to \infty$ (top).

$Re_{\mathrm{t}} \to \infty$. The protrusion eventually vanishes as the liquid jet forms and impacts the distal vessel wall, at which point the distal side of the bubble not only begins to deform the wall of the vessel but must also conform to its geometry due to the large tissue viscosity. The latter results in an oblong shape of the distal bubble wall, elongated in the direction of the primary axis of the vessel, which may more closely be observed in Figure 4.11, in the snapshots of $Re_{\mathrm{t}} = 10$. The same snapshots show the proximal side of the bubble to be elongated in an exactly perpendicular direction. This is not all that surprising and is simply a consequence of the retarded involution of the bubble walls along that direction during collapse, which is due to the increased resistance in the fluid flow along paths perpendicular to the primary axis of the vessel. On the other hand, the analogous snapshots of $Re_{\mathrm{t}} \to \infty$ show the final shape of the bubble to be nearly axisymmetric, despite the difference in the acoustic impedance between water and 10% gelatin.

4.4 Summary

In this chapter, the shock-induced collapse of a bubble in a free-field and inside a vessel phantom were simulated. The free-field simulations were carried out across typical clinical SWL pressure ratios, $296 \leq P_{\mathrm{s}}/P_{\mathrm{o}} \leq 1086$ [26]. For $P_{\mathrm{s}}/P_{\mathrm{o}} = 353$, the simulation results compared well with those of a previous convergence study [66], suggesting that the utilized simulation parameters adequately resolved the relevant spatial and temporal scales of the dynamics of the bubble. Identical parameters were subsequently employed in vessel phantom simulations, which are characterized by comparable spatial and temporal scales. The vessel phantom simulations were performed at the pressure ratio of a widely utilized clinical and research lithotripter, the Dornier HM3 [28], $P_{\mathrm{s}}/P_{\mathrm{o}} = 395$, and across a large parameter space that included the vessel to bubble diameter ratio, $1.1 \leq D_{\mathrm{v}}^{*} \leq 4.0$, the x-coordinate of the bubble within the vessel, $-0.75 \leq H_{x}^{*} \leq 0.75$, the angle at which the shockwave impacts the bubble and vessel, $0 \leq \theta \leq \pi/2$, and the tissue Reynolds number, $Re_{\mathrm{t}} \geq 10$. Vessel wall pressures and deformations were utilized to characterize the potential for vascular rupture and to identify potential injury mechanisms. The present results suggest that the invagination of the vessel, due to the volumetric compression of the bubble, and its subsequent distention, instigated by the impact of the liquid jet, are the primary mechanisms by which a vessel might be damaged. Moreover, the potential for injury is highest when the volumetric confinement of the bubble is strongest, the bubble is nearest the vessel wall, the angle of incidence of the shockwave is such that the distance between the jet tip and the nearest vessel surface is minimized and/or the tissue viscosity is low. In the next chapter, these results are expanded upon with estimates of the smallest bubble sizes needed to induce vascular rupture in the collapse and jetting phases, respectively.

Chapter 5

Estimates of the smallest injurious bubbles in shock-induced collapse

5.1 Overview

In Chapter 4, the potential for vascular rupture due to shocked bubbles was primarily characterized with vessel wall pressures and displacements. The use of these metrics, however, led to predominantly qualitative results, as vessel wall pressures were shown to not correlate directly with injury, see Section 4.3.7, and the sparseness of experimental work with shocked bubbles in vasculature inhibited comparisons with the measured vessel wall displacements. As a result, while trends in the potential for vascular rupture as a function of problem geometry, as well as tissue viscosity, were established, little could be said as to whether in any given case vascular injury could be expected to occur and if so, what size bubbles would be needed to cause it.

In the present chapter, these shortcomings are addressed by considering the finite strain fluid deformations induced by the shocked bubble. Unlike vessel wall pressures and displacements, strains provide a complete description of material deformations and failure, with experimental measurements of ultimate strains in tissue available for comparison, see Section 2.1.2. A method is thus developed to post-process from simulations the 3D, time-dependent, finite strains in proximity of a shocked bubble in order to estimate the smallest injurious bubbles in the collapse and jetting phases. The free-field simulations of Section 4.2, in particular, are considered in order to compute minima independent of problem geometry. The approach is expected to be valid for early times in the life cycle of the bubble and low estimates of tissue viscoelasticity, see Sections 2.1.4, 4.3.2 and 4.3.7. For the larger measurements of the tissue's properties, a model for spherical bubble dynamics in a viscoelastic material is utilized to adjust the free-field, collapse phase results [25]. A model for jet penetration into a viscous fluid is similarly adapted in order to estimate the smallest injurious bubbles in the jetting phase, for later times in the bubble's life cycle [43].

The remainder of this chapter proceeds as follows. In Section 5.2, a vascular rupture criterion based on the finite strain deformations of the fluid surrounding a shocked bubble is first proposed. A numerical method is then introduced in Section 5.3 to directly measure the finite strain field in free-field simulations. The typical time-dependent behavior of the strain field is discussed in Section 5.4, followed by estimates of the smallest injurious bubbles in the collapse and jetting phases in Sections 5.5 and 5.6, respectively. Finally, a summary of the results is presented in Section 5.7.

5.2 Criterion for vascular rupture

In order to define a criterion for vascular rupture due to the shock-induced collapse of a bubble, a fundamental understanding of the response of tissue on the microscale and under multiaxial loading is necessary. Recall from Section 2.1.2, however, that the tissue response under those conditions remains largely uncharacterized and only experimental results from the macroscale material response under uniaxial loading are readily available. The design of a vascular rupture criterion must thus utilize uniaxial loading results to predict rupture under multiaxial loading conditions. Presently, the von Mises strain is employed to consistently relate the states of strain resulting from the different loading modalities.

The von Mises strain is a measure of the deviatoric or shear strain energy in a material and is typically utilized as a yield criterion for isotropic ductile metals [85]. It is arguably also an appropriate injury criterion for tissue which though anisotropic is largely incompressible and can be expected to yield, or more precisely rupture, under shear rather than hydrostatic stress [42], akin to isotropic ductile metals. The underlying assumption of the von Mises criterion, however, is that regardless of the state of strain the failure of the material should occur when the stored shear strain energy exceeds a certain threshold. Unfortunately, it remains unclear from experiments whether this is the case in tissue. In the absence of experimental evidence, the use of the von Mises strain represents a best effort to establish a vascular rupture criterion for multiaxial loading conditions based on uniaxial results.

The design of the vascular rupture criterion is completed by determining the ultimate von Mises strains in tissue from the corresponding ultimate strains from uniaxial loading experiments which are given in Section 2.1.2. To do so, we begin with the expression for the Green-Lagrange finite strain tensor, $\mathbf{E}$:

$$\mathbf{E} = \frac{1}{2}\left(\mathbf{F}^{\mathrm{T}}\mathbf{F} - \mathbf{I}\right), \tag{5.1}$$

where $\mathbf{F}$ is the deformation gradient tensor. Under uniaxial loading and under the assumption that tissue can be approximated as isotropic, the deformation gradient tensor is diagonal in principal coordinates with $\mathbf{F} = \mathrm{diag}(\lambda_1, \lambda_2, \lambda_3)$, where λ_1, λ_2 and λ_3 are the stretch ratios in the principal directions. If tissue is further approximated as incompressible, *i.e.* $\det(\mathbf{F}) = 1$, and the loading takes place in the first principal direction, the stretch ratios along the directions orthogonal to the load are equal and can be expressed in terms of the first principal stretch: $\lambda_2 = \lambda_3 = \lambda_1^{-1/2}$. Utilizing the resulting deformation gradient tensor in Equation (5.1) yields a Green-Langrage finite strain tensor that is also diagonal and can be expressed solely as a function of the first principal stretch:

$$\mathbf{E} = \begin{pmatrix} \frac{1}{2}\left(\lambda_1^2 - 1\right) & 0 & 0 \\ 0 & \frac{1}{2}\left(\lambda_1^{-1} - 1\right) & 0 \\ 0 & 0 & \frac{1}{2}\left(\lambda_1^{-1} - 1\right) \end{pmatrix}. \tag{5.2}$$

In the uniaxial loading experiments in tissue, the first principal stretch may be obtained from the reported strain, since the latter is measured in the direction of the loading which is presently assumed to coincide with a principal direction in the material. Thus, using Equation (5.2), we see that the two quantities are related by

$$E_1 = \frac{1}{2}\left(\lambda_1^2 - 1\right) \tag{5.3}$$

so that the full state of strain is known for tissue under uniaxial loading conditions. The von Mises strain is then computed from

$$E_{\mathrm{vm}} = \sqrt{\frac{2}{3}\mathbf{E}_{\mathrm{d}} : \mathbf{E}_{\mathrm{d}}}, \tag{5.4}$$

where $\mathbf{E}_{\mathrm{d}}$ is the deviatoric component of the volumetric-deviatoric additive split of the Green-Lagrange finite strain tensor: $\mathbf{E} = \mathbf{E}_{\mathrm{v}} + \mathbf{E}_{\mathrm{d}}$, which reduces to $\mathbf{E} = \mathbf{E}_{\mathrm{d}}$ under the assumption that tissue is incompressible. The ultimate von Mises strains in tissue, $E_{\mathrm{vm,u}}$, may now be computed from the corresponding ultimate strains measured in uniaxial loading experiments by setting E_1 to E_{u} and utilizing Equations (5.2)–(5.4). The result of the procedure is an approximate range for $E_{\mathrm{vm,u}}$, given by $0.20 \leq E_{\mathrm{vm,u}} \leq 0.55$, which completes the design of the vascular rupture criterion. The criterion is then readily applied to free-field simulations where vascular rupture will be said to occur for a particular value of the ultimate von Mises strain if it is exceeded across a layer adjacent to the bubble that is thicker than the vessel wall.

5.3 Direct measurement of finite strain fluid deformations

To compute the time-dependent finite strains in the flow field surrounding the shocked bubble, a method developed by Senatore *et al.* [98] and utilized to extract strain information from 2D particle image velocimetry data of soil under a running gear is adapted and extended to 3D. In the present framework, the method relies on the advection of massless particles corresponding to the nodes of a finite element mesh to determine the strain in the flow field following standard finite element analysis procedures. The same finite element mesh is utilized in all free-field simulations, see Figure 5.1. It is generated with the Gmsh tool [45] and consists of approximately 17 million eight-node hexahedral

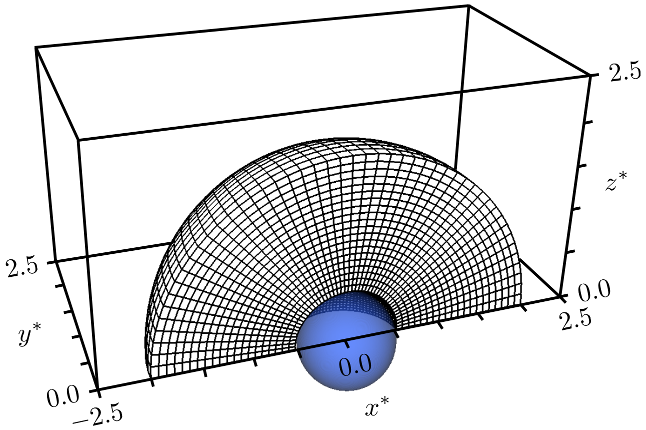

Figure 5.1: Finite element mesh at 1:1000 of the resolution utilized in the simulations. The mesh corresponds to a quarter of a hollowed out sphere and is shown in the computational box of the fluid solver where the bubble is depicted in blue. To reduce computational cost, exponential stretching is utilized to refine the mesh near the bubble and coarsen it away.

elements with about the same number of total nodes or particles. In each free-field simulation, the flow solver is provided with the node positions, which are then updated by integrating

$$\frac{\mathrm{d}\mathbf{x}_i}{\mathrm{d}t} = \mathbf{u}\left(\mathbf{x}_i, t\right), \quad i = 1, 2, ..., N \tag{5.5}$$

alongside Equations (2.1)–(2.5), where $\mathbf{x}_i$ is the node or particle position and N is the total number of particles. The particle velocity is determined through a linear interpolation of the average cell face velocities of the cell in which the particle is located, *i.e.* by utilizing Equation (3.14). Once the finite element mesh has been deformed by the flow field, trilinear shape functions are utilized to determine the deformation gradient tensor, $\mathbf{F}$, in each element, by taking the derivative of the position of an arbitrary point in an element's deformed body configuration, $\mathcal{B}_\mathrm{f}$, as given by $\mathbf{x}'$, with respect to the position of this point in the element's undeformed body configuration, $\mathcal{B}_\mathrm{o}$, as given by $\mathbf{x}$:

$$\mathbf{F} = \frac{\partial \mathbf{x}'}{\partial \mathbf{x}}. \tag{5.6}$$

The Green-Lagrange finite strain tensor, **E**, is easily computed therefrom using Equation (5.1), with the average value in each element directly approximated from that at the element center. Additional details on how the finite strain fluid deformations are post-processed may be found in Appendix G.

Despite the simplicity of this method, the analysis of fluid flow deformations with finite elements poses several difficulties, the most critical of which is the potential for mesh entanglement to occur. Such a scenario is unlikely to happen in the finite element analysis of a solid mechanics problem because the deformations are usually small, but may be challenging to avoid in the analysis of a flowing fluid, as large deformations are possible. The issue is addressed here by ensuring that the finite element mesh is sufficiently refined and not too close to the interface of the bubble, where the largest deformations are expected to occur. A stand-off distance of 10% of the bubble diameter of the mesh from the interface, as well as the present level of refinement, are sufficient to stave off mesh entanglement across the simulated shockwave amplitudes and times. Moreover, the utilized mesh resolution is also adequate to qualitatively study how the shock-induced collapse of the bubble deforms the surrounding liquid and to quantify the spatial extents of the region surrounding the bubble for which the strain is larger than the ultimate strain anticipated in tissue. In both cases, only negligible differences are noted upon doubling the resolution.

5.4 Characterization of the time-dependent strain field

To understand the mechanisms by which the flow field surrounding the bubble is deformed by its collapse, the time-dependent strain field induced by the interaction between a 30 MPa shockwave and a bubble is illustrated with snapshots of the filled contours of the von Mises strain (top panels) and pressure (bottom panels) in Figure 5.2. To facilitate the visualization of potential regions of injury, the strain contours are saturated at 0.55, the largest estimate of ultimate strain in tissue considered, while the color bar is adjusted such that the threshold between the colors green and yellow corresponds to the smallest estimate. In other words, strain thresholds of tissue are exceeded in the yellow and red regions, while there is negligible damage potential in the green regions. It is straightforward to observe then, at $t^* = 0.06$, that the passage of the shockwave produces negligible

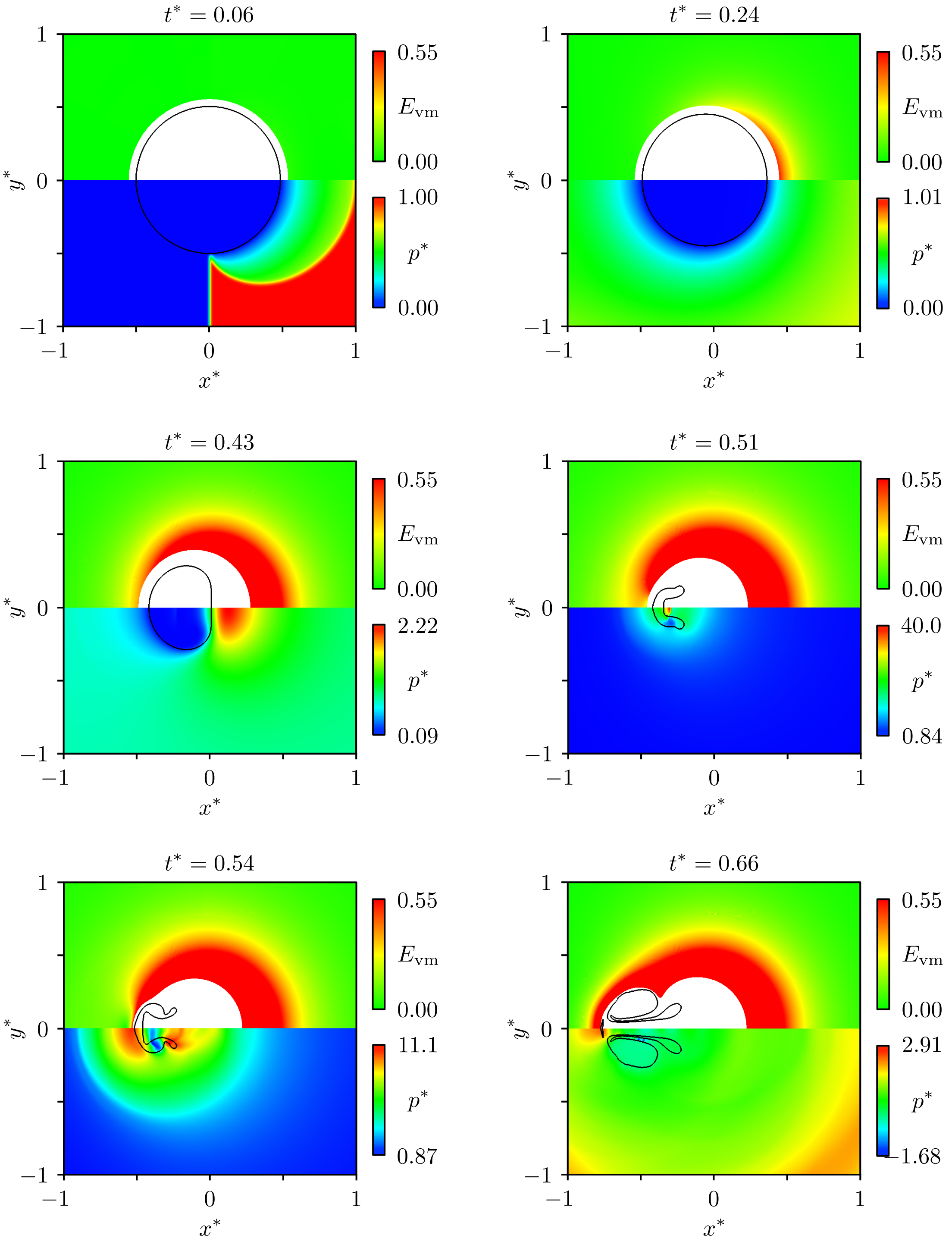

Figure 5.2: Temporal snapshots of the filled contours of the von Mises strain (E_{vm}, upper panel half) and pressure (p^*, lower panel half) in the x-y cross section of the 3D domain, where the bubble is depicted by the 0.5 isopleth of the volume fraction of air. The von Mises strain contours are saturated at 0.55, *i.e.* the largest ultimate strain of tissue considered, to facilitate visualization, since in a narrow layer adjacent to the bubble contour values can be several orders of magnitude larger.

deformations in the flow field and that the first potentially injurious strains are detected at the proximal side of the bubble, with the motion of the interface, as the bubble begins to visibly collapse around $t^* = 0.24$. At that time, however, the strains are still negligible on the distal bubble side, since the bubble translates as it collapses, offsetting the motion of its distal interface. This effect is overtaken in the snapshot of $t^* = 0.43$, where the bubble volume has significantly decreased and the resulting sink flow has induced injurious strains all around the bubble. The strain field remains asymmetric, however, as the bubble continues to translate during its collapse. The collapse phase terminates around $t^* = 0.51$, when the minimum bubble volume is achieved, which also marks the end of the sink flow mechanism and, resultantly, a slowdown in the growth of the injury region surrounding the bubble. The jetting phase then begins, as illustrated for $t^*= 0.54$, which initially reduces the deformation region induced by the sink flow on the distal side of the bubble, but subsequently results in its growth as the vortex ring propagates in the direction of the shockwave, see $t^* = 0.66$. Lastly, it is interesting to note that the emission of the water hammer shockwave, visible at $t^* = 0.54$, does not appear to correlate with an appreciable increase in damage potential, which is consistent with observations made in Section 4.3.7 for the viscous vessel phantom.

Though it may not be obvious from the snapshots of the filled von Mises strain contours in Figure 5.2 – as they are shown in the deformed body configuration, $\mathcal{B}_{\mathrm{f}}$ – the largest injury layer thicknesses induced by the collapse and jetting mechanisms are actually along the x-axis, on the proximal and distal sides of the bubble, respectively. Measurements of the injury region at those locations will therefore be useful in estimating for each mechanism the smallest bubble sizes that can potentially rupture a blood vessel. In Figure 5.3, the time history of the distal and proximal injury layer thicknesses, h^*_{d} and h^*_{p}, as measured in the undeformed body configuration, $\mathcal{B}_{\mathrm{o}}$, are shown across several estimates of the ultimate von Mises strain in tissue. While it is safe to assume that the thin region immediately adjacent to the bubble, where the strains are not available, is also eventually damaged, it is presently not included in the measurements. Though a lot of the same time-dependent features of the injury layer thickness that were observed in Figure 5.2 may also be observed here, notable exceptions include the approximately linear growth of the distal injury layer

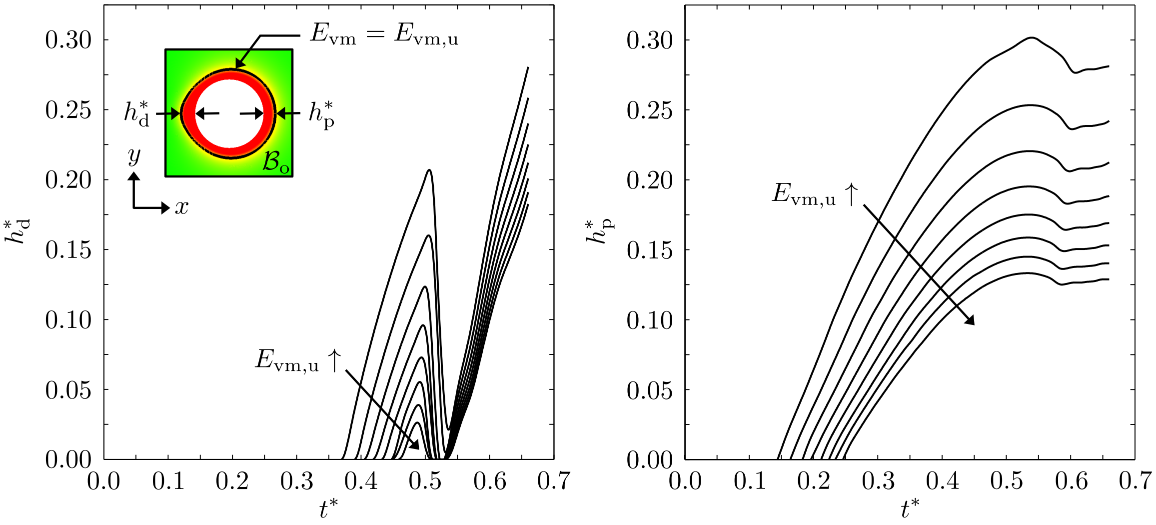

Figure 5.3: Time history of the distal injury layer thickness (h_{d}^*, left) and proximal injury layer thickness (h_{p}^*, right) for ultimate von Mises strains, $E_{\mathrm{vm,u}}$, of 0.20, 0.25, ..., and 0.55. Both measurements are taken in the undeformed body configuration, $\mathcal{B}_{\mathrm{o}}$, as shown the schematic in the top left corner, which depicts the filled contours of the von Mises strain at an arbitrary time and in the x-y cross section of the 3D domain.

thickness in the jetting phase and an initial drop in the thickness of the proximal injury layer at the end of the collapse phase. The latter event corresponds to the release of the water hammer shockwave which acts to slow the motion of the fluid on the proximal side of the bubble and thus contributes to the observed decrease in the injury region. Lastly, as might be expected, the thickness of the injury region on both the distal and proximal side of the bubble is observed to strongly depend on the estimated value of the ultimate strain in tissue. Specifically, both the distal and proximal thicknesses grow faster and achieve higher values as the ultimate strain decreases.

5.5 Estimates of the smallest injurious bubbles in the collapse phase

5.5.1 Spherical bubble dynamics in a viscoelastic material

Recall that in Section 2.1.4, the neglect of capillary, viscous and elastic effects in the study of shock-induced bubble collapse in a vessel was motivated by a nondimensional analysis of the spherical bubble dynamics model of Church and Yang [25], which describes the motion of a bubble in a fluid that is surrounded by a viscoelastic material. The model is now introduced as a means to quantify the error in the minimum bubble sizes, as a function of tissue viscosity and elasticity, that are predicted to result in vascular injury during the collapse phase by the free-field, shock-induced bubble collapse simulations. The error is estimated by comparing spherical collapses with and without viscoelastic effects, with the expectation that the estimated error will be comparable in the case of asymmetric collapses as the latter occur on the same temporal and spatial scales [63] and only strongly break symmetry upon the formation of the liquid jet, which nearly coincides with the end of the collapse phase, when the minimum bubble volume is achieved [63].

The model of Church and Yang [25] couples the Keller-Miksis equation for spherical bubble dynamics to the Kelvin-Voigt constitutive relationship for a viscoelastic material. The Keller-Miksis model is a second-order, nonlinear, ordinary differential equation that accounts for the effects of surface tension, liquid viscosity and to first-order in Mach number, liquid compressibility, on the motion of the bubble. It is given by

$$R_{\mathrm{b}}\ddot{R}_{\mathrm{b}}\left(1-\frac{\dot{R}_{\mathrm{b}}}{c_{\mathrm{l}}}\right)+\frac{3}{2}\dot{R}_{\mathrm{b}}^{2}\left(1-\frac{\dot{R}_{\mathrm{b}}}{3c_{\mathrm{l}}}\right)=\frac{1}{\rho_{\mathrm{l}}}\left[\left(1+\frac{\dot{R}_{\mathrm{b}}}{c_{\mathrm{l}}}\right)\left(p_{\mathrm{b}}-P_{\infty}\right)+\frac{R_{\mathrm{b}}}{c_{\mathrm{l}}}\left(\dot{p}_{\mathrm{b}}-\dot{P}_{\infty}\right)\right], \tag{5.7}$$

where R_{b} is the radius of the bubble, c_{l} is the sound speed in the liquid, p_{b} is the pressure on the outer surface of the bubble, P_{∞} is the pressure of the far-field, and the overset dot indicates a time derivative. Assuming that the contents of the bubble behave adiabatically and consist of only non-condensable gas, the pressure on the outer surface of the bubble is simply given by

$$p_{\mathrm{b}}=\left(P_{\mathrm{o}}+\frac{2\sigma}{R_{\mathrm{b},0}}\right)\left(\frac{R_{\mathrm{b},0}}{R_{\mathrm{b}}}\right)^{3\gamma_{\mathrm{g}}}-\frac{2\sigma}{R_{\mathrm{b}}}, \tag{5.8}$$

where $R_{\mathrm{b},0}$ is the initial radius of the bubble. The expression for the far-field pressure, on the other hand, is more complicated and is utilized to couple the viscoelastic effects of the Kelvin-Voigt material to the Keller-Miksis equation through the linear stress-strain relationship

$$\tau_{rr} = 2\left(G\gamma_{rr} + \mu_{\mathrm{t}}\dot{\gamma}_{rr}\right), \tag{5.9}$$

where τ_{rr} and γ_{rr} are the normal components in the radial direction of the deviatoric stress and strain tensors, respectively. The expression for the far-field pressure, accounting for viscoelastic effects, is then given by

$$P_\infty = P_{\mathrm{o}} + P_{\mathrm{s}}H(t) + \frac{4G}{3}\left[1 - \left(\frac{R_{\mathrm{v},0}}{R_{\mathrm{v}}}\right)^3\right] + \frac{4\dot{R}_{\mathrm{b}}}{R_{\mathrm{b}}}\left[\mu_{\mathrm{l}}\left(\frac{R_{\mathrm{v},0}^3 - R_{\mathrm{b},0}^3}{R_{\mathrm{v}}^3}\right) + \mu_{\mathrm{t}}\left(\frac{R_{\mathrm{b}}}{R_{\mathrm{v}}}\right)^3\right], \tag{5.10}$$

where H is a Heaviside function and R_{v} is the radius of the vessel, or more precisely, the radius of the spherical cavity in the Kelvin-Voigt material which confines the liquid and bubble. Equations (5.7), (5.8) and (5.10) constitute the bubble-liquid-tissue model of Church and Yang, albeit a simplified form, based on the assumption that the density of tissue is equivalent to that of the liquid, which is justified following the discussion of Section 2.1.4. The model will furthermore only be considered in the case of an infinitesimal liquid layer, *i.e.* $R_{\mathrm{b}} = R_{\mathrm{v}}$, in order to maximize the influence of the presence of tissue on the dynamics of the bubble, in an effort to establish conservative estimates of the error in the minimum bubble sizes predicted to result in vascular injury.

The model of Church and Yang [25] is solved by rewriting the expressions in Equations (5.7), (5.8) and (5.10) as a system of first-order linear ordinary differential equations, which are subsequently numerically approximated with the MATLAB `ode45` algorithm. The computations are carried out across the parameter space spanned by the range of bubble sizes and tissue viscoelastic properties established in Sections 2.1.1 and 2.1.2, respectively, with the remaining model parameters chosen so to as closely as possible match those used in the free-field, shock-induced bubble collapse simulations. However, capillary effects between the bubble and liquid are included in the spherical bubble dynamics model. The computational parameter space is discretized uniformly across the range of bubble diameters and logarithmically across the range of tissue viscosities and elasticities, in each case with 100 points. For comparison, solutions are also obtained in the absence of surface tension, viscosity and elasticity. The error in the minimum bubble sizes predicted to result in vascular injury is estimated by determining the maximum injury layer thickness produced by latter bubbles sizes in the spherical bubble dynamics model, in the absence of surface tension, viscosity and elasticity, and comparing them to the bubble sizes that are necessary to obtain the same maximum injury layer thickness when the latter effects are included. As before, the injury layer thickness is defined as the region immediately adjacent to the bubble across which the von Mises strain exceeds its ultimate value for tissue.

For the sake of consistency, the von Mises strain is once again computed from the finite strain tensor, despite the use of a linear constitutive relationship for tissue. This choice is sensible based on the large strains that are expected during the collapse phase [33], but calls into question the merit of utilizing a constitutive relationship based on small strains. The latter is justified here by the uncertainty in the mechanical properties of tissue and the resulting difficulty in fitting a more complex constitutive model. The finite von Mises strain in the Kelvin-Voigt material is computed from the spherically symmetric Green-Lagrange strain tensor,

$$\mathbf{E} = \begin{pmatrix} E_{rr} & 0 & 0 \\ 0 & E_{\theta\theta} & 0 \\ 0 & 0 & E_{\phi\phi} \end{pmatrix}, \tag{5.11}$$

which is equivalent to its deviatoric component, $\mathbf{E} = \mathbf{E}_\mathrm{d}$, since first-order compressibility effects only account for dissipation through acoustic radiation and not volumetric changes. Spherical symmetry with no volume changes also implies that $E_{\theta\theta} = E_{\phi\phi}$ and that $\mathbf{F}$ is a diagonal matrix with $\det(\mathbf{F}) = 1$, so that by utilizing Equation (5.1) the Green-Lagrange strain tensor can fully be expressed in terms of E_{rr}, *i.e.*

$$E_{\theta\theta} = \frac{1}{2}\left(\frac{1}{\sqrt{2E_{rr}+1}} - 1\right), \tag{5.12}$$

which, following a simplification of the Green-Lagrange strain-displacement relations in spherical coordinates, is given by

$$E_{rr} = \frac{\partial d_r}{\partial r} + \frac{1}{2}\left(\frac{\partial d_r}{\partial r}\right)^2, \tag{5.13}$$

where d_r is the displacement in the radial direction. The partial derivative of the radial displacement is obtained by integrating the radial velocity in the Keller-Miksis model in time, *i.e.*

$$u_r = \frac{R_{\mathrm{b}}^2 \dot{R}_{\mathrm{b}}}{r^2}, \tag{5.14}$$

and subsequently taking the partial derivative of the result in the radial direction to get

$$\frac{\partial d_r}{\partial r} = -\frac{2\left(R_{\mathrm{b}}^3 - R_{\mathrm{b},0}^3\right)}{3r^3}, \tag{5.15}$$

which incidentally corresponds to the small strain approximation, γ_{rr}. Finally, the finite von Mises strain is computed by using Equations (5.11)–(5.13) and (5.15) in Equation (5.4). This procedure is a simple matter of post-processing the bubble radius history obtained as part of the solution to Equations (5.7), (5.8) and (5.10).

5.5.2 Smallest injurious bubbles in absence of tissue viscoelasticity

To estimate the smallest bubbles able to rupture a blood vessel in the absence of the viscoelastic effects of tissue, the largest injury layer produced during the collapse phase in free-field simulations is considered. The latter is located at the proximal side of the bubble, along its centerline, see Section 5.4, with its thickness measured by $h_{\mathrm{p,max}}$, which includes the extent of the small region adjacent to the bubble for which the strain is unavailable but that can also be assumed injured. In Figure 5.4, $h_{\mathrm{p,max}}$ is plotted as a function of the initial bubble diameter, D_{b}, for several ultimate von Mises strains of tissue. A gray region is plotted for each ultimate strain, as spanned by the smallest and largest shockwave pressures considered, $P_{\mathrm{s}} = 30$ and 110 MPa, respectively. Regions

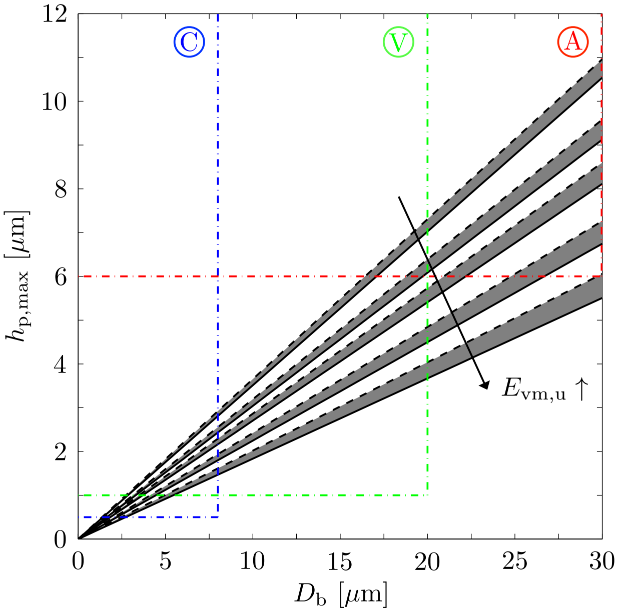

Figure 5.4: Maximum proximal injury layer thickness, $h_{\mathrm{p,max}}$, as a function of the initial bubble diameter, D_{b}, as predicted by the shock-induced, free-field, bubble collapse model. The gray regions correspond to ultimate von Mises strains, $E_{\mathrm{vm,u}}$, of 0.20, 0.25, 0.30, 0.40, and 0.55, and are spanned by the smallest (—) and largest (−−) shockwave pressures considered, 30 and 110 MPa. The injury regions for capillaries (C, −·−), venules (V,−·−) and arterioles (A, −·−) are also shown, with the right and bottom bounds of each region defined by the average vessel diameter and wall thickness, respectively. The inside of each injury region is denoted by the position of the label of the corresponding vessel.

bound by the average thicknesses and lumen diameters of capillaries, venules and arterioles are also included and serve to encompass those bubbles which not only can cause injury to the vessel but can also fit inside it. Thus for capillaries and venules, injurious bubbles sizes seem available across all of the estimated ultimate strains in tissue and clinical SWL pressure amplitudes, while for arterioles, rupture does not seem likely at the largest ultimate strain considered, $E_{\mathrm{vm,u}} = 0.55$, for almost any clinical shockwave strength. Moreover, bubbles smaller than approximately 1 μm appear harmless to the entire microvasculature, which is consistent with how injury is expected to be initiated in SWL, see Section 2.1.1.

5.5.3 Error in the estimates as a function of tissue viscoelasticity

The errors in the predicted bubble sizes resulting from neglecting tissue viscoelasticity are now estimated with the spherical bubble dynamics model of the previous section, by computing the

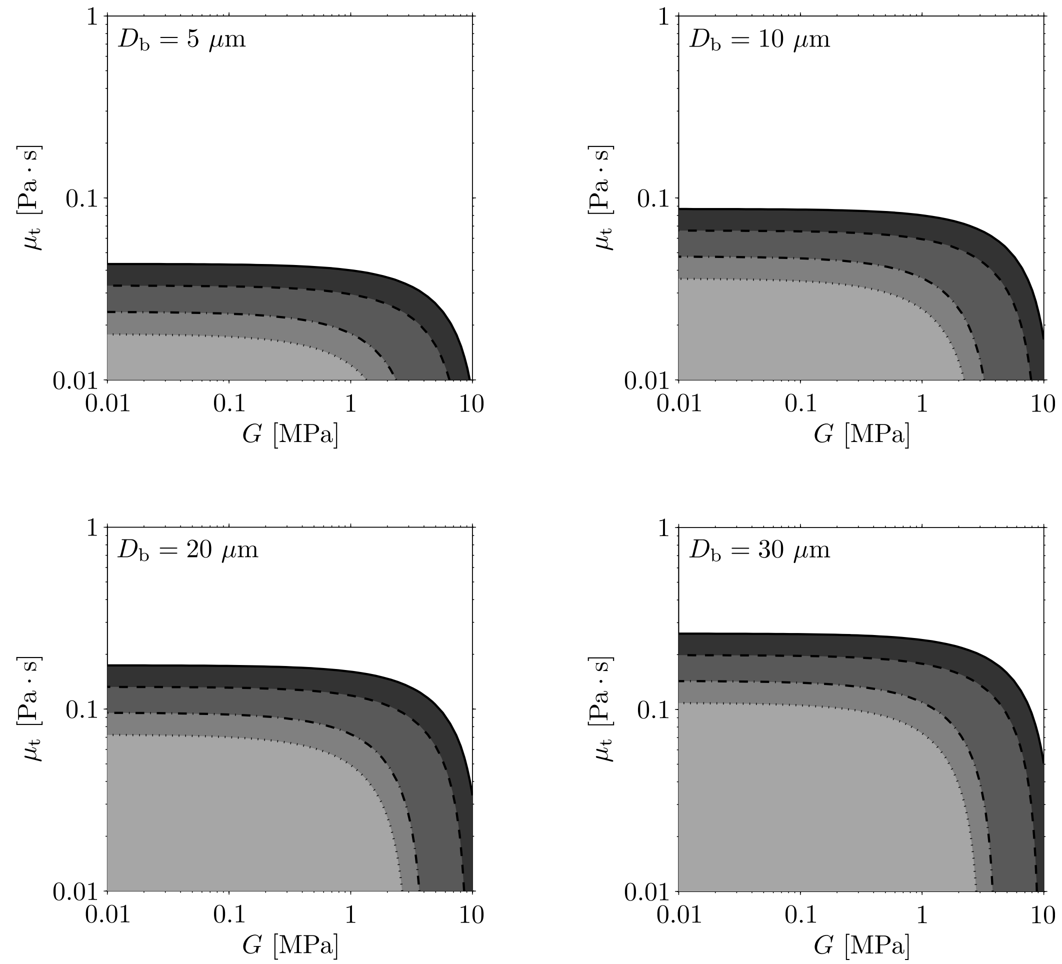

Figure 5.5: Stacked area plot of the regions in the space spanned by the tissue viscosity, μ_t, and elasticity, G, in which the maximum proximal injury layer thickness, $h_{p,\max}$, predicted by the shock-induced, free-field, bubble collapse model, is not expected to exceed 5% error relative to the case in which tissue viscoelasticity is not neglected. Regions are shown for initial bubble diameters, D_b, of 5, 10, 20 and 30 μm, and at shockwave pressures, P_s, and ultimate von Mises strains, $E_{vm,u}$, of 30 MPa and 0.20 (−·−, ■), 30 MPa and 0.55 (·····, ■), 110 MPa and 0.20 (—, ■), and 110 MPa and 0.55 (−−, ■).

relative error in the maximum thickness of the injury layer obtained in the spherical collapse between solutions with and without tissue confinement, which are compared at the collapse time of the latter. These results are shown in Figure 5.5, where error plots have been produced for initial bubble diameters, D_b, of 5, 10, 20, and 30 μm. In each case, regions with 5% or less relative error have been drawn for shockwave pressures, P_s, of 30 and 110 MPa, and ultimate von Mises strains, $E_{vm,u}$, of 0.20 and 0.55. The results for a 1 μm bubble are omitted, however, since the relative error in this case exceeds 10% even for the smallest estimates of tissue viscosity and elasticity. The latter further supports the conclusion of Section 5.5.2 which found such small bubbles to be harmless in the free-field case, since any added viscosity or elasticity will further suppress the potential for injury. For the bubble diameters that are plotted, the relative errors are typically less than 5% for tissue viscosities, μ_{t}, in the range of ultrasound measurements, $\mathcal{O}(10^{-2})$, and nearly the entire range of estimated tissue elasticities, G, up to $\mathcal{O}(1)$. The large role that viscosity plays in suppressing injury is consistent with the scaling analysis of Section 2.1.4, as well all as the findings of Freund [41] from the study of bubble expansion in tissue. Finally, the range of viscosities and elasticities across which the error is less than 5% increases as a function of increasing bubble diameter and pressure, but decreases with increasing ultimate strain. The former trend is the result of the increased role that inertia plays for larger bubbles and stronger shockwaves, while the latter occurs because the von Mises strain in the spherical bubble dynamics model has a power-law-like distribution and the larger strains near the surface of the bubble experience greater suppression for the same value of viscosity and elasticity than deformations further away from the bubble do.

5.5.4 Smallest injurious bubbles as a function of tissue viscosity

The spherical bubble dynamics model is now utilized to adjust as a function of tissue viscosity the estimates of the smallest injurious bubbles obtained in Section 5.5.2 from free-field simulations. Tissue elasticity, on the other hand, is neglected based on the findings in Section 5.5.3 which indicate that it is largely unsuccessful at suppressing the growth of the injury layer. The procedure to adjust the free-field simulation results is iterative and requires that for a given tissue viscosity the spherical bubble dynamics model be solved for increasingly larger bubbles, starting from an estimate of the smallest injurious bubble in the free-field case, until such a bubble size is found that the added tissue viscosity is no longer able to suppress injury. More precisely, the procedure is said to have converged on the adjusted estimate of the smallest injurious bubble if the latter is also found to be injurious in free-field simulations, in Section 5.5.2, and the relative error in its maximum injury layer thickness, computed as in Section 5.5.3, is not sufficiently large to alter that conclusion. The former condition is trivially satisfied, of course, since in free-field simulations a bubble that is larger than the smallest

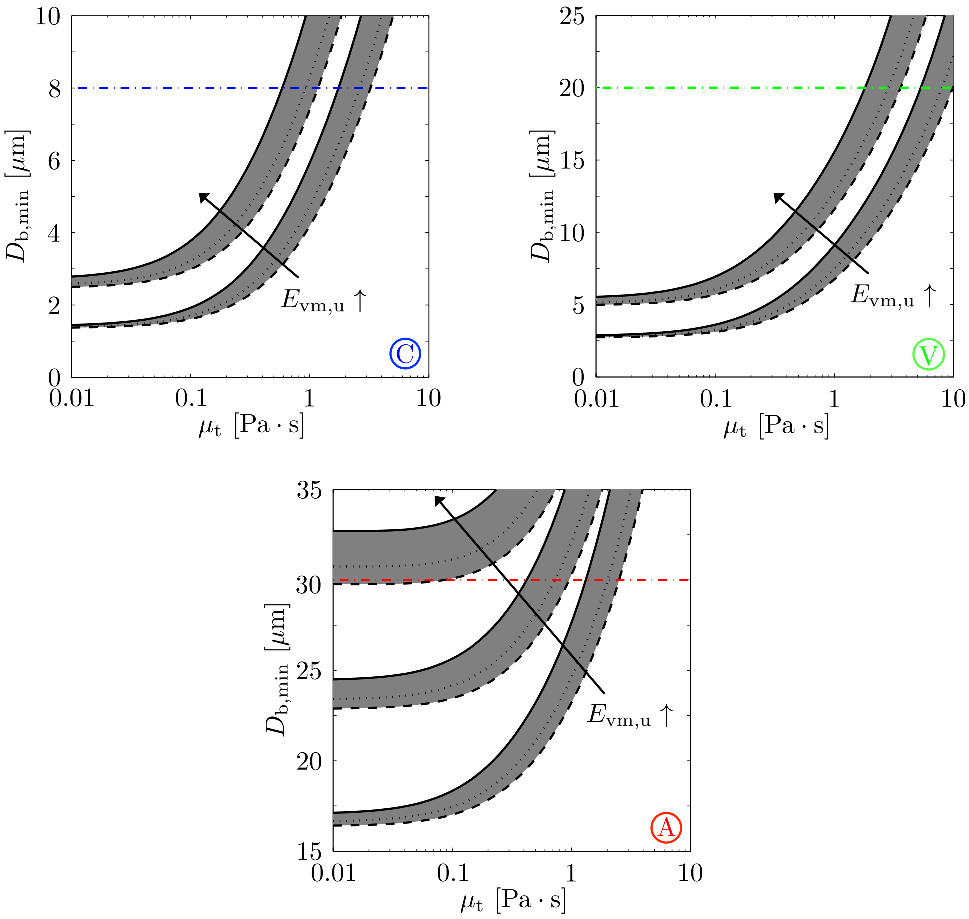

Figure 5.6: Minimum initial bubble diameters, $D_{\mathrm{b,min}}$, needed for the rupture of capillaries (C), venules (V) and arterioles (A) during the collapse phase, as predicted by the shock-induced, free-field, bubble collapse model and subsequently adjusted for the estimated error resulting from neglecting tissue viscosity, μ_{t}. The gray regions correspond to ultimate von Mises strains, $E_{\mathrm{vm,u}}$, of 0.20 and 0.55 in the left and center panels, and 0.20, 0.35 and 0.55 in the right panel. Each region is spanned by shockwave pressure, P_{s}, of 30 (—), 70 (·····) and 110 MPa (−−). The average lumen diameter of each vessel is indicated by a dash-dotted line.

one required for vascular rupture is inherently also injurious.

The adjusted estimates of the smallest injurious bubbles are now presented in Figure 5.6, where the minimum bubble diameter, $D_{\mathrm{b,min}}$, that is needed to rupture capillaries, venules and arterioles is plotted against the tissue viscosity, μ_{t}. In each case, gray regions are drawn for ultimate von Mises strains in tissue, $E_{\mathrm{vm,u}}$, of 0.20 and 0.55, with the exception of arterioles where the result for $E_{\mathrm{vm,u}}$ = 0.35 is also included. As in Figure 5.4, each of the regions is spanned by the smallest and largest shockwave pressure considered, P_{s} = 30 and 110 MPa. Moreover, a line denoting the average lumen diameter of each vessel is also shown. An interesting observation from Figure 5.6 is the existence of a threshold viscosity, within the range of those expected in tissue, beyond which the minimum bubble diameter required for vascular rupture can no longer fit inside the average lumen diameter of the vessel. Resultantly, in the most rupture-prone case, *i.e.* $P_{\mathrm{s}} = 110$ MPa and $E_{\mathrm{vm,u}} = 0.20$, injury seems improbable above $\mu_{\mathrm{t}} = 3.24$ Pa·s, while for venules and arterioles, the same is true beyond $\mu_{\mathrm{t}} = 9.89$ and 2.52 Pa·s, respectively. For much smaller estimates of tissue viscosity, on the other hand, $\mathcal{O}(10^{-2})$ Pa·s, the minimum injurious bubble diameters readily fit inside the vessels and in fact, are not significantly larger than those estimated in free-field simulations, in Section 5.5.2. The latter is not unexpected, however, based on the results of Section 5.5.3, which show the maximum injury layer thickness in spherical collapse to be relatively unaffected by tissue viscosities of $\mathcal{O}(10^{-2})$ Pa·s when compared to the inviscid case. Lastly, the trends in the minimum bubble diameter as a function of shockwave pressure and ultimate strain are the same here as observed in Figure 5.5, and thus no further discussed.

5.6 Estimates of the smallest injurious bubbles in the jetting phase

5.6.1 Propagation of an inviscid fluid sphere in a viscous fluid

In Section 2.1.4, the omission of a viscous and elastic tissue model was motivated by a scaling analysis which suggests that during the early times of shock-induced collapse inertia is expected to play the dominant role across a large range of estimated values of tissue viscoelasticity. At later times, however, the propagation of the bubble jet is expected to be suppressed by tissue, which cannot be predicted by a free-field collapse model. Then, to estimate injurious bubble sizes in the jetting phase, the jet propagation model of Freund *et al.* [43] is utilized. The model is a time-dependent solution of the propagation of an inviscid fluid sphere in a quiescent viscous flow, in the Stokes' limit, and is shown to provide conservative estimates of the propagation distance of the jet when compared to results of axisymmetric simulations of jetting into a planar viscous fluid layer [43]. Once more, tissue elasticity is neglected, since viscosity can be expected to play a much larger

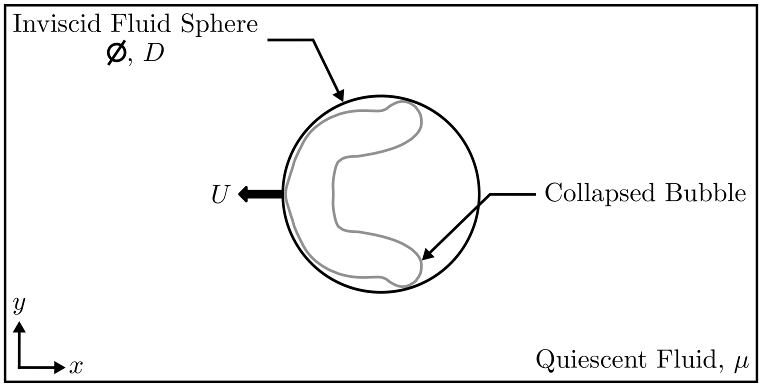

Figure 5.7: Schematic of the model of Freund *et al.* [43] in Equation (5.16) for the propagation of an inviscid fluid sphere in a quiescent viscous fluid, shown here in the x-y cross section of a 3D domain. The schematic depicts how the model is adapted to describe the propagation of a bubble jetting into tissue.

role in suppressing the dynamics of the bubble, see Sections 2.1.4 and 5.5.3. The model of Freund *et al.* is given by

$$d(t) = U\frac{\rho D^2}{12\mu}\left[1 - \exp\left(-\frac{12\mu}{\rho D^2}t\right)\right] \tag{5.16}$$

and illustrated in the schematic of Figure 5.7. In Equation (5.16), d is the propagation distance, U and D are the initial velocity and fixed diameter of the inviscid sphere, respectively, and ρ and μ are the density and viscosity of the surrounding fluid. To predict the propagation of the jet, the model is typically fitted with the size of the bubble and material interface velocity at the time the jet first interacts with it. However, in the present case, it is fitted with the minimum bubble size achieved during collapse and the growth velocity of the distal injury layer at early times of the jetting phase in order to predict the distal injury layer thickness. This choice of bubble size will lead to estimates that are more conservative than those of Freund *et al.*, while the choice of utilizing the growth velocity of the distal injury layer is justified by the fact that the latter is approximately proportional to that of the material interface velocity, as evidenced by Figures 5.3 and 4.6.

5.6.2 Smallest injurious bubbles as a function of tissue viscosity

In Figure 5.8, the smallest injurious bubble diameters estimated from fitting the jet penetration

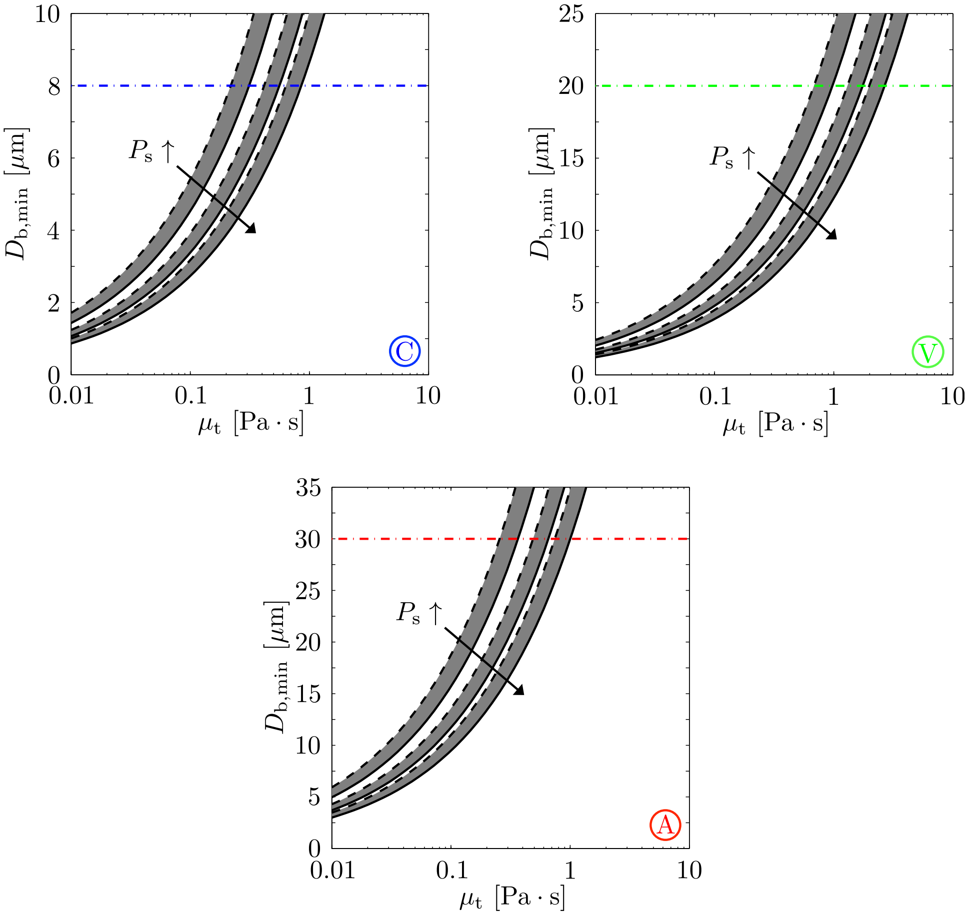

Figure 5.8: Minimum initial bubble diameter, $D_{\mathrm{b,min}}$, needed for the rupture of capillaries (C), venules (V) and arterioles (A) during the jetting phase as a function of tissue viscosity, μ_{t}, and as predicted by fitting the jetting model of Freund *et al.* [43]. The gray regions correspond to shockwave pressures, P_{s}, of 30, 70 and 110 MPa. Each region is spanned by ultimate von Mises strains, $E_{\mathrm{vm,u}}$, of 0.20 (—) and 0.55 (−−). The average lumen diameter of each vessel is indicated by a dash-dotted line.

model of Freund *et al.* [43], Equation (5.16), with the free-field simulations are shown for capillaries, venules and arterioles. In each case, gray regions spanned by ultimate von Mises strains in tissue, $E_{\mathrm{vm,u}}$, of 0.20 and 0.55 are plotted for shockwave pressures, P_{s}, of 30, 70 and 110 MPa. For reference, a line denoting the average lumen diameter of each vessel is also shown. The results for jetting are similar to those obtained for the collapse phase, Section 5.5.2. Notably, it can once again be concluded that bubbles smaller than approximately 1 μm are unlikely to rupture the microvasculature. This result is significant because it suggests that the shock-induced collapse of bubbles present under normal physiological conditions cannot result in vascular rupture – in agreement with how injury is thought to develop in SWL, see Section 2.1.1. Furthermore, just as in the collapse phase, a threshold viscosity within the range of those expected in tissue also exists in the jetting phase, such that for values beyond it, the minimum bubble diameter required for vascular rupture can no longer fit inside the average lumen size of the vessel. It is interesting to note, however, that the threshold values in the jetting phase are typically lower than those in the collapse phase. For comparison, for the most rupture-prone configuration, *i.e.* $P_{\mathrm{s}} = 110$ MPa and $E_{\mathrm{vm,u}} = 0.20$, these are given here by $\mu_{\mathrm{t}} = 0.86$, 2.68 and 1.00 Pa·s, for capillaries, venules and arterioles, respectively. In all likelihood, these lower values are the product of the finer spatial scales introduced during the jetting phase, which enhance viscous effects.

5.7 Summary

In this chapter, a method to extract finite strain fluid deformations from simulations of shock-induced bubble collapse in the free-field was introduced and a criterion was developed to consistently correlate the resulting strains to ultimate strains of tissue from uniaxial loading experiments in order to predict vascular rupture. The vascular rupture criterion was subsequently utilized to estimate the smallest injurious bubbles for the collapse and jetting mechanisms. For both mechanisms, the free-field simulation results indicated that the smallest injurious bubbles would lie in the range expected in the microvasculature, $1 \leq D_{\mathrm{b}} \leq 30$ μm. The finding was nearly independent of the type of microvessel, clinical SWL pressure amplitude or ultimate strain considered. Large estimates of tissue viscosity, on the other hand, which were accounted for *ex posto facto* using a spherical bubble dynamics model and a jet propagation model in the collapse and jetting phases, respectively, were shown to be able to suppress vascular injury for any bubble size. In particular, for the collapse mechanism, vascular injury in capillaries, venules and arterioles could be suppressed entirely for estimates of tissue viscosity larger than $\mu_{\mathrm{t}} = 3.24$, 9.89 and 2.52 Pa·s, respectively, while for the jetting mechanism, the latter was the case for $\mu_{\mathrm{t}} = 0.86$, 2.68 and 1.00 Pa·s.

Chapter 6

Concluding remarks

6.1 Summary and conclusions

In the present work, idealized problems consisting of the shock-induced collapse of a bubble in the free-field and inside a vessel phantom were studied in order to characterize the coupled dynamics between the bubble, vessel and shockwave, and to correlate these dynamics to vascular damage potential in SWL. Both problems were modeled in the scope of viscous and compressible multicomponent flows and a quasi-conservative, high-order accurate, shock- and interface-capturing numerical method was developed to evolve the governing equations. In the case of the shock-induced collapse in a free-field, numerical simulations were carried out across a parameter space spanned by the range of shockwave pressure amplitudes characteristic of clinical SWL applications. A single pressure from that range, on the other hand, was chosen for the numerical simulations of bubble collapse in a vessel phantom, where additional parameters, including vessel confinement, vessel proximity, shockwave angle and tissue viscosity, were considered. Correlations to vascular damage potential were subsequently carried out by comparing the measured finite strain fluid deformations in the free-field, and the vessel wall pressures and displacement in the phantom, to available measurements in tissue.

In the vessel phantom, the largest pressures and displacements were measured in the case of the most restrictive vascular confinement considered. In particular, the pressures were nearly an order of magnitude larger than the amplitude of the initial shockwave during the jetting phase, on the distal vessel wall, while the magnitude of the displacements was nearly half of the initial vessel radius during both the collapse and jetting phases, on the proximal and distal vessel walls, respectively. Both the pressures and displacements dropped off quickly, however, as the vascular confinement was released, with the decrease of the maximum distal and proximal vessel wall pressures during the jetting phase obeying a power law model and the analogous displacements during the collapse phase obeying a sink flow model. For a fixed vessel confinement, on the other hand, nearly the same behavior could also be observed in the study of the effects of bubble proximity, when the bubble was moved farther away from the vessel walls, whereas the effects of shockwave angle had a nearly negligible impact on the maximum vessel wall displacement during the collapse phase, but significantly reduced both the maximum vessel wall pressure and displacement during the jetting phase, when the jet was made to propagate perpendicularly to the nearest vessel wall rather than toward it. Finally, in the study of the effects of tissue viscosity, the estimates from ultrasound measurements were shown to be able to reduce the vessel wall displacements, but had a negligible impact on the vessel wall pressures, ultimately suggesting that the latter may not be a reliable metric for estimating vascular damage potential.

A more detailed analysis of the deformations induced by the collapse of the bubble was subsequently carried out in the free-field by developing a method to post-process the time-dependent, 3D, finite strain fluid deformations in the neighborhood of the bubble. Moreover, a vascular rupture criterion based on the von Mises strain was proposed to determine the size of injurious bubbles in capillaries, venules and arterioles. Bubble sizes present under normal physiological conditions, *i.e.* prior to treatment, were shown to be unlikely to result in the rupture of any microvessel, even at the largest clinical SWL pressure tested. In the range of sizes available during treatment, however, bubbles capable of vascular rupture were expected to exist for the entire microvasculature, with both the collapse and jetting mechanisms involved. In the collapse phase, the errors in the predicted injurious bubble sizes were quantified as a function of tissue viscoelasticity utilizing a spherical bubble dynamics model. The adjusted bubble sizes showed that beyond a certain threshold tissue viscosity, specific to each vessel, rupture could be prevented. The same was the case in the jetting phase, where a jet penetration model was utilized to predict the size of the injurious bubbles as a function of tissue viscosity.

In conclusion, the present work constitutes a significant advance in the state of practice for the study of shocked-bubble dynamics in tissue. Indeed, asymmetric simulations of the shock-induced collapse of a bubble in a vessel phantom have previously never been reported in literature. The simulated parameter space is thus inherently the most exhaustive to date and the resulting trends in vessel wall pressures and displacements as a function of the problem geometry and vessel phantom viscosity are the first of their kind. The state of practice of this problem was also furthered by the development of a numerical method for extracting finite strain fluid deformations, which enabled a previously difficult to establish link between the flow quantities in fluid simulations and the mechanical failure of tissue. This method, which was applied to simulations of shock-induced bubble collapse in the free-field, resulted in the first reported estimates of the smallest injurious bubbles in the microvasculature. These estimates are potentially significant, as they may prove to be a useful metric in testing predictions from simulations with corresponding experiments where small spatial and fast temporal scales of shock-induced collapse make it challenging to measure other quantities, such as pressures and deformations.

6.2 Suggestions for future work

The focus of the present study has been the dynamics of shock-induced collapse. However, the latter only represent a small part of the rich spectrum of bubble dynamics that can be expected in SWL. Shocked-bubble expansion, bubble splitting and cloud cavitation will undoubtedly all play nontrivial roles in vascular injury and should be investigated. In particular, understanding how these dynamics might evolve from a single preexisting nucleus, as a function of the repeated passage of a lithotripter pulse, would be essential to understanding how injury develops in microvessels. To that end, a numerical scheme that can handle both slow and fast time scales, as well as small and large spatial scales, needs to be developed, with additional physics, such as phase change, mass transfer and heat transfer, modeled in the governing equations.

Lastly, beyond estimating the effects of tissue viscoelasticity through the spherical bubble dynamics and jet penetration models, free-field simulations of shock-induced collapse in a viscoelastic fluid should be considered. Such simulations, when carried out across the parameter space spanned by the measurements of tissue viscosity and elasticity, could help establish lower bounds for the estimates of the smallest injurious bubble sizes in the microvasculature. To begin, a simple constitutive model, such as the Oldroyd-B model, for example, which describes a fluid consisting of elastic beads and spring dumbbells, could be coupled to the present governing equations.

Appendix A

State variables, fluxes and source terms

The vectors of state variables, $\mathbf{q}$:

$$\mathbf{q} = \left(\alpha_1\rho_1, \alpha_2\rho_2, \rho u, \rho v, \rho w, E, \alpha_1\right)^{\mathrm{T}}, \tag{A.1}$$

advective fluxes, $\mathbf{f}^{\mathrm{a}}$, $\mathbf{g}^{\mathrm{a}}$ and $\mathbf{h}^{\mathrm{a}}$:

$$\left.\begin{aligned}
\mathbf{f}^{\mathrm{a}} &= \left(\alpha_1\rho_1 u, \alpha_2\rho_2 u, \rho u^2 + p, \rho v u, \rho w u, (E+p)u, \alpha_1 u\right)^{\mathrm{T}}, \\
\mathbf{g}^{\mathrm{a}} &= \left(\alpha_1\rho_1 v, \alpha_2\rho_2 v, \rho u v, \rho v^2 + p, \rho w v, (E+p)v, \alpha_1 v\right)^{\mathrm{T}}, \\
\mathbf{h}^{\mathrm{a}} &= \left(\alpha_1\rho_1 w, \alpha_2\rho_2 w, \rho u w, \rho v w, \rho w^2 + p, (E+p)w, \alpha_1 w\right)^{\mathrm{T}},
\end{aligned}\right\} \tag{A.2}$$

diffusive fluxes, $\mathbf{f}^{\mathrm{d}}$, $\mathbf{g}^{\mathrm{d}}$ and $\mathbf{h}^{\mathrm{d}}$:

$$\left.\begin{aligned}
\mathbf{f}^{\mathrm{d}} &= \left(0, 0, \tau_{xx}, \tau_{xy}, \tau_{xz}, \tau_{xx}u + \tau_{xy}v + \tau_{xz}w, 0\right)^{\mathrm{T}}, \\
\mathbf{g}^{\mathrm{d}} &= \left(0, 0, \tau_{yx}, \tau_{yy}, \tau_{yz}\tau_{yx}u + \tau_{yy}v + \tau_{yz}w, 0\right)^{\mathrm{T}}, \\
\mathbf{h}^{\mathrm{d}} &= \left(0, 0, \tau_{zx}, \tau_{zy}, \tau_{zz}, \tau_{zx}u + \tau_{zy}v + \tau_{zz}w, 0\right)^{\mathrm{T}},
\end{aligned}\right\} \tag{A.3}$$

and source terms, $\mathbf{s}$:

$$\mathbf{s} = \left(0, 0, 0, 0, 0, 0, \alpha_1 \nabla \cdot \mathbf{u}\right)^{\mathrm{T}}, \tag{A.4}$$

of the conservation-law form of the five-equation model, Equation (3.1), where τ is an element of the viscous stress tensor, Equation (2.6).

Appendix B

Characteristic decomposition

To illustrate the projection of the primitive variables onto the characteristic fields, we begin by rewriting the conservation-law form of the equations of motion, Equation (3.1), in its equivalent quasi-linear form and as a function of the primitive variables. In the process, we neglect the viscous terms, as they will not impact the sought-after result, and once again consider the advection equation for the volume fraction in its original form, see Equation (2.5). Equation (3.1) then becomes

$$\frac{\partial \mathbf{v}}{\partial t} + \mathbf{A}(\mathbf{v})\frac{\partial \mathbf{v}}{\partial x} + \mathbf{B}(\mathbf{v})\frac{\partial \mathbf{v}}{\partial y} + \mathbf{C}(\mathbf{v})\frac{\partial \mathbf{v}}{\partial z} = \mathbf{0}, \tag{B.1}$$

where $\mathbf{v}$ is the vector of primitive variables and $\mathbf{A} = \partial_{\mathbf{v}}\mathbf{f}^{\mathrm{a}}$, $\mathbf{B} = \partial_{\mathbf{v}}\mathbf{g}^{\mathrm{a}}$ and $\mathbf{C} = \partial_{\mathbf{v}}\mathbf{h}^{\mathrm{a}}$ are Jacobian matrices. The individual components of these vector and matrix variables are given by

$$\mathbf{v} = \begin{pmatrix} \alpha_1\rho_1 \\ \alpha_2\rho_2 \\ u \\ v \\ w \\ p \\ \alpha_1 \end{pmatrix}, \mathbf{A} = \begin{pmatrix} u & 0 & \alpha_1\rho_1 & 0 & 0 & 0 & 0 \\ 0 & u & \alpha_2\rho_2 & 0 & 0 & 0 & 0 \\ 0 & 0 & u & 0 & 0 & \rho^{-1} & 0 \\ 0 & 0 & 0 & u & 0 & 0 & 0 \\ 0 & 0 & 0 & 0 & u & 0 & 0 \\ 0 & 0 & \rho c^2 & 0 & 0 & u & 0 \\ 0 & 0 & 0 & 0 & 0 & 0 & u \end{pmatrix}, \tag{B.2a}$$

$$\mathbf{B} = \begin{pmatrix} v & 0 & 0 & \alpha_1\rho_1 & 0 & 0 & 0 \\ 0 & v & 0 & \alpha_2\rho_2 & 0 & 0 & 0 \\ 0 & 0 & v & 0 & 0 & 0 & 0 \\ 0 & 0 & 0 & v & 0 & \rho^{-1} & 0 \\ 0 & 0 & 0 & 0 & v & 0 & 0 \\ 0 & 0 & 0 & \rho c^2 & 0 & v & 0 \\ 0 & 0 & 0 & 0 & 0 & 0 & v \end{pmatrix}, \mathbf{C} = \begin{pmatrix} w & 0 & 0 & 0 & \alpha_1\rho_1 & 0 & 0 \\ 0 & w & 0 & 0 & \alpha_2\rho_2 & 0 & 0 \\ 0 & 0 & w & 0 & 0 & 0 & 0 \\ 0 & 0 & 0 & w & 0 & 0 & 0 \\ 0 & 0 & 0 & 0 & w & \rho^{-1} & 0 \\ 0 & 0 & 0 & 0 & \rho c^2 & w & 0 \\ 0 & 0 & 0 & 0 & 0 & 0 & w \end{pmatrix}. \tag{B.2b}$$

Now in order to obtain the characteristic variables from the primitive ones, Equation (B.1) must be decomposed along its characteristics. However, since the characteristic decomposition is only applied in one coordinate direction at a time, we illustrate the procedure for the x-direction with the understanding that the procedure for the remaining coordinate directions is entirely analogous. We begin by solving the eigenvalue decomposition problem for $\mathbf{A}$:

$$\mathbf{A} = \mathbf{Q}_\mathrm{A}\mathbf{\Lambda}_\mathrm{A}\mathbf{Q}_\mathrm{A}^{-1}, \tag{B.3}$$

where $\mathbf{Q}_\mathrm{A}$ is a matrix whose columns are the right eigenvectors of $\mathbf{A}$ and $\mathbf{\Lambda}_\mathrm{A}$ is a matrix whose diagonal elements are the corresponding eigenvalues:

$$\mathbf{Q}_\mathrm{A} = \begin{pmatrix} -\frac{\alpha_1\rho_1}{2c} & 1 & 0 & 0 & 0 & 0 & \frac{\alpha_1\rho_1}{2c} \\ -\frac{\alpha_2\rho_2}{2c} & 0 & 1 & 0 & 0 & 0 & \frac{\alpha_2\rho_2}{2c} \\ \frac{1}{2} & 0 & 0 & 0 & 0 & 0 & \frac{1}{2} \\ 0 & 0 & 0 & 1 & 0 & 0 & 0 \\ 0 & 0 & 0 & 0 & 1 & 0 & 0 \\ -\frac{\rho c}{2} & 0 & 0 & 0 & 0 & 0 & \frac{\rho c}{2} \\ 0 & 0 & 0 & 0 & 0 & 1 & 0 \end{pmatrix}, \mathbf{\Lambda}_\mathrm{A} = \begin{pmatrix} u-c & 0 & 0 & 0 & 0 & 0 & 0 \\ 0 & u & 0 & 0 & 0 & 0 & 0 \\ 0 & 0 & u & 0 & 0 & 0 & 0 \\ 0 & 0 & 0 & u & 0 & 0 & 0 \\ 0 & 0 & 0 & 0 & u & 0 & 0 \\ 0 & 0 & 0 & 0 & 0 & u & 0 \\ 0 & 0 & 0 & 0 & 0 & 0 & u+c \end{pmatrix}. \tag{B.4}$$

Then, by assuming that $\mathbf{Q}_\mathrm{A}$ is spatially and temporally frozen, the variable transformation $\mathbf{v} = \mathbf{Q}_\mathrm{A}\mathbf{w}_\mathrm{A}$, along with Equation (B.3), can be substituted into Equation (B.1) to yield the dimensionally split characteristic equation for the x-direction:

$$\frac{\partial \mathbf{w}_\mathrm{A}}{\partial t} + \mathbf{\Lambda}_\mathrm{A}\frac{\partial \mathbf{w}_\mathrm{A}}{\partial x} = \mathbf{0}, \tag{B.5}$$

where $\mathbf{w}_\mathrm{A}$ is the vector of characteristic variables obtained from the projection of the primitive variables onto the characteristic fields in the x-direction:

$$\mathbf{w}_\mathrm{A} = \mathbf{Q}_\mathrm{A}^{-1}\mathbf{v}. \tag{B.6}$$

The variable transformation in Equation (B.6) may now be utilized to convert the cell average primitive variables into the cell average characteristic variables so that the latter may be reconstructed. However, since Equation (B.6) was obtained based on a characteristic decomposition in the x-direction, the reconstruction of the resulting characteristic variables must be carried out on cell faces normal to that direction. Then, applying Equation (B.6) to the cell average primitive variables in a given cell, we get

$$\mathbf{w}_{\mathrm{A}_{i,j,k}} = \mathbf{Q}_{\mathrm{A}_{i+1/2,j,k}}^{-1}\mathbf{v}_{i,j,k}, \tag{B.7}$$

where the frozen projection matrix, $\mathbf{Q}_\mathrm{A}^{-1}$, is to be evaluated at state $\mathbf{v}_{i+1/2,j,k}$. However, the latter is not known prior to reconstruction, so that typically a Roe or arithmetic average of $\mathbf{v}_{i,j,k}$ and $\mathbf{v}_{i+1,j,k}$ is utilized instead. We prefer computing the arithmetic average, as it is less computationally expensive than, and performs equally well in our tests as, the Roe average. Once the characteristic variables have been reconstructed at the Gaussian quadrature points of both the left and right side of the cell faces normal to the x-direction, the primitive variables may be recovered by projecting the characteristic variables back onto the physical fields:

$$\left.\begin{aligned}\mathbf{v}^{\mathrm{L}}_{i+1/2,j_l,k_m} &= \mathbf{Q}_{\mathrm{A}_{i+1/2,j,k}}\mathbf{w}^{\mathrm{L}}_{\mathrm{A}_{i+1/2,j_l,k_m}},\\ \mathbf{v}^{\mathrm{R}}_{i+1/2,j_l,k_m} &= \mathbf{Q}_{\mathrm{A}_{i+1/2,j,k}}\mathbf{w}^{\mathrm{R}}_{\mathrm{A}_{i+1/2,j_l,k_m}}.\end{aligned}\right\} \tag{B.8}$$

The procedure described by Equations (B.7) and (B.8) does not affect the formal order of the spatial accuracy of the numerical method and has readily been utilized in the past with high-order methods for conservation laws, see [54, 64, 92, 110] to name but a few.

Appendix C

WENO reconstruction

Our WENO scheme is primarily a generalization of the original fifth-order method of Liu *et al.* [80] to nonuniform grids. To our knowledge, the building blocks of such a scheme, *i.e.* the polynomials, weights, and smoothness indicators, have only been reported in literature once before and in a limited capacity. Specifically, Johnsen [63] provided them for a reconstruction at the cell boundaries, but not at the quadrature points. In this section, we thus briefly overview the procedure by which the generalized WENO building blocks of an arbitrarily high-order reconstruction at a given point may be obtained and document those for a fifth-order reconstruction, at both the cell boundaries and quadrature points.

Following the notes of Shu [99], a $(2k-1)^{\text{th}}$-order WENO reconstruction in cell I_i consists of the convex combination of k polynomials of k^{th}-order, which are defined on candidate stencils

$$S_r(i) = \left\{ x_{i-r}, ..., x_{i-r+k-1} \right\}, \quad r = 0, ..., k-1. \tag{C.1}$$

The Lagrange form of each polynomial is given by

$$f^{(r)}(x) = \sum_{m=0}^{k} \sum_{j=0}^{m-1} f_{i-r+j} \Delta x_{i-r+j} \left(\frac{\sum\limits_{\substack{l=0 \\ l \neq m}}^{k} \prod\limits_{\substack{q=0 \\ q \neq m,l}}^{k} \left(x - x_{i-r+q-1/2} \right)}{\prod\limits_{\substack{l=0 \\ l \neq m}}^{k} \left(x_{i-r+m-1/2} - x_{i-r+l-1/2} \right)} \right), \tag{C.2}$$

where f is an arbitrary function whose pointwise approximation is to be obtained in cell I_i from its cell averages in the candidate stencils. Without any loss in the generality of the methodology, we can then write the convex combination of the candidate polynomials for a reconstruction at the right cell boundary of cell I_i, $x_{i+1/2}$, as follows:

$$f_{i+1/2} = \sum_{r=0}^{k-1} \omega_{i+1/2}^{(r)} f_{i+1/2}^{(r)} = f\left(x_{i+1/2}\right) + \mathcal{O}\left(\Delta x_i^{2k-1}\right), \tag{C.3}$$

where the nonlinear weights, ω, satisfy

$$\omega_{i+1/2}^{(r)} \geq 0, \quad \sum_{r=0}^{k-1} \omega_{i+1/2}^{(r)} = 1, \tag{C.4}$$

for stability and consistency, and are specially designed to achieve a $(2k-1)^{\text{th}}$-order reconstruction in smooth regions of f and an essentially non-oscillatory one in regions containing discontinuities.

The nonlinear weights depend on both the cell size distribution and the smoothness of the interpolated function. They are derived from the so-called ideal weights, d, which are only a function of the former and for which the relationships in Equations (C.3) and (C.4) also hold, *i.e.*

$$f_{i+1/2} = \sum_{r=0}^{k-1} d_{i+1/2}^{(r)} f_{i+1/2}^{(r)} = f\left(x_{i+1/2}\right) + \mathcal{O}\left(\Delta x_i^{2k-1}\right) \tag{C.5}$$

and

$$d_{i+1/2}^{(r)} \geq 0, \quad \sum_{r=0}^{k-1} d_{i+1/2}^{(r)} = 1. \tag{C.6}$$

The ideal weights are obtained by matching the coefficients of the convex combination of the k^{th}-order polynomials with those of a $(2k-1)^{\text{th}}$-order polynomial generated by Equation (C.2) and centered about cell I_i. Though the ideal weights also achieve a $(2k-1)^{\text{th}}$-order reconstruction in smooth regions of f, they produce oscillatory behavior for reconstructions in regions containing discontinuities.

The nonlinear weights are derived from the ideal weights by taking into account the smoothness of f. The latter is characterized by the smoothness indicators of Jiang and Shu [62], β:

$$\beta^{(r)} = \sum_{l=1}^{k-1} \int_{x_{i-1/2}}^{x_{i+1/2}} \Delta x_i^{2l-1} \left(\frac{\mathrm{d}^l f^{(r)}(x)}{\mathrm{d}^l x} \right)^2 \, \mathrm{d}x, \tag{C.7}$$

which are utilized to first rescale the ideal weights:

$$\alpha_{i+1/2}^{(r)} = \frac{d_{i+1/2}^{(r)}}{\left(\beta^{(r)} + \epsilon\right)^2}, \tag{C.8}$$

and subsequently normalize them so to obtain the nonlinear ones:

$$\omega_{i+1/2}^{(r)} = \frac{\alpha_{i+1/2}^{(r)}}{\sum\limits_{s=0}^{k-1} \alpha_{i+1/2}^{(s)}}, \tag{C.9}$$

with ϵ a small parameter that is utilized to avoid division by zero. Typically, it is set to 10^{-6} to avoid deteriorating the formal order of accuracy of the reconstruction near critical points of f. In practice, we remove this restriction and set ϵ to machine precision by means of an additional mapping of the nonlinear weights, see Henrick *et al.* [56] for details.

The above-described methodology is analogous for the reconstruction at any other point within cell I_i. In addition, the resulting WENO scheme is no more expensive than one developed on a uniform grid, as all grid-dependent coefficients that appear in the polynomials, weights and smoothness indicators can be computed prior to simulation. Next, we document the building blocks of a fifth-order WENO reconstruction. For conciseness, we utilize the square bracket notation to denote the usual jump in a quantity, *e.g.* $[x]_{i-1/2}^{i+1/2} = x_{i+1/2} - x_{i-1/2}$.

A.1. Polynomials

$x = x_{i+1/2}$

$$\left.\begin{aligned}
f^{(0)}_{i+1/2} &= f_i + \frac{[x]^{i+1/2}_{i-1/2}\left([x]^{i+3/2}_{i-1/2} + [x]^{i+5/2}_{i+1/2}\right)}{[x]^{i+3/2}_{i-1/2}[x]^{i+5/2}_{i-1/2}}[f]^{i+1}_{i} - \frac{[x]^{i+1/2}_{i-1/2}[x]^{i+3/2}_{i+1/2}}{[x]^{i+5/2}_{i-1/2}[x]^{i+5/2}_{i+1/2}}[f]^{i+2}_{i+1} \\
f^{(1)}_{i+1/2} &= f_i + \frac{[x]^{i+1/2}_{i-1/2}[x]^{i+3/2}_{i+1/2}}{[x]^{i+1/2}_{i-3/2}[x]^{i+3/2}_{i-3/2}}[f]^{i}_{i-1} + \frac{[x]^{i+1/2}_{i-3/2}[x]^{i+1/2}_{i-1/2}}{[x]^{i+3/2}_{i-3/2}[x]^{i+3/2}_{i-1/2}}[f]^{i+1}_{i} \\
f^{(2)}_{i+1/2} &= f_i - \frac{[x]^{i+1/2}_{i-3/2}[x]^{i+1/2}_{i-1/2}}{[x]^{i-1/2}_{i-5/2}[x]^{i+1/2}_{i-5/2}}[f]^{i-1}_{i-2} + \frac{[x]^{i+1/2}_{i-1/2}\left([x]^{i+1/2}_{i-5/2} + [x]^{i+1/2}_{i-3/2}\right)}{[x]^{i+1/2}_{i-5/2}[x]^{i+1/2}_{i-3/2}}[f]^{i}_{i-1}
\end{aligned}\right\} \tag{C.10}$$

$x = x_{i-1/2}$

$$\left.\begin{aligned}
f^{(0)}_{i-1/2} &= f_i - \frac{[x]^{i+1/2}_{i-1/2}\left([x]^{i+3/2}_{i-1/2} + [x]^{i+5/2}_{i-1/2}\right)}{[x]^{i+3/2}_{i-1/2}[x]^{i+5/2}_{i-1/2}}[f]^{i+1}_{i} + \frac{[x]^{i+1/2}_{i-1/2}[x]^{i+3/2}_{i-1/2}}{[x]^{i+5/2}_{i-1/2}[x]^{i+5/2}_{i+1/2}}[f]^{i+2}_{i+1} \\
f^{(1)}_{i-1/2} &= f_i - \frac{[x]^{i+1/2}_{i-1/2}[x]^{i+3/2}_{i-1/2}}{[x]^{i+1/2}_{i-3/2}[x]^{i+3/2}_{i-3/2}}[f]^{i}_{i-1} - \frac{[x]^{i-1/2}_{i-3/2}[x]^{i+1/2}_{i-1/2}}{[x]^{i+3/2}_{i-3/2}[x]^{i+3/2}_{i-1/2}}[f]^{i+1}_{i} \\
f^{(2)}_{i-1/2} &= f_i + \frac{[x]^{i-1/2}_{i-3/2}[x]^{i+1/2}_{i-1/2}}{[x]^{i-1/2}_{i-5/2}[x]^{i+1/2}_{i-5/2}}[f]^{i-1}_{i-2} - \frac{[x]^{i+1/2}_{i-1/2}\left([x]^{i-1/2}_{i-5/2} + [x]^{i+1/2}_{i-3/2}\right)}{[x]^{i+1/2}_{i-5/2}[x]^{i+1/2}_{i-3/2}}[f]^{i}_{i-1}
\end{aligned}\right\} \tag{C.11}$$

$x = x_{i+1/(2\sqrt{3})}$

$$\left.\begin{aligned}
f^{(0)}_{i+1/(2\sqrt{3})} &= f_i + \frac{[x]^{i+1/2}_{i-1/2}\left(2[x]^{i+3/2}_{i-1/2} + [x]^{i+5/2}_{i-1/2} + [x]^{i+5/2}_{i+1/2}\right)}{2\sqrt{3}[x]^{i+3/2}_{i-1/2}[x]^{i+5/2}_{i-1/2}}[f]^{i+1}_{i} \\
&\quad - \frac{[x]^{i+1/2}_{i-1/2}\left([x]^{i+3/2}_{i-1/2} + [x]^{i+3/2}_{i+1/2}\right)}{2\sqrt{3}[x]^{i+5/2}_{i-1/2}[x]^{i+5/2}_{i+1/2}}[f]^{i+2}_{i+1} \\
f^{(1)}_{i+1/(2\sqrt{3})} &= f_i + \frac{[x]^{i+1/2}_{i-1/2}\left([x]^{i+3/2}_{i-1/2} + [x]^{i+3/2}_{i+1/2}\right)}{2\sqrt{3}[x]^{i+1/2}_{i-3/2}[x]^{i+3/2}_{i-3/2}}[f]^{i}_{i-1} \\
&\quad + \frac{[x]^{i+1/2}_{i-1/2}\left([x]^{i-1/2}_{i-3/2} + [x]^{i+1/2}_{i-3/2}\right)}{2\sqrt{3}[x]^{i+3/2}_{i-3/2}[x]^{i+3/2}_{i-1/2}}[f]^{i+1}_{i} \\
f^{(2)}_{i+1/(2\sqrt{3})} &= f_i + \frac{[x]^{i+1/2}_{i-1/2}\left([x]^{i-1/2}_{i-5/2} + [x]^{i+1/2}_{i-5/2} + 2[x]^{i+1/2}_{i-3/2}\right)}{2\sqrt{3}[x]^{i+1/2}_{i-5/2}[x]^{i+1/2}_{i-3/2}}[f]^{i}_{i-1} \\
&\quad - \frac{[x]^{i+1/2}_{i-1/2}\left([x]^{i-1/2}_{i-3/2} + [x]^{i+1/2}_{i-3/2}\right)}{2\sqrt{3}[x]^{i-1/2}_{i-5/2}[x]^{i+1/2}_{i-5/2}}[f]^{i-1}_{i-2}
\end{aligned}\right\} \tag{C.12}$$

$x = x_{i-1/(2\sqrt{3})}$

$$\left.\begin{aligned}
f^{(0)}_{i-1/(2\sqrt{3})} &= 2f_i - f^{(0)}_{i+1/(2\sqrt{3})} \\
f^{(1)}_{i-1/(2\sqrt{3})} &= 2f_i - f^{(1)}_{i+1/(2\sqrt{3})} \\
f^{(2)}_{i-1/(2\sqrt{3})} &= 2f_i - f^{(2)}_{i+1/(2\sqrt{3})}
\end{aligned}\right\} \tag{C.13}$$

A.2. Ideal weights

$x = x_{i+1/2}$

$$\left.\begin{aligned}
d^{(0)}_{i+1/2} &= \frac{[x]^{i+1/2}_{i-5/2}[x]^{i+1/2}_{i-3/2}}{[x]^{i+5/2}_{i-5/2}[x]^{i+5/2}_{i-3/2}} \\
d^{(2)}_{i+1/2} &= \frac{[x]^{i+3/2}_{i+1/2}[x]^{i+5/2}_{i+1/2}}{[x]^{i+3/2}_{i-5/2}[x]^{i+5/2}_{i-5/2}}
\end{aligned}\right\} \tag{C.14}$$

$x = x_{i-1/2}$

$$\left.\begin{aligned}
d^{(0)}_{i-1/2} &= \frac{[x]^{i-1/2}_{i-5/2}[x]^{i-1/2}_{i-3/2}}{[x]^{i+5/2}_{i-5/2}[x]^{i+5/2}_{i-3/2}} \\
d^{(2)}_{i-1/2} &= \frac{[x]^{i+3/2}_{i-1/2}[x]^{i+5/2}_{i-1/2}}{[x]^{i+3/2}_{i-5/2}[x]^{i+5/2}_{i-5/2}}
\end{aligned}\right\} \tag{C.15}$$

$x = x_{i+1/(2\sqrt{3})}$

$$\left.\begin{aligned}
d^{(0)}_{i+1/(2\sqrt{3})} = \Big\{ &[x]^{i+1/2}_{i-1/2}\left(\sqrt{3}\left([x]^{i+1/2}_{i-1/2}\right)^2 - 6[x]^{i+1/2}_{i-1/2}\left([x]^{i-1/2}_{i-5/2} + [x]^{i-1/2}_{i-3/2}\right)\right. \\
&\left. - 18[x]^{i-1/2}_{i-5/2}[x]^{i-1/2}_{i-3/2}\right) + 6[x]^{i+3/2}_{i-1/2}\left(6[x]^{i-1/2}_{i-5/2}[x]^{i-1/2}_{i-3/2}\right. \\
&\left. +3[x]^{i+1/2}_{i-1/2}\left([x]^{i-1/2}_{i-5/2} + [x]^{i-1/2}_{i-3/2}\right) + \left([x]^{i+1/2}_{i-1/2}\right)^2\right)\Big\} \\
&\div \left\{18[x]^{i+5/2}_{i-5/2}[x]^{i+5/2}_{i-3/2}\left([x]^{i+3/2}_{i-1/2} + [x]^{i+3/2}_{i+1/2}\right)\right\} \\
d^{(2)}_{i+1/(2\sqrt{3})} = \Big\{ &-18[x]^{i+1/2}_{i-1/2}\left([x]^{i+5/2}_{i+1/2}\left([x]^{i-1/2}_{i-3/2} - [x]^{i+3/2}_{i-1/2}\right) - [x]^{i-1/2}_{i-3/2}[x]^{i+3/2}_{i-1/2}\right) \\
&- \left(6+\sqrt{3}\right)\left([x]^{i+1/2}_{i-1/2}\right)^3 + 36[x]^{i-1/2}_{i-3/2}[x]^{i+3/2}_{i-1/2}[x]^{i+5/2}_{i+1/2} \\
&-6\left([x]^{i+1/2}_{i-1/2}\right)^2\left(2[x]^{i-1/2}_{i-3/2} - 2[x]^{i+3/2}_{i-1/2} + [x]^{i+5/2}_{i+1/2}\right)\Big\} \\
&\div \left\{18[x]^{i+3/2}_{i-5/2}[x]^{i+5/2}_{i-5/2}\left([x]^{i-1/2}_{i-3/2} + [x]^{i+1/2}_{i-3/2}\right)\right\}
\end{aligned}\right\} \tag{C.16}$$

$x = x_{i-1/(2\sqrt{3})}$

$$\left.\begin{aligned}
d^{(0)}_{i-1/(2\sqrt{3})} &= d^{(0)}_{i+1/(2\sqrt{3})} - \frac{\left([x]^{i+1/2}_{i-1/2}\right)^3}{3\sqrt{3}[x]^{i+5/2}_{i-5/2}[x]^{i+5/2}_{i-3/2}\left([x]^{i+3/2}_{i-1/2} + [x]^{i+3/2}_{i+1/2}\right)} \\
d^{(2)}_{i-1/(2\sqrt{3})} &= d^{(2)}_{i+1/(2\sqrt{3})} + \frac{\left([x]^{i+1/2}_{i-1/2}\right)^3}{3\sqrt{3}[x]^{i+3/2}_{i-5/2}[x]^{i+5/2}_{i-5/2}\left([x]^{i-1/2}_{i-3/2} + [x]^{i+1/2}_{i-3/2}\right)}
\end{aligned}\right\} \tag{C.17}$$

A.3. Smoothness indicators

$$\left.\begin{aligned}
\beta^{(0)} = 4\left([x]^{i+1/2}_{i-1/2}\right)^2 \times ... & \\
\Bigg(\frac{10\left([x]^{i+1/2}_{i-1/2}\right)^2 + [x]^{i+1/2}_{i-1/2}\left([x]^{i+3/2}_{i-1/2} + [x]^{i+5/2}_{i+1/2}\right) + \left([x]^{i+3/2}_{i-1/2} + [x]^{i+5/2}_{i+1/2}\right)^2}{\left([x]^{i+3/2}_{i-1/2}[x]^{i+5/2}_{i-1/2}\right)^2}\left([f]^{i+1}_{i}\right)^2 & \\
-\frac{19\left([x]^{i+1/2}_{i-1/2}\right)^2 - [x]^{i+1/2}_{i-1/2}[x]^{i+5/2}_{i+1/2} + 2[x]^{i+3/2}_{i-1/2}\left([x]^{i+3/2}_{i-1/2} + [x]^{i+5/2}_{i+1/2}\right)}{[x]^{i+3/2}_{i-1/2}[x]^{i+5/2}_{i+1/2}\left([x]^{i+5/2}_{i-1/2}\right)^2}[f]^{i+1}_{i}[f]^{i+2}_{i+1} & \\
+\frac{10\left([x]^{i+1/2}_{i-1/2}\right)^2 + [x]^{i+1/2}_{i-1/2}[x]^{i+3/2}_{i+1/2} + \left([x]^{i+3/2}_{i+1/2}\right)^2}{\left([x]^{i+5/2}_{i-1/2}[x]^{i+5/2}_{i+1/2}\right)^2}\left([f]^{i+2}_{i+1}\right)^2\Bigg) & \\
\beta^{(1)} = 4\left([x]^{i+1/2}_{i-1/2}\right)^2 \times ... & \\
\Bigg(-\frac{[x]^{i+1/2}_{i-1/2}\left([x]^{i-1/2}_{i-3/2} + 20[x]^{i+1/2}_{i-1/2}\right) - [x]^{i+3/2}_{i-1/2}\left(2[x]^{i-1/2}_{i-3/2} + [x]^{i+1/2}_{i-1/2}\right)}{[x]^{i+1/2}_{i-3/2}[x]^{i+3/2}_{i-1/2}\left([x]^{i+3/2}_{i-3/2}\right)^2}[f]^{i}_{i-1}[f]^{i+1}_{i} & \\
+\frac{10\left([x]^{i+1/2}_{i-1/2}\right)^2 + [x]^{i+1/2}_{i-1/2}[x]^{i+3/2}_{i+1/2} + \left([x]^{i+3/2}_{i+1/2}\right)^2}{\left([x]^{i+1/2}_{i-3/2}[x]^{i+3/2}_{i-3/2}\right)^2}\left([f]^{i}_{i-1}\right)^2 & \\
+\frac{10\left([x]^{i+1/2}_{i-1/2}\right)^2 + [x]^{i-1/2}_{i-3/2}[x]^{i+1/2}_{i-1/2} + \left([x]^{i-1/2}_{i-3/2}\right)^2}{\left([x]^{i+3/2}_{i-3/2}[x]^{i+3/2}_{i-1/2}\right)^2}\left([f]^{i+1}_{i}\right)^2\Bigg) & \\
\beta^{(2)} = 4\left([x]^{i+1/2}_{i-1/2}\right)^2 \times ... & \\
\Bigg(\frac{12\left([x]^{i+1/2}_{i-1/2}\right)^2 + 3[x]^{i+1/2}_{i-1/2}\left([x]^{i-1/2}_{i-5/2} + [x]^{i-1/2}_{i-3/2}\right) + \left([x]^{i-1/2}_{i-5/2} + [x]^{i-1/2}_{i-3/2}\right)^2}{\left([x]^{i+1/2}_{i-5/2}[x]^{i+1/2}_{i-3/2}\right)^2}\left([f]^{i}_{i-1}\right)^2 & \\
-\frac{19\left([x]^{i+1/2}_{i-1/2}\right)^2 - [x]^{i-1/2}_{i-5/2}[x]^{i+1/2}_{i-1/2} + 2[x]^{i+1/2}_{i-3/2}\left([x]^{i-1/2}_{i-5/2} + [x]^{i+1/2}_{i-3/2}\right)}{[x]^{i-1/2}_{i-5/2}[x]^{i+1/2}_{i-3/2}\left([x]^{i+1/2}_{i-5/2}\right)^2}[f]^{i-1}_{i-2}[f]^{i}_{i-1} & \\
+\frac{10\left([x]^{i+1/2}_{i-1/2}\right)^2 + [x]^{i-1/2}_{i-3/2}[x]^{i+1/2}_{i-1/2} + \left([x]^{i-1/2}_{i-3/2}\right)^2}{\left([x]^{i-1/2}_{i-5/2}[x]^{i+1/2}_{i-5/2}\right)^2}\left([f]^{i-1}_{i-2}\right)^2\Bigg) &
\end{aligned}\right\} \tag{C.18}$$

Appendix D

Numerical flux

The methodology for obtaining the solution to a Riemann problem with the HLLC solver is identical for quadrature points on cell faces normal to the same direction and is analogous between quadrature points on orthogonal cell faces. As a result, to illustrate the solution procedure, we temporarily drop the indicial notation used in the previous sections and consider a Riemann problem in the x-coordinate direction comprised of left and right states, $\mathbf{q}_{\mathrm{L}}$ and $\mathbf{q}_{\mathrm{R}}$, respectively. The advective numerical flux is then given by the HLLC solver as

$$\hat{\mathbf{f}}^{\mathrm{a}} = \frac{1+\operatorname{sgn}(s_*)}{2}\left[\mathbf{f}^{\mathrm{a}}_{\mathrm{L}} + s_-\left(\mathbf{q}_{*\mathrm{L}} - \mathbf{q}_{\mathrm{L}}\right)\right] + \frac{1-\operatorname{sgn}(s_*)}{2}\left[\mathbf{f}^{\mathrm{a}}_{\mathrm{R}} + s_+\left(\mathbf{q}_{*\mathrm{R}} - \mathbf{q}_{\mathrm{R}}\right)\right], \tag{D.1}$$

where the state in the intermediate star region, with K = L or R, is given by

$$\mathbf{q}_{*\mathrm{K}} = \left(\frac{s_{\mathrm{K}} - u_{\mathrm{K}}}{s_{\mathrm{K}} - s_*}\right)\begin{pmatrix} (\alpha_1\rho_1)_{\mathrm{K}} \\ (\alpha_2\rho_2)_{\mathrm{K}} \\ \rho_{\mathrm{K}} s_* \\ \rho_{\mathrm{K}} v_{\mathrm{K}} \\ \rho_{\mathrm{K}} w_{\mathrm{K}} \\ E_{\mathrm{K}} + (s_* - u_{\mathrm{K}})\left(\rho_{\mathrm{K}} s_* + \dfrac{p_{\mathrm{K}}}{s_{\mathrm{K}} - u_{\mathrm{K}}}\right) \\ \alpha_{1_{\mathrm{K}}} \end{pmatrix}. \tag{D.2}$$

The advective numerical flux is fully determined once the wave speeds, s, have been estimated. Following Einfeldt *et al.* [37], we choose

$$\left.\begin{aligned} s_- &= \min(0, s_\mathrm{L}), \\ s_+ &= \max(0, s_\mathrm{R}), \end{aligned}\right\} \tag{D.3}$$

and

$$\left.\begin{aligned} s_\mathrm{L} &= \min(\bar{u} - \bar{c}, u_\mathrm{L} - c_\mathrm{L}), \\ s_\mathrm{R} &= \max(\bar{u} + \bar{c}, u_\mathrm{R} + c_\mathrm{R}), \end{aligned}\right\} \tag{D.4}$$

where $\bar{u}$ and $\bar{c}$ are averages computed from the left and right states of the Riemann problem and may be obtained from either a Roe or an arithmetic averaging procedure. In practice, however, we once again find that the two averaging methods yield nearly identical numerical results and so choose to compute arithmetic averages since they are more computationally efficient. Finally, to estimate the wave speed in the star region, we follow Batten *et al.* [9] in choosing

$$s_* = \frac{p_\mathrm{R} - p_\mathrm{L} + \rho_\mathrm{L} u_\mathrm{L}(s_\mathrm{L} - u_\mathrm{L}) - \rho_\mathrm{R} u_\mathrm{R}(s_\mathrm{R} - u_\mathrm{R})}{\rho_\mathrm{L}(s_\mathrm{L} - u_\mathrm{L}) - \rho_\mathrm{R}(s_\mathrm{R} - u_\mathrm{R})}. \tag{D.5}$$

The above choice of wave speeds will result in the exact resolution of isolated shockwaves and contact waves by the HLLC solver [9].

With the advective numerical flux computed, we may now evaluate the numerical source term velocity and diffusive flux. In both cases, for consistency, the same velocity as that in the advective numerical flux must be utilized [64, 90]. The component of the numerical velocity in the x-direction is given by

$$\hat{u} = \frac{1 + \mathrm{sgn}(s_*)}{2}\left[u_\mathrm{L} + s_-\left(\frac{s_\mathrm{L} - u_\mathrm{L}}{s_\mathrm{L} - s_*} - 1\right)\right] + \frac{1 - \mathrm{sgn}(s_*)}{2}\left[u_\mathrm{R} + s_+\left(\frac{s_\mathrm{R} - u_\mathrm{R}}{s_\mathrm{R} - s_*} - 1\right)\right], \tag{D.6}$$

and is derived from the advective numerical flux of the advection equation. The remaining velocity components, on the other hand, may simply be written as

$$\hat{v} = \frac{1+\mathrm{sgn}(s_*)}{2} v_{\mathrm{L}} + \frac{1-\mathrm{sgn}(s_*)}{2} v_{\mathrm{R}}, \tag{D.7}$$

$$\hat{w} = \frac{1+\mathrm{sgn}(s_*)}{2} w_{\mathrm{L}} + \frac{1-\mathrm{sgn}(s_*)}{2} w_{\mathrm{R}}. \tag{D.8}$$

In the solution procedure of a Riemann problem in the x-direction, only $\hat{u}$ is necessary in order to evaluate the numerical source term velocity, while all of the velocity components are needed to compute the numerical diffusive flux. In addition, the latter also requires that a value of the velocity gradient be available at the interface of the Riemann problem. Following Perigaud and Saurel [90], we choose

$$\overline{\nabla \mathbf{u}} = \frac{1}{2}\left[(\nabla \mathbf{u})_{\mathrm{L}} + (\nabla \mathbf{u})_{\mathrm{R}}\right]. \tag{D.9}$$

Appendix E

Algorithm

To facilitate the implementation of the proposed numerical scheme, we proceed next by illustrating how its building blocks are assembled to evolve the cell average conservative variables in time. We omit, however, discussing the time-marching scheme itself, since it is explicit and straightforward to implement. Instead, we provide the steps necessary to evaluate the RHS of the semi-discrete form of the equations of motion in Equation (3.4), which is represented by the $\mathbf{L}$ operator in the time-stepper in Equation (3.19), and must be evaluated at least once at each time-stage. We begin with the cell average conservative variables, $\mathbf{q}_{i,j,k}$:

1. From $\mathbf{q}_{i,j,k}$, build the primitive variables, $\mathbf{v}_{i,j,k}$:
   (a) Reconstruct $\mathbf{q}_{i,j,k}$ in the x-direction to get $\mathbf{q}_{i_l,j,k}$.
   (b) Reconstruct $\mathbf{q}_{i_l,j,k}$ in the y-direction to get $\mathbf{q}_{i_l,j_m,k}$.
   (c) Reconstruct $\mathbf{q}_{i_l,j_m,k}$ in the z-direction to get $\mathbf{q}_{i_l,j_m,k_n}$.
   (d) Convert $\mathbf{q}_{i_l,j_m,k_n}$ into $\mathbf{v}_{i_l,j_m,k_n}$.
   (e) Average $\mathbf{v}_{i_l,j_m,k_n}$ to get $\mathbf{v}_{i,j,k}$.
2. To evaluate the RHS contribution of the advective fluxes and source term in the x-direction, from $\mathbf{v}_{i,j,k}$, build $\mathbf{f}^{\mathrm{a}}_{i+1/2,j,k}$ and $u_{i+1/2,j,k}$, respectively:
   (a) Project $\mathbf{v}_{i,j,k}$ onto the characteristic fields to get $\mathbf{w}_{i,j,k}$.
   (b) Reconstruct $\mathbf{w}_{i,j,k}$ in the x-direction to get $\mathbf{w}^{\mathrm{K}}_{i+1/2,j,k}$.

   (c) Reconstruct $\mathbf{w}^{\mathrm{K}}_{i+1/2,j,k}$ in the y-direction to get $\mathbf{w}^{\mathrm{K}}_{i+1/2,j_l,k}$.

   (d) Reconstruct $\mathbf{w}^{\mathrm{K}}_{i+1/2,j_l,k}$ in the z-direction to get $\mathbf{w}^{\mathrm{K}}_{i+1/2,j_l,k_m}$.

   (e) Project $\mathbf{w}^{\mathrm{K}}_{i+1/2,j_l,k_m}$ onto the physical fields to get $\mathbf{v}^{\mathrm{K}}_{i+1/2,j_l,k_m}$.

   (f) Convert $\mathbf{v}^{\mathrm{K}}_{i+1/2,j_l,k_m}$ into $\mathbf{q}^{\mathrm{K}}_{i+1/2,j_l,k_m}$.

   (g) Compute $\hat{\mathbf{f}}^{\mathrm{a}}_{i+1/2,j_l,k_m}$ and $\hat{u}_{i+1/2,j_l,k_m}$ from $\mathbf{q}^{\mathrm{K}}_{i+1/2,j_l,k_m}$ with the Riemann solver.

   (h) Average $\hat{\mathbf{f}}^{\mathrm{a}}_{i+1/2,j_l,k_m}$ and $\hat{u}_{i+1/2,j_l,k_m}$ to get $\mathbf{f}^{\mathrm{a}}_{i+1/2,j,k}$ and $u_{i+1/2,j,k}$.

3. To evaluate the RHS contribution of the advective fluxes and source term in the y- and z-directions, build $\mathbf{h}^{\mathrm{a}}_{i,j+1/2,k}$ and $v_{i,j+1/2,k}$, and $\mathbf{g}^{\mathrm{a}}_{i,j,k+1/2}$ and $w_{i,j,k+1/2}$, respectively, by following a procedure similar to that in Step 2.

4. From the velocities $\mathbf{u}^{\mathrm{K}}_{i+1/2,j_l,k_m}$, build the spatial derivative of the velocity in the x-direction, $\partial_x \mathbf{u}_{i,j,k}$:

   (a) Average $\mathbf{u}^{\mathrm{K}}_{i+1/2,j_l,k_m}$ to get $\mathbf{u}_{i+1/2,j_l,k_m}$.

   (b) Average $\mathbf{u}_{i+1/2,j_l,k_m}$ to get $\mathbf{u}_{i+1/2,j,k}$.

   (c) Compute $\partial_x \mathbf{u}_{i,j,k}$ from $\mathbf{u}_{i+1/2,j,k}$ with the divergence theorem.

5. Build $\partial_y \mathbf{u}_{i,j,k}$ and $\partial_z \mathbf{u}_{i,j,k}$ by following a procedure similar to that in Step 4.

6. To evaluate the RHS contribution of diffusive fluxes in the x-direction, from $\hat{\mathbf{u}}_{i+1/2,j_l,k_m}$ and $\nabla \mathbf{u}_{i,j,k}$, build $\mathbf{f}^{\mathrm{d}}_{i+1/2,j,k}$:

   (a) Reconstruct $\nabla \mathbf{u}_{i,j,k}$ to get $\nabla \mathbf{u}^{\mathrm{K}}_{i+1/2,j_l,k_m}$ by following a procedure similar to that in Step 2, (b)–(d).

   (b) Average $\nabla \mathbf{u}^{\mathrm{K}}_{i+1/2,j_l,k_m}$ to get $\nabla \mathbf{u}_{i+1/2,j_l,k_m}$.

   (c) Compute $\hat{\mathbf{f}}^{\mathrm{d}}_{i+1/2,j_l,k_m}$ from $\hat{\mathbf{u}}_{i+1/2,j_l,k_m}$ and $\nabla \mathbf{u}_{i+1/2,j_l,k_m}$ directly.

   (d) Average $\hat{\mathbf{f}}^{\mathrm{d}}_{i+1/2,j_l,k_m}$ to get $\mathbf{f}^{\mathrm{d}}_{i+1/2,j,k}$.

7. To evaluate the RHS contribution of diffusive fluxes in the y- and z-directions, thus completing the evaluation of the RHS, build $\mathbf{g}^{\mathrm{d}}_{i,j+1/2,k}$ and $\mathbf{h}^{\mathrm{d}}_{i,j,k+1/2}$, respectively, by following a procedure similar to that in Step 6.

Appendix F

Performance benchmarks

In order to simulate shock-induced bubble collapse across the parameter space defined in Section 2.3.4, the numerical method of Chapter 3 was implemented in 3D and subsequently extended to parallel, due to the significant computational cost of performing direct, multidimensional, numerical simulations. The simulations were then carried out on Kraken – a large computing system compromised of 9408 nodes, each containing 12 cores or, more precisely, two 2.6 GHz six-core AMD Opteron processors. For each simulation, 288 nodes, or 3456 cores, were utilized. In this section, we document the Kraken grind time and scalability of the multicomponent flow solver for typical algorithm parameters utilized in the inviscid simulations, see Section 4.1 for details.

We measure the parallel scaling performance of the multicomponent flow solver with the strong scaling, weak scaling and speedup tests, the results of which are shown in Figure F.1. The strong scaling test is a measure of how the time to solution, or wall clock time per time step, varies for a fixed problem size, *i.e.* a fixed grid, as a function of the number of cores utilized in the computation. The weak scaling test, on the other hand, benchmarks how well the computational load is balanced across these cores by measuring the time to solution while maintaining a fixed core grid size. Finally, the speedup test measures the factor increase in the time to solution as a function of the total number of cores, with respect to a serial computation. Note from Figure F.1 that the multicomponent flow solver achieves almost ideal behavior in each benchmark, with a near unity slope in the strong scaling and speedup tests, *i.e.* a nearly 100% parallel scaling efficiency, and an approximately constant computational load maintained in the weak scaling test. The results are

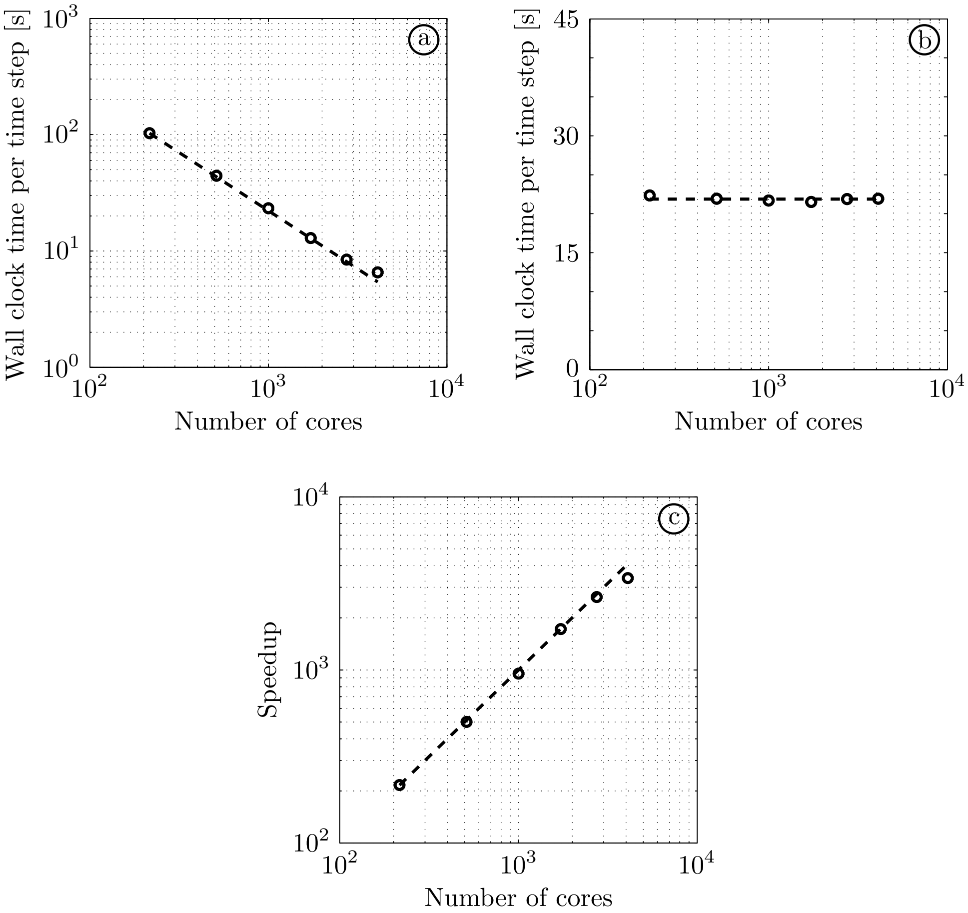

Figure F.1: Parallel performance benchmarks of the numerical implementation of the multicomponent flow algorithm. These include (a) the strong scaling, (b) weak scaling and (c) speedup tests. The ideal performance is given by (−−) and (○) denotes the measured performance. The strong scaling and speedup tests are carried out on a 500^3 grid, while a constant load of 50^3 cells per core is maintained during the weak scaling test.

reported for up to 4096 cores at which point the strong scaling and speedup behaviors begin to deviate from ideal. The latter motivates to use of 3456 cores in simulations, since it strikes a good balance between reducing the time to solution and computational efficiency.

Finally, the parallel scaling performance results are also utilized to compute the average grind time for the multicomponent flow solver, where the grind time is a measure of the wall clock time required to advance one flow variable in a single cell by one time-step. For the inviscid simulations performed in the scaling benchmarks, the average grind time is 20 μs, with nearly 80% of that time spent in the WENO reconstruction procedure and the remainder largely in the HLLC approximate Riemann solver. Therefrom, we can also approximate the grind time for viscous simulations, which require twice the number of WENO reconstructions for the velocity components in order to recover their first-order spatial derivatives, but no additional time expenditure in the HLLC solver. Then, conservatively, since the velocity components represent less than 50% of the total flow variables in simulations with two or more fluids, the grind time can be expected to be at most 28 μs in the viscous case.

Appendix G

Post-processing of finite strain fluid deformations

The strain field in each element of the finite element mesh is approximated from its nodal displacements, by utilizing a standard isoparametric mapping between the natural or virtual coordinates of an element, see Figure G.1(a), and its physical coordinates, see Figure G.1(b) [75]. For a hexahedral element, the isoparametric mapping consists of trilinear shape functions, N_i – one associated with each node of the element, $i = 1, 2, ..., 8$ – which are given here as a function of the natural coordinates, along with the position vectors of the corresponding nodes, $\boldsymbol{\xi}_i$:

$$\left.\begin{aligned}
\boldsymbol{\xi}_1 &= (-1,-1,-1)^{\mathrm{T}}, & N_1(\boldsymbol{\xi}) &= \frac{1}{8}(1-\xi_1)(1-\xi_2)(1-\xi_3),\\
\boldsymbol{\xi}_2 &= (+1,-1,-1)^{\mathrm{T}}, & N_2(\boldsymbol{\xi}) &= \frac{1}{8}(1+\xi_1)(1-\xi_2)(1-\xi_3),\\
\boldsymbol{\xi}_3 &= (+1,+1,-1)^{\mathrm{T}}, & N_3(\boldsymbol{\xi}) &= \frac{1}{8}(1+\xi_1)(1+\xi_2)(1-\xi_3),\\
\boldsymbol{\xi}_4 &= (-1,+1,-1)^{\mathrm{T}}, & N_4(\boldsymbol{\xi}) &= \frac{1}{8}(1-\xi_1)(1+\xi_2)(1-\xi_3),\\
\boldsymbol{\xi}_5 &= (-1,-1,+1)^{\mathrm{T}}, & N_5(\boldsymbol{\xi}) &= \frac{1}{8}(1-\xi_1)(1-\xi_2)(1+\xi_3),\\
\boldsymbol{\xi}_6 &= (+1,-1,+1)^{\mathrm{T}}, & N_6(\boldsymbol{\xi}) &= \frac{1}{8}(1+\xi_1)(1-\xi_2)(1+\xi_3),\\
\boldsymbol{\xi}_7 &= (+1,+1,+1)^{\mathrm{T}}, & N_7(\boldsymbol{\xi}) &= \frac{1}{8}(1+\xi_1)(1+\xi_2)(1+\xi_3),\\
\boldsymbol{\xi}_8 &= (-1,+1,+1)^{\mathrm{T}}, & N_8(\boldsymbol{\xi}) &= \frac{1}{8}(1-\xi_1)(1+\xi_2)(1+\xi_3),
\end{aligned}\right\} \tag{G.1}$$

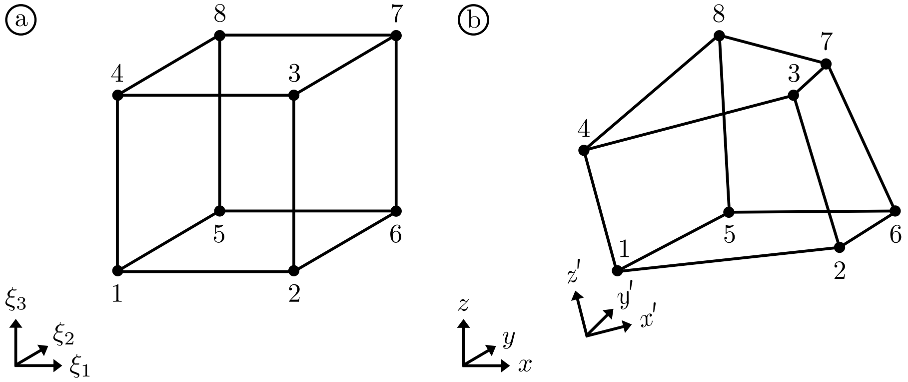

Figure G.1: Hexahedral finite element in (a) its natural or virtual coordinates and (b) its physical (Eulerian and Lagrangian) coordinates.

where

$$N_i(\boldsymbol{\xi}_j) = \delta_{ij}, \quad \sum_{i=1}^{8} N_i(\boldsymbol{\xi}) = 1. \tag{G.2}$$

The isoparametric mapping between the natural and physical coordinates of the element is then simply given by

$$\left.\begin{aligned} \mathbf{x}(\boldsymbol{\xi}, t) &= \sum_{i=1}^{8} N_i(\boldsymbol{\xi})\mathbf{x}_i(t), \\ \mathbf{x}'(\boldsymbol{\xi}, t) &= \sum_{i=1}^{8} N_i(\boldsymbol{\xi})\mathbf{x}'_i(t), \end{aligned}\right\} \tag{G.3}$$

from which an analogous expression for the displacements, $\mathbf{d}(\boldsymbol{\xi}, t) = \mathbf{x}'(\boldsymbol{\xi}, t) - \mathbf{x}(\boldsymbol{\xi}, 0)$, may be written:

$$\mathbf{d}(\boldsymbol{\xi}, t) = \sum_{i=1}^{8} N_i(\boldsymbol{\xi})\mathbf{d}_i(t). \tag{G.4}$$

The deformation gradient tensor, $\mathbf{F}$, is computed therefrom by taking the partial spatial derivative of the expressions in Equations (G.3) and (G.4) with respect to the natural coordinates:

$$\left.\begin{aligned}
\frac{\partial \mathbf{x}}{\partial \boldsymbol{\xi}} &= \sum_{i=1}^{8} \mathbf{x}_i \frac{\partial N_i}{\partial \boldsymbol{\xi}}, \\
\frac{\partial \mathbf{x}'}{\partial \boldsymbol{\xi}} &= \sum_{i=1}^{8} \mathbf{x}'_i \frac{\partial N_i}{\partial \boldsymbol{\xi}}, \\
\frac{\partial \mathbf{d}}{\partial \boldsymbol{\xi}} &= \sum_{i=1}^{8} \mathbf{d}_i \frac{\partial N_i}{\partial \boldsymbol{\xi}},
\end{aligned}\right\} \tag{G.5}$$

and substituting them in the expression for **F**, Equation (5.6):

$$\mathbf{F} = \frac{\partial \mathbf{x}'}{\partial \mathbf{x}} = \frac{\partial \boldsymbol{\xi}}{\partial \mathbf{x}} \frac{\partial \mathbf{x}'}{\partial \boldsymbol{\xi}} = \frac{\partial \boldsymbol{\xi}}{\partial \mathbf{x}} \frac{\partial \mathbf{d}}{\partial \boldsymbol{\xi}} + \mathbf{I}, \tag{G.6}$$

to get

$$\mathbf{F} = \left(\sum_{i=1}^{8} \mathbf{x}_i \frac{\partial N_i}{\partial \boldsymbol{\xi}} \right)^{-1} \sum_{i=1}^{8} \mathbf{d}_i \frac{\partial N_i}{\partial \boldsymbol{\xi}} + \mathbf{I}, \tag{G.7}$$

where the function notation has been omitted for the sake of conciseness. Equation (G.7) can subsequently be utilized in Equation (5.1) to compute the Green-Lagrange strain anywhere in the element.

Bibliography

[1] R. Abgrall. How to prevent pressure oscillations in multicomponent flow calculations: A quasi conservative approach. *J. Comput. Phys.*, 125(1):150–160, 1996.

[2] R. Abgrall and S. Karni. Computations of compressible multifluids. *J. Comput. Phys.*, 169 (2):594–623, 2001.

[3] G. Allaire, S. Clerc, and S. Kokh. A five-equation model for the simulation of interfaces between compressible fluids. *J. Comput. Phys.*, 181(2):577–616, 2002.

[4] M. Arora and P. L. Roe. On postshock oscillations due to shock capturing schemes in unsteady flows. *J. Comput. Phys.*, 130(1):25–40, 1997.

[5] M. R. Bailey, L. A. Crum, A. P. Evan, J. A. McAteer, J. C. Williams, O. A. Sapozhnikov, R. O. Cleveland, and T. Colonius. Cavitation in shock wave lithotripsy. In *Fifth International Symposium on Cavitation*, Osaka, Japan, 2003.

[6] M. R. Bailey, Y. A. Pishchalnikov, O. A. Sapozhnikov, R. O. Cleveland, J. A. McAteer, N. A. Miller, I. V. Pishchalnikova, B. A. Connors, L. A. Crum, and A. P. Evan. Cavitation detection during shock-wave lithotripsy. *Ultrasound Med. Biol.*, 31(9):1245–1256, 2005.

[7] G. J. Ball, B. P. Howell, T. G. Leighton, and M. J. Schofield. Shock-induced collapse of a cylindrical air cavity in water: A free-Lagrange simulation. *Shock Waves*, 10(4):265–276, 2000.

[8] D. S. Balsara and C. W. Shu. Monotonicity preserving weighted essentially non-oscillatory schemes with increasingly high order of accuracy. *J. Comput. Phys.*, 160(2):405–452, 2000.

[9] P. Batten, N. Clarke, C. Lambert, and D. M. Causon. On the choice of wavespeeds for the HLLC Riemann solver. *SIAM J. Sci. Comput.*, 18(6):1553–1570, 1997.

[10] J. E. Blatteau, J. B. Souraud, E. Gempp, and A. Boussuges. Gas nuclei, their origin, and their role in bubble formation. *Aviat. Space Envir. Md.*, 77(10):1068–1076, 2006.

[11] M. E. Brachet, D. I. Meiron, S. A. Orszag, B. G. Nickel, R. H. Morf, and U. Frisch. Small-scale structure of the Taylor-Green vortex. *J. Fluid Mech.*, 130:411–452, 1983.

[12] E. A. Brujan. *Cavitation in non-Newtonian fluids: With biomedical and bioengineering applications.* Springer Verlag, Heidelberg; New York, 2011.

[13] E. A. Brujan, K. Nahen, P. Schmidt, and A. Vogel. Dynamics of laser-induced cavitation bubbles near an elastic boundary. *J. Fluid Mech.*, 433:251–281, 2001.

[14] E. A. Brujan, K. Nahen, P. Schmidt, and A. Vogel. Dynamics of laser-induced cavitation bubbles near elastic boundaries: Influence of the elastic modulus. *J. Fluid Mech.*, 433:283–314, 2001.

[15] A. C. Burton. Relation of structure to function of the tissues of the wall of blood vessels. *Physiol. Rev.*, 34(4):619–642, 1954.

[16] J. R. Cash and A. H. Karp. A variable order Runge-Kutta method for initial-value problems with rapidly varying right-hand sides. *ACM T. Math. Software*, 16(3):201–222, 1990.

[17] C. F. Caskey, S. M. Stieger, S. Qin, P. A. Dayton, and K. W. Ferrara. Direct observations of ultrasound microbubble contrast agent interaction with the microvessel wall. *J. Acoust. Soc. Am.*, 122(2):1191–1200, 2007.

[18] S. D. Chambers, R. H. Bartlett, and S. L. Ceccio. Determination of the *in vivo* cavitation nuclei characteristics of blood. *ASAIO J.*, 45(6):541–549, 1999.

[19] H. Chen, A. A. Brayman, M. R. Bailey, and T. J. Matula. Blood vessel rupture by cavitation. *Urol. Res.*, 38(4):321–326, 2010.

[20] H. Chen, W. Kreider, A. A. Brayman, M. R. Bailey, and T. J. Matula. Blood vessel deformations on microsecond time scales by ultrasonic cavitation. *Phys. Rev. Lett.*, 106(3), 2011.

[21] H. Chen, C. Perez, A. A. Brayman, and T. J. Matula. High speed imaging of shockwave-induced dynamics of cavitation bubbles and vessel wall. *J. Acoust. Soc. Am.*, 129:2374, 2011.

[22] H. Chen, A. A. Brayman, A. P. Evan, and T. J. Matula. Preliminary observations on the spatial correlation between short-burst microbubble oscillations and vascular bioeffects. *Ultrasound Med. Biol.*, 38(12):2151–2162, 2012.

[23] H. Chen, A. A. Brayman, and T. J. Matula. Characteristic microvessel relaxation timescales associated with ultrasound-activated microbubbles. *Appl. Phys. Lett.*, 101(16), 2012.

[24] C. C. Church. A theoretical study of cavitation generated by an extracorporeal shock-wave lithotripter. *J. Acoust. Soc. Am.*, 86(1):215–227, 1989.

[25] C. C. Church and X. M. Yang. Theoretical study of gas bubble dynamics in tissue. *AIP Conf. Proc.*, 838:217–224, 2006.

[26] R. O. Cleveland and J. A. McAteer. The physics of shock wave lithotripsy. In A. D. Smith, G. Preminger, G. Badlani, and L. Kavoussi, editors, *Smith's Textbook on Endourology*, chapter 49, pages 529–558. Wiley-Blackwell, 3rd edition, 2012.

[27] R. O. Cleveland, D. A. Lifshitz, B. A. Connors, A. P. Evan, L. R. Willis, and L. A. Crum. *In vivo* pressure measurements of lithotripsy shock waves in pigs. *Ultrasound Med. Biol.*, 24(2): 293–306, 1998.

[28] R. O. Cleveland, M. R. Bailey, N. Fineberg, B. Hartenbaum, M. Lokhandwalla, J. A. McAteer, and B. Sturtevant. Design and characterization of a research electrohydraulic lithotripter patterned after the Dornier HM3. *Rev. Sci. Instrum.*, 71(6):2514–2525, 2000.

[29] J. P. Cocchi and R. Saurel. A Riemann problem based method for the resolution of compressible multimaterial flows. *J. Comput. Phys.*, 137(2):265–298, 1997.

[30] J. P. Cocchi, R. Saurel, and J. C. Loraud. Treatment of interface problems with Godunov-type schemes. *Shock Waves*, 5(6):347–357, 1996.

[31] A. J. Coleman, J. E. Saunders, L. A. Crum, and M. Dyson. Acoustic cavitation generated by an extracorporeal shockwave lithotripter. *Ultrasound Med. Biol.*, 13(2):69–76, 1987.

[32] A. J. Coleman, M. J. Choi, J. E. Saunders, and T. G. Leighton. Acoustic emission and sonoluminescence due to cavitation at the beam focus of an electrohydraulic shock wave lithotripter. *Ultrasound Med. Biol.*, 18(3):267–281, 1992.

[33] V. Coralic and T. Colonius. Shock-induced collapse of a bubble inside a deformable vessel. *Eur. J. Mech. B-Fluid*, 40:64–74, 2013.

[34] L. A. Crum. Cavitation microjets as a contributory mechanism for renal calculi disintegration in ESWL. *J. Urology*, 140(6):1587–1590, 1988.

[35] M. Delius, G. Enders, Z. R. Xuan, H. G. Liebich, and W. Brendel. Biological effects of shock waves: Kidney damage by shock waves in dogs – Dose dependence. *Ultrasound Med. Biol.*, 14 (2):117–122, 1988.

[36] F. A. Duck. *Physical properties of tissue: A comprehensive reference book.* Academic Press, London; San Diego, 1990.

[37] B. Einfeldt, C. D. Munz, P. L. Roe, and B. Sjgreen. On Godunov-type methods near low densities. *J. Comput. Phys.*, 92(2):273–295, 1991.

[38] M. Farshad, M. Barbezat, P. Flueler, F. Schmidlin, P. Graber, and P. Niederer. Material characterization of the pig kidney in relation with the biomechanical analysis of renal trauma. *J. Biomech.*, 32(4):417–425, 1999.

[39] R. P. Fedkiw, T. Aslam, B. Merriman, and S. Osher. A non-oscillatory Eulerian approach to interfaces in multimaterial flows (the ghost fluid method). *J. Comput. Phys.*, 152(2):457–492, 1999.

[40] H. H. Francis and A. A. Anthony. Fluid dynamics. Technical Report LA-4700, Los Alamos National Laboratory, 1971.

[41] J. B. Freund. Suppression of shocked-bubble expansion due to tissue confinement with application to shock-wave lithotripsy. *J. Acoust. Soc. Am.*, 123(5):2867–2874, 2008.

[42] J. B. Freund, T. Colonius, and A. P. Evan. A cumulative shear mechanism for tissue damage initiation in shock-wave lithotripsy. *Ultrasound Med. Biol.*, 33(9):1495–1503, 2007.

[43] J. B. Freund, R. K. Shukla, and A. P. Evan. Shock-induced bubble jetting into a viscous fluid with application to tissue injury in shock-wave lithotripsy. *J. Acoust. Soc. Am.*, 126(5): 2746–56, 2009.

[44] D. Fuster and S. Zaleski. The importance of liquid evaporation on rectified diffusion processes. In *7th International Conference on Multiphase Flow*, Tampa, FL, 2010.

[45] C. Geuzaine and J. F. Remacle. Gmsh: A 3-D finite element mesh generator with built-in pre- and post-processing facilities. *Int. J. Numer. Meth. Eng.*, 79(11):1309–1331, 2009.

[46] J. Glimm, J. W. Grove, X. L. Li, K. M. Shyue, Y. Zeng, and Q. Zhang. Three-dimensional front tracking. *SIAM J. Sci. Comput.*, 19(3):703–727, 1998.

[47] J. Glimm, X. L. Li, Y. J. Liu, Z. L. Xu, and N. Zhao. Conservative front tracking with improved accuracy. *SIAM J. Numer. Anal.*, 41(5):1926–1947, 2003.

[48] D. M. Glover, W. J. Jenkins, and S. C. Doney. *Modeling methods for marine science.* Cambridge University Press, Cambridge; New York, 2011.

[49] A. B. Gojani, K. Ohtani, K. Takayama, and S. H. R. Hosseini. Shock Hugoniot and equations of states of water, castor oil, and aqueous solutions of sodium chloride, sucrose and gelatin. *Shock Waves*, 2009.

[50] S. A. Goss, R. L. Johnston, and F. Dunn. Compilation of empirical ultrasonic properties of mammalian tissues. II. *J. Acoust. Soc. Am.*, 68(1):93–108, 1980.

[51] S. Gottlieb and C. W. Shu. Total variation diminishing Runge-Kutta schemes. *Math. Comput.*, 67(221):73–85, 1998.

[52] J. F. Haas and B. Sturtevant. Interaction of weak shock waves with cylindrical and spherical gas inhomogeneities. *J. Fluid Mech.*, 181:41–76, 1987.

[53] R. K. S. Hankin. The Euler equations for multiphase compressible flow in conservation form – Simulation of shock-bubble interactions. *J. Comput. Phys.*, 172(2):808–826, 2001.

[54] A. Harten, B. Engquist, S. Osher, and S. R. Chakravarthy. Uniformly high order accurate essentially non-oscillatory schemes, III. *J. Comput. Phys.*, 71(2):231–303, 1987.

[55] B. Hejazialhosseini, D. Rossinelli, M. Bergdorf, and P. Koumoutsakos. High order finite volume methods on wavelet-adapted grids with local time-stepping on multicore architectures for the simulation of shock-bubble interactions. *J. Comput. Phys.*, 229(22):8364–8383, 2010.

[56] A. K. Henrick, T. D. Aslam, and J. M. Powers. Mapped weighted essentially non-oscillatory schemes: Achieving optimal order near critical points. *J. Comput. Phys.*, 207(2):542–567, 2005.

[57] N. Hosseinkhah, H. Chen, T. J. Matula, P. N. Burns, and K. Hynynen. Mechanisms of microbubble-vessel interactions and induced stresses: A numerical study. *J. Acoust. Soc. Am.*, 134(3):1875–1885, 2013.

[58] E. Hrncir and J. Rosina. Surface tension of blood. *Physiol. Res.*, 46(4):319–321, 1997.

[59] X. Y. Hu and B. C. Khoo. An interface interaction method for compressible multifluids. *J. Comput. Phys.*, 198(1):35–64, 2004.

[60] X. Y. Hu, B. C. Khoo, N. A. Adams, and F. L. Huang. A conservative interface method for compressible flows. *J. Comput. Phys.*, 219(2):553–578, 2006.

[61] P. Jenny, B. Muller, and H. Thomann. Correction of conservative Euler solvers for gas mixtures. *J. Comput. Phys.*, 132(1):91–107, 1997.

[62] G. S. Jiang and C. W. Shu. Efficient implementation of weighted ENO schemes. *J. Comput. Phys.*, 126(1):202–228, 1996.

[63] E. Johnsen. *Numerical simulations of non-spherical bubble collapse with applications to shockwave lithotripsy.* PhD thesis, California Institute of Technology, 2008.

[64] E. Johnsen and T. Colonius. Implementation of WENO schemes in compressible multicomponent flow problems. *J. Comput. Phys.*, 219(2):715–732, 2006.

[65] E. Johnsen and T. Colonius. Shock-induced collapse of a gas bubble in shockwave lithotripsy. *J. Acoust. Soc. Am.*, 124(4):2011–2020, 2008.

[66] E. Johnsen and T. Colonius. Numerical simulations of non-spherical bubble collapse. *J. Fluid Mech.*, 629:231–262, 2009.

[67] E. Johnsen and F. Ham. Preventing numerical errors generated by interface-capturing schemes in compressible multi-material flows. *J. Comput. Phys.*, 231(17):5705–5717, 2012.

[68] S. Karni. Multicomponent flow calculations by a consistent primitive algorithm. *J. Comput. Phys.*, 112(1):31–43, 1994.

[69] S. Karni. Hybrid multifluid algorithms. *SIAM J. Sci. Comput.*, 17(5):1019–1039, 1996.

[70] C. A. Kennedy and M. H. Carpenter. Additive Runge-Kutta schemes for convection-diffusion-reaction equations. *Appl. Numer. Math.*, 44(1-2):139–181, 2003.

[71] E. Klaseboer, S. W. Fong, C. K. Turangan, B. C. Khoo, A. J. Szeri, M. L. Calvisi, G. N. Sankin, and P. Zhong. Interaction of lithotripter shockwaves with single inertial cavitation bubbles. *J. Fluid Mech.*, 593:33–56, 2007.

[72] K. Kobayashi, T. Kodama, and H. Takahira. Shock wave-bubble interaction near soft and rigid boundaries during lithotripsy: Numerical analysis by the improved ghost fluid method. *Phys. Med. Biol.*, 56(19):6421–6440, 2011.

[73] T. Kodama and Y. Tomita. Cavitation bubble behavior and bubble-shock wave interaction near a gelatin surface as a study of *in vivo* bubble dynamics. *Appl. Phys. B-Lasers O.*, 70(1): 139–149, 2000.

[74] B. M. Koeppen and B. A. Stanton. *Berne and Levy physiology.* Mosby/Elsevier, Philadelphia, PA, 6th edition, 2010.

[75] O. Kolditz. *Computational methods in environmental fluid mechanics.* Springer, Berlin; New York, 2002.

[76] R. J. LeVeque. *Finite volume methods for hyperbolic problems.* Cambridge Texts in Applied Mathematics. Cambridge University Press, Cambridge; New York, 2002.

[77] T. G. Liu, B. C. Khoo, and K. S. Yeo. Ghost fluid method for strong shock impacting on material interface. *J. Comput. Phys.*, 190(2):651–681, 2003.

[78] T. G. Liu, B. C. Khoo, and C. W. Wang. The ghost fluid method for compressible gas-water simulation. *J. Comput. Phys.*, 204(1):193–221, 2005.

[79] W. Liu, L. Yuan, and C. W. Shu. A conservative modification to the ghost fluid method for compressible multiphase flows. *Commun. Comput. Phys.*, 10(4):785–806, 2011.

[80] X. D. Liu, S. Osher, and T. Chan. Weighted essentially non-oscillatory schemes. *J. Comput. Phys.*, 115(1):200–212, 1994.

[81] H. Luo, J. D. Baum, and R. Lohner. On the computation of multi-material flows using ALE formulation. *J. Comput. Phys.*, 194(1):304–328, 2004.

[82] A. Marquina and P. Mulet. A flux-split algorithm applied to conservative models for multicomponent compressible flows. *J. Comput. Phys.*, 185(1):120–138, 2003.

[83] J. Massoni, R. Saurel, B. Nkonga, and R. Abgrall. Some models and Eulerian methods for interface problems between compressible fluids with heat transfer. *Int. J. Heat Mass Tran.*, 45(6):1287–1307, 2002.

[84] H. Miao, S. M. Gracewski, and D. Dalecki. Ultrasonic excitation of a bubble inside a deformable tube: Implications for ultrasonically induced hemorrhage. *J. Acoust. Soc. Am.*, 124(4):2374–2384, 2008.

[85] R. v. Mises. Mechanik der festen Körper im plastisch-deformablen Zustand. *Nachr. Ges. Wiss. Gttingen, Math.-Phys. Kl.*, 1913:582–592, 1913.

[86] W. Mulder, S. Osher, and James A. Sethian. Computing interface motion in compressible gas dynamics. *J. Comput. Phys.*, 100(2):209–228, 1992.

[87] S. Nasseri, L. E. Bilston, and N. Phan-Thien. Viscoelastic properties of pig kidney in shear, experimental results and modelling. *Rheol. Acta*, 41(1-2):180–192, 2002.

[88] R. R. Nourgaliev and T. G. Theofanous. High-fidelity interface tracking in compressible flows: Unlimited anchored adaptive level set. *J. Comput. Phys.*, 224(2):836–866, 2007.

[89] C. D. Ohl and R. Ikink. Shock-wave-induced jetting of micron-size bubbles. *Phys. Rev. Lett.*, 90(21), 2003.

[90] G. Perigaud and R. Saurel. A compressible flow model with capillary effects. *J. Comput. Phys.*, 209(1):139–178, 2005.

[91] Y. A. Pishchalnikov, O. A. Sapozhnikov, M. R. Bailey, J. C. Williams, R. O. Cleveland, T. Colonius, L. A. Crum, A. P. Evan, and J. A. McAteer. Cavitation bubble cluster activity in the breakage of kidney stones by lithotripter shockwaves. *J. Endourol.*, 17(7):435–446, 2003.

[92] J. X. Qiu and C. W. Shu. On the construction, comparison, and local characteristic decomposition for high-order central WENO schemes. *J. Comput. Phys.*, 183(1):187–209, 2002.

[93] J. J. Quirk and S. Karni. On the dynamics of a shock-bubble interaction. *J. Fluid. Mech.*, 318:129–163, 1996.

[94] G. N. Sankin, W. N. Simmons, S. L. Zhu, and P. Zhong. Shock wave interaction with laser-generated single bubbles. *Phys. Rev. Lett.*, 95(3), 2005.

[95] A. C. Santago. *Characterizing the biomechanical response of the liver.* PhD thesis, Virginia Polytechnic Institute and State University, 2010.

[96] R. Saurel and R. Abgrall. A multiphase Godunov method for compressible multifluid and multiphase flows. *J. Comput. Phys.*, 150(2):425–467, 1999.

[97] R. Saurel and R. Abgrall. A simple method for compressible multifluid flows. *SIAM J. Sci. Comput.*, 21(3):1115–1145, 1999.

[98] C. Senatore, M. Wulfmeier, I. Vlahinic, J. Andrade, and K. Iagnemma. Design and implementation of a particle image velocimetry method for analysis of running gear-soil interaction. *J. Terramechanics*, 50(5-6):311–326, 2013.

[99] C. W. Shu. *Essentially non-oscillatory and weighted essentially non-oscillatory schemes for hyperbolic conservation laws*, volume 1697 of *Lecture notes in mathematics*, chapter 4, pages 325–432. Springer Berlin Heidelberg, 1998.

[100] R. K. Shukla, C. Pantano, and J. B. Freund. An interface capturing method for the simulation of multi-phase compressible flows. *J. Comput. Phys.*, 229(19):7411–7439, 2010.

[101] K. M. Shyue. An efficient shock-capturing algorithm for compressible multicomponent problems. *J. Comput. Phys.*, 142(1):208–242, 1998.

[102] K. M. Shyue. A fluid-mixture type algorithm for compressible multicomponent flow with van der Waals equation of state. *J. Comput. Phys.*, 156(1):43–88, 1999.

[103] K. M. Shyue. A fluid-mixture type algorithm for compressible multicomponent flow with Mie-Grüneisen equation of state. *J. Comput. Phys.*, 171(2):678–707, 2001.

[104] L. H. Smaje, P. A. Fraser, and G. Clough. The distensibility of single capillaries and venules in the cat mesentery. *Microvasc. Res.*, 20(3):358–370, 1980.

[105] J. G. Snedeker, P. Niederer, F. R. Schmidlin, M. Farshad, C. K. Demetropoulos, J. B. Lee, and K. H. Yang. Strain-rate dependent material properties of the porcine and human kidney capsule. *J. Biomech.*, 38(5):1011–1021, 2005.

[106] K. K. So, X. Y. Hu, and N. A. Adams. Anti-diffusion interface sharpening technique for two-phase compressible flow simulations. *J. Comput. Phys.*, 231(11):4304–4323, 2012.

[107] H. Terashima and G. Tryggvason. A front-tracking/ghost-fluid method for fluid interfaces in compressible flows. *J. Comput. Phys.*, 228(11):4012–4037, 2009.

[108] K. W. Thompson. Time dependent boundary conditions for hyperbolic systems. *J. Comput. Phys.*, 68(1):1–24, 1987.

[109] K. W. Thompson. Time-dependent boundary conditions for hyperbolic systems, II. *J. Comput. Phys.*, 89(2):439–461, 1990.

[110] V. A. Titarev and E. F. Toro. Finite-volume WENO schemes for three-dimensional conservation laws. *J. Comput. Phys.*, 201(1):238–260, 2004.

[111] E. F. Toro. *Riemann solvers and numerical methods for fluid dynamics: A practical introduction.* Springer, Dordrecht; New York, 3rd edition, 2009.

[112] C. K. Turangan, A. R. Jamaluddin, G. J. Ball, and T. G. Leighton. Free-Lagrange simulations of the expansion and jetting collapse of air bubbles in water. *J. Fluid Mech.*, 598:1–25, 2008.

[113] G. M. Ward and D. I. Pullin. A hybrid, center-difference, limiter method for simulations of compressible multicomponent flows with Mie-Grüneisen equation of state. *J. Comput. Phys.*, 229(8):2999–3018, 2010.

[114] C. Weber, M. E. Moran, E. J. Braun, and G. W. Drach. Injury of rat renal vessels following extracorporeal shock wave treatment. *J. Urology*, 147(2):476–481, 1992.

[115] L. W. Welling, M. T. Zupka, and D. J. Welling. Mechanical properties of basement membrane. *News Physiol. Sci.*, 10:30–35, 1995.

[116] X. M. Yang and C. C. Church. A simple viscoelastic model for soft tissues in the frequency range 6-20 MHz. *IEEE T. Ultrason. Ferr.*, 53(8):1404–1411, 2006.

[117] T. Ye and J. L. Bull. Microbubble expansion in a flexible tube. *J. Biomech. Eng.-T. ASME*, 128(4):554–563, 2006.

[118] P. Zhong, Y. F. Zhou, and S. L. Zhu. Dynamics of bubble oscillation in constrained media and mechanisms of vessel rupture in SWL. *Ultrasound Med. Biol.*, 27(1):119–134, 2001.